2014

DESIGN AND APPLICATION OF WIRELESS PASSIVE MAGNETOELASTIC RESONANCE AND MAGNETOHARMONIC FORCE SENSORS

Brandon D. Pereles
Michigan Technological University

DESIGN AND APPLICATION OF WIRELESS PASSIVE MAGNETOELASTIC RESONANCE AND MAGNETOHARMONIC FORCE SENSORS

By
Brandon D. Pereles

A DISSERTATION
Submitted in partial fulfillment of the requirements for the degree of
DOCTOR OF PHILOSOPHY
In Biomedical Engineering

MICHIGAN TECHNOLOGICAL UNIVERSITY
2014

This dissertation has been approved in partial fulfillment of the requirements for the Degree of DOCTOR OF PHILOSOPHY in Biomedical Engineering.

Department of Biomedical Engineering

Dissertation Advisor: *Keat Ghee Ong*

Committee Member: *Rupak Rajachar*

Committee Member: *Megan Frost*

Committee Member: *Yongmei Jin*

Department Chair: *Sean Kirkpatrick*

This work is dedicated to my mom and dad who always believed in me.
To my brother who has never stopped being proud of me and whose journey in life has been an inspiration.
To all of those teachers who nurtured in me a love for learning and science.
And to my Lord and Savior Jesus Christ who created the Heavens and the Earth and gave man the desire to explore and understand this creation. In His graciousness we were all instilled with the intuition and creativity to make dreams into reality and because of His loving sacrifice I will continue to dream long after my time in this world is over.

Table of Contents

Preface

All of the work in the following chapters was conducted in the Biomedical Sensors Laboratory at the Michigan Technological University campus. Unless otherwise noted below, the copyright for material in this document has been retained by the author(s).

- Chapter 1 contains potions of previously published materials also included in their entirety in Chapters 3, 5 and 6. The full citations for these works are listed below.
- Chapter 2 contains portions of previously published materials also included in their entirety in Chapters 5 and 6 as well as material from Chapter 4 which is currently submitted for publication. The full citations for these works are listed below.
- Chapter 3 has been reprinted in its entirety from B.D. Pereles, T.A. Dienhart, T.M. Sansom, K. Johnston and K.G. Ong (2012). "A wireless, passive load cell based on magnetoelastic resonance." Smart Materials and Structures **21**(7): 075018. B.D Pereles wrote the journal article and performed the listed experiments along with T.A. Dienhart, T.M. Sansom and K. Johnston. K.G. Ong provided technical support throughout the project, in addition to assisting in editing the published article.
- Chapter 4 has been submitted for publication and is printed in its entirety. B.D. Pereles performed the listed experiments and wrote the submitted manuscript. DeRouin participated in the fabrication of key testing equipment and K.G. provided technical support throughout the project, in addition to assisting in editing the submitted article. J. Jiang assisted in the development of the presented ANSYS model.
- Chapter 5 is reprinted in its entirety from B.D Pereles, A.J. DeRouin, T.A. Dienhart, E.L. Tan, K.G. Ong (2012), “A Wireless, Magnetoelastic-based Sensor Array for Force Monitoring on a Hard Surface”, *Sensor Lett.*, 10(3): 805-812. B.D. Pereles performed the listed experiments, with the assistance of T.A. Dienhart, and wrote the article with revisions and assistance from K.G. Ong. A.J. DeRouin participated in the fabrication of key testing equipment. E.L. Tan provided technical assistance in setting up and running the listed experiments.

- Chapter 6 is reprinted in its entirety from Pereles, B.D., DeRouin, A.J., and Ghee Ong, K., *A Wireless, Passive Magnetoelastic Force–Mapping System for Biomedical Applications.* Journal of Biomechanical Engineering, 2013. **136**(1): p. 011010-011010. Published originally by ASME. B.D. Pereles performed the listed experiments and wrote the article with assistance from Professor K.G. Ong. A.J. DeRouin participated in the fabrication of key testing equipment.

Acknowledgments

The author would like to acknowledge funding for portions of the presented work from athe Department of Defense (DOD) of the Office of the Congressionally Directed Medical Research Programs (CDMRP), Grant DR081026 Hypothesis Development.

The authors would like to acknowledge additional funding from the National Institute of Biomedical Imaging and Bioengineering under Grant R15EB008883-01A1.

This research was also conducted with Government support under contract FA9550-11-C-0028 and awarded by DOD, Air Force Office of Scientific Research, National Defense Science and Engineering Graduate (NDSEG) Fellowship, 32 CFR 168a.

The authors would like to acknowledge Northern Orthotics & Prosthetics Inc. for contributions to this work.

Support in the design and fabrication of the automated pneumatic mechanical loader system, crucial to the completion of the presented work, was graciously provided by Master Machinist Martin R. Toth.

Special thanks to fellow graduate student Andrew DeRouin whose help and support not only in research but as a close friend has been invaluable.

Thanks to everyone at Evangel Baptist Church for their constant prayers and support over the last five years.

This work would not have been possible without the friendship and mentoring of Aaron Green, Jon Stone, Jay Weidner, Nate Marsh, Kedmon Hungwe and many others who have guided me through the ups and downs of life. Thank you all.

Lastly, I cannot thank my advisor, Professor Keat Ghee Ong, enough for all of the time and effort he has invested in training me. None of this work would be possible without his guidance and expertise.

Abstract

DESIGN AND APPLICATION OF WIRELESS PASSIVE MAGNETOELASTIC RESONANCE AND MAGNETOHARMONIC FORCE SENSORS

The objective of the work described in this dissertation is the development of new wireless passive force monitoring platforms for applications in the medical field, specifically monitoring lower limb prosthetics. The developed sensors consist of stress sensitive, magnetically soft amorphous metallic glass materials. The first technology is based on magnetoelastic resonance. Specifically, when exposed to an AC excitation field along with a constant DC bias field, the magnetoelastic material mechanically vibrates, and may reaches resonance if the field frequency matches the mechanical resonant frequency of the material. The presented work illustrates that an applied loading pins portions of the strip, effectively decreasing the strip length, which results in an increase in the frequency of the resonance. The developed technology is deployed in a prototype lower limb prosthetic sleeve for monitoring forces experienced by the distal end of the residuum. This work also reports on the development of a magnetoharmonic force sensor comprised of the same material. According to the Villari effect, an applied loading to the material results in a change in the permeability of the magnetic sensor which is visualized as an increase in the higher-order harmonic fields of the material. Specifically, by applying a constant low frequency AC field and sweeping the applied DC biasing field, the higher-order harmonic components of the magnetic response can be visualized. This sensor technology was also instrumented onto a lower limb prosthetic for proof of deployment; however, the magnetoharmonic sensor illustrated complications with sensor positioning and a necessity to tailor the interface mechanics between the sensing material and the surface being monitored. The novelty of these two technologies is in their wireless passive nature which allows for long term monitoring over the life time of a given device. Additionally, the developed technologies are low cost. Recommendations for future works include improving the system for real-time monitoring, useful for data collection outside of a clinical setting.

Chapter 1 Introduction

Chapter Overview

The aim of this chapter is to familiarize the reader with lower extremity amputations, their causes and associated surgeries, general recovery strategies and the fabrication, function, implementation and problems with the long term use of prosthetic limb replacements. Following this, the currently available solutions used for dealing with lower limb complications will be presented to establish the need for new innovative solutions to these problems. Lastly, the new technologies developed towards monitoring lower limb prosthetics will be presented along with a general overview of currently available wireless passive magnetic sensors.

1.1 Background and Significance

An estimated 185,000 limb amputations occur each year [1], most commonly as a result of vascular and circulatory disease (82%), trauma (16.4%), cancer and malignancies (0.9%) and congenital conditions (0.8%) [2]. In addition to those, more than 1500 United States servicemen have had major limb amputations as a result of combat related injuries [3]. Lower-limb amputations make up the majority of these procedures and in 2005 roughly 1.025 million people in the United States were categorized as having had a lower-limb amputation [2]. Following such procedures, many patients are fitted with a prosthetic replacement and while a variety of prosthetic designs exist, they all need to distribute and absorb the forces which the lost limb would casually handle. Unfortunately, even with the incredible advancements in prosthetic technology over the last century, a study done by Johns Hopkins University in collaboration with the Amputee Coalition of America found that of 954 amputees surveyed, 70% reported that they experienced residual limb pain sometimes (45%) or all the time (23%) [4]. In addition to residual limb pain, prosthetic users are also at risk of developing blisters, cysts, ulcerations, deep tissue injury, etc. [5] resulting from forces experienced throughout the residuum [6]. A patient experiencing one or more of these problems may

be required to stop using their prosthetic until the residuum has healed and if healing does not occur, further amputations may be required [7].

Many of these issues can be prevented if the prosthetic is fitted properly and can be monitored constantly to avoid future problems. A number of systems have been developed for research purposes or for clinical settings as a tool to assist the fitting process. When monitoring patients with patellar tendon bearing sockets, for instance, most systems report a maximum stress of less than 220 kPa, but reports as high as 400 kPa have been published [8]. However, the ability to obtain results representative of a patient's day-to-day prosthetic use is often complicated by a variety of other parameters. For example, increases in temperature and the presence of moisture decrease the stiffness of the stratum corneum and the dermis. This causes tissue to experience greater overall elongation and strain because of applied loading [9]. Additionally, the duration of load application also affects the tissue's response. Testing on animals has shown that 13 kPa applied over 6 hours resulted in muscle necrosis while the same loading applied for 2 hours only resulted in ischemic histological changes in the tissue [9].

This work focuses on the development of new wireless passive monitoring systems capable of being incorporated into various portions of a prosthetic which could allow for monitoring over the lifetime of prosthetic use. The ability to instrument a system for long term use would not only provide patient specific data for researchers and orthotists, but would also be useful as a diagnostic tool capable of reporting on the applied loading to patient tissue in addition to the time period over which it was applied.

1.1.1 Causes of Amputation

Lower limb amputations occur for a variety of reasons; however, vascular and circulatory diseases, such as peripheral vascular disease (PVD), Diabetes Mellitus (DM) and Chronic Venous Insufficiency (CVI), are responsible for 82% of lower extremity amputations in the U.S. [2]. Of particular concern are patients with and conditions resulting from diabetes mellitus. As of 2008 it was estimated that DM was responsible for over half of the amputations in the United States and most of these amputations are of the lower limb [10]. Fortunately, in the United States the number of LEAs (lower extremity

amputations) related to DM has decreased from 11.2% in 1996 to 3.9% in 2009. However, even with this decrease, patients with DM are still 15 times more likely to have a LEA as compared to non-DM patients. Additionally, DM patients are most at risk from severe peripheral vascular disease [11] as well as ulcers and lower extremity neuropathies. As a matter of fact, even the occurrence of a prior amputation can increase the risk of secondary amputations [12]. Generally speaking, ischemia, resulting primarily from peripheral artery disease, is the primary cause of amputations resulting from a vascular or circulatory disease and in these cases an amputation may be necessary if revascularization has either failed or is not possible [13].

The second primary cause of LEA is trauma. While only accounting for 16.4% of LEAs [2], this could still be considered a significant minority cause of LEA and the national significance of this is especially seen in the increased number of combat related LEAs over the last decade. Recent overseas conflicts have led to an increase in the number of injuries in military personnel requiring amputation. Of particular importance is a distinct difference between the current and previous combat operations the U.S. has engaged in, mainly the use of improvised explosive devices (IEDs). In blast related injuries the primary causes of damage are the pressure wave from the blast interacting with tissue and organs, debris and physical movement of a person from the blast [14]. Typically, civilians experiencing lower extremity trauma do not experience blast related injuries. However, whether combat or non-combat related trauma, the primary concerns leading to amputation include open fracture with nerve injury, ischemia and soft tissue injury, to list a few [15]. Before moving to the next portion of this discussion it is worth noting that while malignancy and congenital defects are causes of LEAs, since they comprise less than 2% of all cases they will not be discussed here [2].

1.1.2 Amputation Procedure and Stump Formation

The actual procedure involved in removing a limb is approached from at least two general fronts: physiologically and psychologically. The primary focus here will be the physical aspect; however, the use of a prosthetic plays a critical role in recovery both psychologically and physically. In terms of the physical side of amputation, there are two

primary goals: 1) address the cause of the amputation and 2) reconstruct the remaining limb [16]. A primary factor in accomplishing both of these goals is the level of amputation**.** The amputation level will not only determine not the success of the procedure, but also the functional outcome for the patient. The effect of choosing one amputation level over another can then be described in terms of what will allow for the fastest patient recovery and the highest mobility given the condition of the patient's limb. This issue is complicated by the fact that transtibial amputations tend to result in more functional limbs, but also are more likely to require revision surgery while the opposite is true of transfermoral amputations [17].

In general then, the approach taken for the surgical procedure and determination of the amputation level can be summarized in terms of the makeup of the resulting residuum. The residuum of an amputee consists primarily of the skin surrounding the stump, the underlying muscle which makes up the bulk of the residuum and bone tissue over which the muscle is positioned and secured [16]. The skin of the residuum is one of the primary interfaces through which forces are transferred during ambulation and as a result must be capable of handling the stresses and strains experienced without rupturing, while still allowing for proper blood flow through the tissue. As a result, the condition of the soft tissue and the kind of flap that can be constructed using the available skin are prime factors in determining amputation level [18]. The second major component of the residuum is the muscle. Muscle tissue not only serves the purpose of allowing for ambulation in the remaining limb, but also is essential in providing proper padding to the residuum. The last major component of the residuum is the bone tissue. The bone acts as the interface between the artificially fashioned residuum and the rest of the body. As a result it is a primary point of force transfer and as such it is crucial that the remaining bone be shaped in order to eliminate rough or sharp edges and any protrusions that may result in high pressure and future complications [16]. Other important considerations for the actual procedure and construction of the stump include location of scar tissue, the shape of the stump, location and future effects of remaining nerves and specific surgical procedures such as the primary strategy employed in handling the muscle tissue [16].

This only represents a handful of the more noteworthy factors that must be taken into account with an amputation procedure.

1.1.3 Rehabilitation

The first phase of rehabilitation actually begins pre-operatively and primarily deals with preparing the patient psychologically. Prior to any surgical procedure it is important to discuss with the patient and their family the procedure that is going to be performed, expected outcomes, recovery times, etc. This relates to the fact that the loss of a limb will have drastic implications on the life and identity of a patient. As a result, providing proper expectations for short and long term recovery are essential [18].

Following pre-operative preparations and the actual surgery itself, patient rehabilitation focuses on two general goals, physical recovery and preparation for prosthetic use. The primary concerns in terms of physical recovery from the surgery include wound healing, controlling edema and postoperative pain and monitoring for infection [16]. Critically important to this process is the choice of dressings to use following surgery. Two types of dressings are primarily used: soft and rigid. Soft dressings are easy to apply and remove, can allow for regular inspection of wound healing and are compressible, which not only eliminates edema but also helps the maturation of the patient's stump. In comparison, rigid dressings carry the same benefits, and even more since the limb is better supported, with the primary concern being the inability to frequently check on the healing process as the removal and application of rigid dressings is a more involved process [16].

The second goal of early rehabilitation, preparation for prosthetic use, can be addressed almost immediately following surgery. While there is still debate on the usage of immediate post-operative prosthetics, the benefits to the patient both psychologically and physically can be quite advantageous. Psychologically, the use of a prosthetic immediately allows the patient to begin recovering and accepting their limb loss faster by minimizing the time period in which they are truly without any limb, artificial or otherwise. As a matter of fact, some studies have shown that this kind of early mobilization of the patient decreases pain and increases the overall recovery of the

patient. However, this must be balanced against the actual healing and maturation of the residuum. The integrity of the skin at the residuum is crucial to maintain if a patient is to have long term use of a prosthetic; additionally, over the course of initial rehabilitation the shape and volume of the stump will change as well [16]. As a result, the first year of patient recovery is crucial as a large amount of residual limb "maturation" will be occurring. It is recommended that during this time period temporary adjustable sockets and prosthetic liners be used, to artificially account for changes in volume and shape, until the stump is more or less fully mature [16].

1.1.4 General design and purpose of lower limp prosthetic

The primary goal of a lower limb prosthetic is to replace the functionality of the lost limb. One of the critical considerations to accomplishing this is how loads will be distributed onto the residuum. Commercially, three designs are commonly used: patellar tendon bearing sockets, hydrostatic sockets and total surface bearing sockets. The primary difference between the three types of prosthetics is the regions over which force is distributed. The patellar tending bearing socket (PTB) is designed such that forces are concentrated on the patellar tendon, medial flare of the tibia and the distal half of the stump while pressure relief occurs at the anterior distal aspect of the stump, over the crest of the tibia and the fibula head [19]. However, as a result of the limited load bearing regions [20] and lack of suspension at the residuum [21], PTB sockets risk placing too much load on the patellar tendon in addition to possibly causing a stretch effect on the soft tissue regions. Moreover, this can permit movement of stump tissue during use which may result in skin abrasion [21].

The total surface bearing (TSB) design was created in order to overcome the issues with the PTB sockets. A TSB socket differs from a PTB socket in two primary ways: suspension and load distribution. The TSB socket uses prosthetic liners to produce suction which maintains contact between the prosthetic and the patients' residuum. This was done in order to prevent movement during use and thus resolve abrasion and other issues which occur from movement during pistoning [22]. In addition to using suction suspension, the TSB socket design also uses the entire residuum as the weight bearing

surface, under the assumption that this will disperse loads more effectively and increase comfort [22]. However, while the TSB socket design does improve on some of the problems with the PTB socket, some studies have shown that TSB socket users are more prone to experience increased sweating, infection of hair follicles, pain from the shear forces of the liner on the stump and friction induced skin irritation at the knee [22].

The last type of prosthetic is the hydrostatic socket design, which is really just a different version of the TSB socket. In this design, a gel liner is utilized and casts are incorporated into the design in an attempt to produce equal distribution of force across the residuum. In a small study comparing PTB and hydrostatic sockets, 68% of patients preferred the hydrostatic socket due to more uniform load distributions, increases in the maximum knee flexion and an increased capacity to feel the weight of the lower limb. However, this design is not suitable for patients with long residual limbs, those who are likely to greatly perspire and those prosthetic users who are not capable of putting on a distal suspension prosthesis [23].

1.1.5 Issues with Prosthetic Use and Current Solutions

The long term health of a patient's stump is a primary concern over the course of the device's lifetime. When considering the stump-socket interface, a variety of parameters must be taken into account including distribution of force, maintaining total contact and prevention of movement during pistoning. Interestingly, the primary difficulty in maintaining these parameters comes from the patient because the process of designing and fitting a prosthetic cannot take into account the physiological changes that will occur in the stump over the patient's lifetime. For instance, even a 3%-5% change in the volume of a patient's stump can result in difficulty for the patient in donning the prosthetic [24]. Additionally, these changes in volume cause skin breakdown as well [25]. A variety of technologies have been developed to avoid issues like this, including those unrelated to changes in patient physiology.

The first preventative measure to maintain health of the residuum is a properly fit and designed prosthetic. To accomplish this, technologies capable of providing quantitative analysis of force distribution during the fitting process have been developed. For instance, the Rincoe Socket Fitting System, Tekscan F-Socket Pressure Measurement System and the Novel Pliance 16P System are all commercially available pressure mapping systems aimed at ensuring a properly fit prosthetic by providing quantitative information on the force distribution between the patient stump and prosthetic [8]. The Tekscan F-Socket and the Rincoe Socket Fitting System measure pressure using a force-sensitive resistive sensor array while the Novel Pliance System utilizes capacitive sensors [8]. Additionally, the Rincoe and Tekscan systems have also been deployed as research tools in various studies to observe, for example, the effects of thigh lacer suspension in reducing socket pressure [26].

With a properly fit prosthetic, the challenge then becomes maintaining proper force distribution and fit. To that end, common practices such as using prosthetic sleeves and liners have been reported to improve suspension and comfort [27], but their effectiveness in terms of prevention of ulceration and other related issues is mixed [28]. In addition, a variety of smart prosthetics have also been developed to maintain force distribution and fit. For instance, a prosthetic capable of changing volume and hardness was developed to account for alterations in stump volume and misalignment issues. The system incorporates bags filled with Magneto-Rheological fluid into the prosthetic. Hardness is altered as a result of changes in fluid viscosity in response to an external magnetic field, while volume can be controlled by inserting or removing the Magneto-Rheological fluid. However, while the device was reported to function better than a TSB socket in a single patient trial, this system represents a major redesign of current socket systems [29].

Even with these practices and developing technologies, monitoring and identifying the loads on the residuum is still critical to maintain the long term health of the lower limb. There are a variety of methods which can be used to try and determine the

interface loads in a lower-limb prosthetic: computational models (such as finite element analysis), imaging techniques (such as computer tomography), and direct measurement techniques (such as those using capacitors and strain gauges). Computational FE modeling is most often carried out with one of three commonly used mathematical models: linear static, nonlinear or dynamic finite element [8]. Linear static models assume material properties to be linear and ignore slip and interface friction, making them the simplest to use but least realistic of the modeling techniques. A nonlinear model, as its name implies, does not assume linear material properties and takes into account slip and interface friction; however, the model lacks the capacity for dynamic analysis. Dynamic models make few assumptions and allow for complex dynamic analysis of properties such as inertia [8]. These models frequently assist in analysis of interface pressures, examination of the effects of design alterations on prosthetics, and are useful for investigating new designs without having to spend money to manufacture a prototype [30]. However, these models must be verified with experimental testing and in order to produce accurate models, additional information such as geometry, material properties, load state, and boundary conditions must be obtained [30]. Moreover, finite element models provide no long term continuous patient care.

Imaging techniques, such as computed tomography (CT), provide noninvasive methods for assisting in development of better fitting prostheses while also allowing access to otherwise unattainable internal views of the residuum. For instance, CT imaging directly influences the production of prosthetics by guiding the manufacturing process through the coupling of individual patient scans with computer aided design/computer aided manufacturing (CAD/CAM) systems. However, CT scans inherently exclude dynamic analysis and can suffer from issues if the patient moves during imaging [31]. Some of these limitations can be overcome by combining this technology with other techniques such as x-ray, which demonstrated enough accuracy and precision for use in distance and static volumetric quantitative socket-fitting research [31].

Pressure measurement devices determine interface loads through monitoring of either discrete focal forces or pressure distributions [8]. Examples of discrete measurement devices include diaphragm deflection strain gauges, fluid-filled sensors, printed circuit sheets, etc. [29]. However, these systems have the distinct disadvantage of not only being limited to measuring force at a point, but also have finite thicknesses and often times require modifications to the prosthetic in order to accommodate the sensing device [8]. While several commercially available sensors from this category, such as the Kulite diaphragm deflection strain gauge, exist, these systems exhibit numerous limitations. For example, a report on the Kulite sensor explained that a cotton cloth placed over the device can dramatically change the observed measurements [8]. Moreover, these devices usually require direct connections to electronics, limiting their usefulness for ambulatory force monitoring.

Pressure distribution, or mapping, systems often utilize an array of sensors in a mat form to allow for accurate fitting of prosthetics [8]. Currently available commercial systems frequently used to assist in socket fitting include the Rincoe Socket Fitting System, Tekscan F-Socket Pressure Measurement System and the Novel Pliance 16P System [8]. The Tekscan F-Socket and the Rincoe Socket Fitting System measure pressure as a function of the response of arrays of force-sensitive resistive sensors while the Novel Pliance System utilizes capacitive sensors [8]. The Rincoe and Tekscan systems have been reported for use clinically and in a variety of studies, including those involving measurement of static and dynamic pressures at the stump interface and observation of the effects of thigh lacer suspension in reducing socket pressure [26]. These systems require the insertion of multiple thin pads into a socket and allow for real time monitoring of the patient while in ambulation, but are not designed for long term monitoring.

While few transducer based systems are reported for long term monitoring of the socket-stump interface, some research and development has been reported towards this end. In particular, a sensor system for wireless long term continuous monitoring was

reported [32]. The system utilized a commercial transducer attached to a custom leg-prosthesis manufactured to mimic the normal prosthesis of a test patient, with the transducer connected below the cup containing the socket-residuum interface. A wireless modem attached to the transducer allowed for transmission of sensor data with a reported range of more than 700 m outdoors and was capable of monitoring loading in the *x*, *y* and *z* axis. Additionally, the system measured moments acting on the prosthesis during a variety of activities [32]. However, even though the system is capable of wirelessly collecting a variety of information, it requires the prosthesis to be redesigned to accommodate the transducer and does not collect data directly from the socket-stump interface.

1.2 Magnetic Sensors

Wireless, passive sensing systems lack battery lifetime issues and in terms of embedding and placement are only limited by the capacity to receive a signal from a device. As a result, a variety of magnetic based sensing systems have been developed. For instance, magnetic materials with magnetic properties that can change depending on external stimuli, such as those reported on later in this chapter, have been widely used towards a variety of sensing applications. In addition to tailoring magnetic materials to various sensor applications, magnetic circuit elements have also been developed for wireless passive sensing. For instance, inductive capacitive (LC) circuits are comprised of an inductive element, such as a spiral inductor, and a capacitive element, such as an interdigitated or digital capacitor. By monitoring the impedance of an external coil loop antenna, the frequency of the peak resonance of the circuit can be observed [33]. Using this technology a sensor was developed for monitoring moisture content in concrete. The device consisted of a seven turn rectangular spiral inductor connected to an interdigitated capacitor [33]. When placed in a moist environment, the capacitance of the resonant circuit increased causing a decrease in the frequency of the peak resonance. By relating this shift in frequency to moisture content, the sensor was able to determine the water

content in drying concrete with a maximum error of less than 10% [33]. The same design has also been deployed for monitoring moisture in dried foods and even for bacteria monitoring [34, 35].

A downside to the use of these materials and magnetic circuit elements is that they must be tailored to their target application, unlike more versatile sensor platforms like RF-based sensors which can be used as energy harvesters for other coupled devices. Radio Frequency based energy harvesting systems take advantage of inductive coupling to not only provide power to an attached device, but also to allow for the sending and receiving of data to and from a device. Specifically, an external source produces a high frequency RF field which is then picked up by a receiving antenna and converted from a RF signal into a current and voltage through inductive coupling [36]. For instance, a wireless, passive implantable blood pressure monitoring system was developed [37]. The system utilized a pressure cuff filled with a low-viscosity silicone oil coupled to a MEMS capacitive pressure sensor to monitor blood flow in lab mice. RF energy harvesting was used as the power source for the onboard electronics and, as a whole, the system had a resolution of 1 mmHg [37]. However, the need to connect a RF component to a sensor increases the complexity of the fabricated device and necessarily its size as well.

1.2.1 Wireless Sensors based on Magnetoelasticity

Of interest to the presented work is a specific magnetic phenomenon known as magnetoelasticity, which describes the effects of applied magnetic fields on the physical properties of a material and *vice versa*. For instance, a magnetic material placed under an applied tensile or compressive load will, depending on its magnetostriction, experience a change in magnetization, referred to as the Villari effect [38]. At the same time, an unstressed magnetic material can experience a stress caused by an applied magnetic field, referred to as the Joule effect [38]. These properties, when found in magnetoelastic and magnetostrictive magnetic materials with low remanence and coercivity, have been utilized as the base sensing mechanism for a large variety of monitoring platforms. Presented in the following section is a broad overview of magnetoharmonic and

magnetoelastic resonance sensors making use of magnetoelastic films as their primary sensing component.

1.2.2 Magnetoharmonic Sensors

Soft magnetic materials have been utilized as wireless, passive sensing platforms by monitoring changes in the higher-order harmonic fields produced by the material. Specifically, when exposed to an AC magnetic field, soft magnetic materials magnetize and generate higher-order field components (see **Figure 1.1**) [39] whose amplitudes depend on an applied DC biasing field [39]. This phenomenon is due to the nonlinear magnetization of soft-magnetic materials, visualized in the *BH* loop (**Figure 1.2**). The result of applying an AC signal to a material which operates according to the *BH* loop in **Figure 1.2** is a distorted sine wave, whose components can be deconstructed using a Fourier transformation. By performing a DC biasing sweep, the effect of this nonlinear magnetization as a function of the changes in the amplitude of different frequency components can be visualized (see **Figure 1.2**), and are referred to as the higher-order harmonics [39]. Sensors have been designed using the higher-order harmonics by monitoring peak amplitudes of the higher-order harmonics or the bias field at which the minimum sensor response occurs. These properties of the higher order harmonics are affected by stimuli such as stress, temperature, corrosion and additional DC field sources, thus allowing for a variety of sensing platforms to be developed. The developed sensor platforms can be categorized as either single or multi-element depending on whether or not they utilize a hard magnetic biasing element in addition to the soft magnetic sensing material [23].

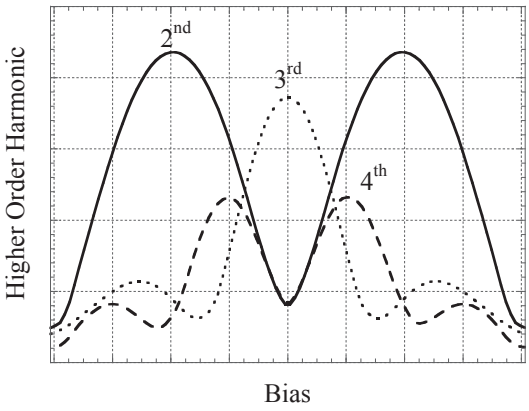

Figure 1.1 Higher-order field components of a magnetically soft material.

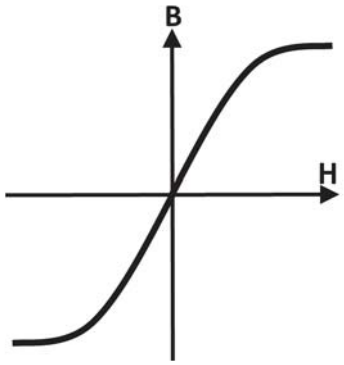

Figure 1.2 The *BH* loop describes the induced magnetization in terms of applied field.

When the primary component used for sensing is a strip of magnetic film (referred to as a single element sensor), the most common property observed is the peak amplitude of the higher order harmonic. The magnitude of the peak amplitude will change as a result of stress, temperature and even corrosion due to changes in sensor permeability. The stress sensitivity of the higher-order harmonic is known as the Villari effect and is not only dependent upon the value of the applied stress, but also the magnetostriction of the material. A material with positive magnetostriction, such as Metglas 2826 MB [40], exhibits an increase in permeability, while Metglas 2605SC, with negative magnetostriction, experiences a decrease in permeability with applied tensile stress [40]. These sensors have been reported for monitoring forces on biomedical

instruments [41], but can also be used for monitoring chemicals with the addition of a coating that swells, and thus stresses the sensor, in response to a target of interest [42]. Additionally, single sensing strips have been reported for multipoint force monitoring. It was found that the application of force to the front and back halves of a magnetoelastic strip could be monitored by capturing the amplitude of the higher harmonic while monitoring from the front and back of the magnetoelastic strip. The effect of applying a load to either region was to effectively alter the permeability of both halves of the strip. By monitoring the signal on either end of the strip under various loading conditions, a multipoint force sensor was then fashioned [41].

Similar to the Villari effect, the effects of temperature on the higher-order harmonics are also material dependent. Specifically, Metglas 2605SC illustrated an increase in amplitude with increasing temperature, Metglas 2826MB exhibited a decrease in response and Metglas 2714A illustrated almost no sensitivity to temperature. This is likely due to the magnetostriction of the materials, with Metglas 2714A having almost zero magnetostriction [39]. While the effects of stress and temperature on the higher order harmonics can vary drastically with material properties, corrosion causes a decrease in permeability regardless of the material in use. In this case, the sensor is physically losing magnetizable material and the result is a decrease in the observed amplitude of the higher-order harmonics [39].

The second commonly used configuration for sensors which monitor changes in the higher order harmonics utilize a permanent magnet (biasing element) in addition to a soft magnetic strip (sensing element). When the biasing element is placed near the sensing strips, an observed shift occurs in the higher-order harmonics. This allows for the fabrication of a variety of sensor platforms. For instance, by adhering the biasing element to a flexible membrane placed at a distance from a sensing strip, wireless passive pressure, stress/strain and glucose sensors have been fabricated. In the case of pressure [43] or stress/strain [44] monitoring, applied pressure deflects the membrane, moving the biasing element closer to the sensing strip. As the separation distance between the sensing and biasing elements decreases, the DC field experienced by the sensing strip increases, resulting in a shift in the higher-order harmonics [43]. In addition to monitoring of

ambient pressure [43], this design was also used to monitor pressure in a liquid-flowing conduit [45]. Moreover, the two element design was further developed and *in vivo* testing was performed on mice as a step towards the fabrication of a wireless passive sensor for monitoring the sphincter of Oddi in humans [46].

To monitor glucose a similar setup comprised of a sensing strip separated from a biasing element adhered to a flexible substrate was used. However, in this application deflection was achieved by using the flexible membrane as part of a mostly sealed chamber with one end being coated with a glucose sensitive substance. When glucose is introduced into the system, a reaction occurs at the coating which results in the consumption of oxygen in the chamber on the other side. The depletion of oxygen produces a negative pressure in the chamber causing the membrane to deflect inward, away from the sensing element. The change in separation distance between the sensing and biasing elements is then observed as a shift in the higher harmonic [47].

A flow sensor was also developed using the two-element design. In this case, instead of using a flexible membrane, the sensing strip is effectively utilized as its own flexible membrane. More specifically, a biasing element was adhered to one wall of a flow channel and a sensing strip was then positioned opposite the biasing strip at an angle such that a flowing liquid would deflect the sensing element away from the biasing element. This resulted in an observed shift in the higher order harmonic [48].

Reported in this work is the development of the previously mentioned multi-point stress/strain single element magnetoharmonic sensing system. Described in the following section is the second magnetic based sensing technology that was developed.

1.2.3 Magnetoelastic Resonance Sensors

Magnetoelastic resonance sensors, just simply magnetoelastic sensors, take advantage of the magnetostrictive properties of certain magnetic materials. A magnetostrictive material exhibits a change in dimensions when placed inside a magnetic field. Of particular interest are magnetoelastic sensors. Typically made from amorphous metallic glasses [49], these materials are capable of being excited using an externally applied time varying magnetic field, or using a pulse, such that the material experiences

longitudinal vibrations [49]. These vibrations produce a secondary magnetic flux, due to the coupling between the magnetic and mechanical energies of the material, which reaches a peak when the applied excitation field's frequency matches the material's mechanical resonance according to [50]:

$$f_0 = \frac{1}{2L}\sqrt{\frac{E}{\rho(1-\sigma^2)}} \tag{1}$$

where f_0 is the resonant frequency, L is the strip length, E is the sensor Young's modulus, ρ is the sensor density and σ is the Poisson's ratio. The changes in both the longitudinal vibrations and the secondary magnetic flux allows for this sensor to be monitored acoustically using a microphone, magnetically using a sensing coil or optically using a laser emitter and phototransistor [49]. Additionally, because the observed resonant frequency is heavily dependent upon the length of the sensor, an array of magnetoelastic sensors can be monitored using a single detection source as long as each sensor has a different length.

When used for sensing, the resonant frequency is typically the monitored parameter since it is relatively independent of the distance from the excitation and detection systems [49]. However, regardless of which method is used to monitor the sensor's response, both the frequency and amplitude of the resonance can be made sensitive for a variety application. It is worth noting that that the majority of the sensors described here behave according to two assumptions: 1) any applied mass is significantly less than the mass of the strip itself and 2) loading, or the addition of mass, is applied equally over the surface of the sensor [51]. While some sensors have been reported for non-uniform loading [49], few sensors have been reported which can function outside of both assumptions.

Many magnetoelastic sensors allow for monitoring of their targets based on a change in the observed resonant frequency or amplitude as a result of an applied mass to the sensor surface according to [49]:

$$\Delta f = -f_0 \frac{\Delta m}{2m_0} \tag{2}$$

where f_0 is the initial resonance frequency, m_0 is the sensor mass and Δm is the applied mass loading. The applied loading dampens the longitudinal vibrations resulting in a decrease in the resonant frequency. In the case of monitoring chemical concentrations or pH, a mass-changing coating is typically applied to the sensor surface. When exposed to the target of interest, these coatings will swell resulting in an increase in the applied mass on the sensor. Several examples include Metglas 2826MB strips coated with poly(acrylic acid-co-isocytlacrylate) for monitoring ammonia [51], pSPMA-IOA and pAA-IOA for salt independent pH monitoring [52] and co-immobilized glucose oxidase and catalyze along with a pH-sensitive polymer for monitoring glucose concentrations [53]. Unlike the monitoring of chemical concentrations and pH, magnetoelastic sensors aimed at monitoring biological targets must have their sensor surfaces functionalized towards a biological target of interest. Some biological targets monitored using functionalized magnetoelastic sensors include avidin [54], *Bacillus anthracis* (responsible for anthrax) [55], *Salmonella typhimurium* [56] and *Escherichia coli* O157:H7 [57].

The resonant frequency of a sensing strip is also sensitive to the viscosity/density of a medium with which it is in contact according to [49]:

$$\Delta f = \frac{\sqrt{\pi f_0}}{2\pi\rho_s d}\sqrt{\eta\rho_l} \tag{3}$$

where η is the viscosity and ρ_l is the density of the surrounding medium. Specifically, as a medium's density/viscosity changes the shear stress on the longitudinal vibrations of the sensor, from the medium, is altered, resulting in a shift in the resonant frequency [58]. Using this principle sensors for monitoring blood coagulation [59], accumulation of sludge in biliary stents [60] and oil as an on line viscometer [61] have been developed.

Pressure can be monitored using magnetoelastic sensors; however, when monitoring pressure a modification to the sensor must occur. By itself, a ribbon magnetoelastic sensor has no sensitivity to pressure since the shear waves of the longitudinal vibrations do not propagate through a gas media [62]. The sensor can be made to be pressure sensitive by stressing the sensor elastically or plastically, for instance permanently deforming the sensor through dimpling which produces out of plane vibrations. An applied increase in pressure then results in a decrease in the resonant

frequency due to a damping of the out of plane vibrations [62]. Another means of monitoring pressure using a magnetoelastic sensor involves fabricating a sensor such that an applied pressure changes the distance between the resonating sensor and a hard magnetic material. As the applied pressure forces the hard magnetic material, often attached to a flexible membrane or substrate, closer to the resonating strip, the increase in applied DC field causes a shift in the resonant frequency, allowing for monitoring of ambient pressure [63].

Temperature can also be monitored using magnetoelastic sensors. It has been shown that the Young's modulus of many materials used as magnetoelastic sensors are temperature dependent. As a result, a change in the ambient temperature will alter the resonant frequency as would be expected from Eq. (1) [49]. Another means by which temperature can be monitored is through the use of a temperature sensitive coating. Similar to a mass sensitive coating, a thermally sensitive coating will expand with increasing temperatures, resulting in a strain on the sensor and a shift in the resonant frequency [64]. However, the temperature dependence of a magnetoelastic sensor is also affected by the applied DC biasing field. In fact, it has been demonstrated that by altering the applied DC biasing field the sensitivity of a magnetoelastic sensor to temperature can be modified to be positive, negative or even neutral [65].

Magnetoelastic sensors have also been developed for identifying the elastic modulus of thin films coated onto the sensor surface. Typically, when a coating is applied to a magnetoelastic sensor the purpose is to sensitize the sensor to a target of interest. However, by applying a thick enough coating the Young's modulus of the magnetoelastic sensor becomes modified by the Young's modulus of the applied coating. This has the effect of altering the longitudinal vibrations traveling through the material. By comparing the known response of an uncoated magnetoelastic sensor to the coated sensor, the Young's modulus of the applied material can be determined. This has been done by sweeping the DC biasing field in order to find the minimum response along the ΔE curve, which is a plot of the change in resonant frequency against the applied DC field. The frequency at which this minimum occurs can be compared for the coated and uncoated sensors, allowing for a determination of the coating's Young's modulus [66].

While not representing a new means or type of magnetoelastic resonance sensor, it is worth explaining that even though the majority of magnetoelastic sensors typically only monitor the first order harmonic, because it has the largest signal, a multi-element single strip sensor can be fashioned. Specifically, a magnetoelastic resonating thin film exhibits resonant peaks at whole number intervals of the fundamental resonant frequency. These higher-order modes are not typically investigated due to the fact that the higher-order modes have a weaker resonant response. Additionally, the majority of applications involving magnetoelastic sensors use individual strips to monitor a single target and thus have no need for the higher harmonics [67]. While few applications have been reported which take advantage of the higher harmonic resonance modes, a mass sensor was reported which made use of them [67]. Specifically, gold was sputtered at the position/positions of peak vibration for the 1^{st} and 2^{nd} resonant modes. Results indicated that applied coatings caused a decrease in the resonant frequency of the relevant resonance mode with little to no effect on the other resonant peak. This would allow for multiple targets to monitored using a single magnetoelastic strip [67]. However, the applied masses were still significantly lower than the mass of the strip itself, distinguishing this work from the sensors presented in the following chapters.

It is worth noting again that with the exception of sensing applications involving temperature, all of the presented sensors, which broadly covers the scope of magnetoelastic resonance sensors, function according to one or more assumptions or practiced limitations: 1) Any applied mass is significantly less than the mass of the strip, 2) Any applied coating is equally distributed over the sensor's surface and 3) only the first harmonic is of interest. Reported in this work is a new magnetoelastic resonating sensor platform which has been shown capable of being monitored with applied loads significantly higher than the mass of the strip and that does not require the applied loading be equally distributed over the sensor surface.

1.3 Overview of Chapters

The focus of the presented work is the development of two magnetic based force monitoring systems. **Chapter 1** focuses on familiarizing the reader with the chosen target

application for these technologies, mainly monitoring of lower limb prosthetics. Additionally, overviews of currently available magnetic sensing systems with the same fundamental sensing mechanisms as the reported technologies are also presented to also illustrate the novelty and uniqueness of the presented systems. **Chapter 2** builds on the overview of magnetic based sensors by delving into the theories governing the development sensor platforms. **Chapter 3** presents the foundational work with the first of the reported systems, the magnetoelastic resonance load sensor. The aim of this chapter is to describe the initial testing and findings regarding the use of resonating magnetoelastic sensors for load monitoring. This research provides the basis for work presented in **Chapter 4**, which covers the characterization and initial testing of a multi-element sensing array. **Chapter 5**, in a similar manner to **Chapter 4**, presents the initial work in developing the magnetoharmonic based sensing technology. The work performed on a three strip array adhered to a hard surface has allowed for investigations into the use of a single strip as a multi-element force sensor, presented in **Chapter 6**, which specifically reports on the characterization and deployment of this technology onto a portion of a lower limb prosthetic donated by Northern Orthotics Inc. **Chapter 7** presents future work to be performed with the magnetoelastic resonance sensing technology. Lastly, **Chapter 8** concludes the dissertation by summarizing the findings and future works.

*Reference*s

1. Ziegler-Graham, K., MacKenzie, E.J., Ephraim, P.L., Travison, T.G., and Brookmeyer, R., *Estimating the prevalence of limb loss in the United States: 2005 to 2050.* Arch Phys Med Rehabil, 2008. **89**(3): p. 422-429.
2. *Standard of Care: Lower Extremity Amputation. The Brigham and Women's Hospital Inc., Department of Rehabilitation Services, 2011.*
3. Fischer, H., *U.S. Military Casualty Statistics: Operation New Dawn, Operation Iraqi Freedom, and Operation Enduring Freedom*. February 5, 2013.
4. The Limb Loss Research and Statistics Program Johns Hopkins Bloomberg School of Public Health and Amputee Coalition, *People With Amputations Speak Out*, 2006, Amputee Coalition of America.
5. Sanders, J.E., Greve, J.M., Mitchell, S.B., and Zachariah, S.G., *Material properties of commonly-used interface materials and their static coefficients of friction with skin and socks.* J Rehabil Res Dev, 1998. **35**(2): p. 161-76.

6. Sanders, J.E. and Daly, C.H., *Normal and shear stresses on a residual limb in a prosthetic socket during ambulation: comparison of finite element results with experimental measurements.* J Rehabil Res Dev, 1993. **30**(2): p. 191-204.
7. Sanders, J.E., *Interface mechanics in external prosthetics: review of interface stress measurement techniques.* Medical and Biological Engineering and Computing, 1995. **33**(4): p. 509-516.
8. Mak, A.F., Zhang, M., and Boone, D.A., *State-of-the-art research in lower-limb prosthetic biomechanics-socket interface: a review.* J Rehabil Res Dev, 2001. **38**(2): p. 161-174.
9. Sanders, J.E., Goldstein, B.S., and Leotta, D.F., *Skin response to mechanical stress: adaptation rather than breakdown-a review of the literature.* Journal of rehabilitation research and development, 1995. **32**: p. 214-214.
10. Staff, N., *Diabetes and Lower Extremity Amputations*. 2008, Amputation Coalition of America.
11. Pecoraro, R.E., Reiber, G.E., and Burgess, E.M., *Pathways to diabetic limb amputation. Basis for prevention.* Diabetes Care, 1990. **13**(5): p. 513-521.
12. Adler, A.I., Boyko, E.J., Ahroni, J.H., and Smith, D.G., *Lower-extremity amputation in diabetes. The independent effects of peripheral vascular disease, sensory neuropathy, and foot ulcers.* Diabetes Care, 1999. **22**(7): p. 1029-1035.
13. Kalapatapu, V. *Lower Extremity Amputation.* 2014; Available from: http://www.uptodate.com/contents/lower-extremity-amputation#H1576691758.
14. *Blast Injuries.* New England Journal of Medicine, 2005. **352**(25): p. 2651-2653.
15. Zaretsky, H.H., Steven R. Herbert, and Alex Moroz., *Medical Aspects of Disability: A Handbook for the Rehabilitation Professional*. 4 ed. 2010, New York, NY: Springer Publishing Company. 784.
16. Smith, D.G., Michael, J.W., Bowker, J.H., and Surgeons, A.A.o.O., *Atlas of amputations and limb deficiencies: surgical, prosthetic, and rehabilitation principles*. 2004: American Academy of Orthopaedic Surgeons Rosemont, IL.
17. Campbell, W.B., St Johnston, J.A., Kernick, V.F., and Rutter, E.A., *Lower limb amputation: striking the balance.* Ann R Coll Surg Engl, 1994. **76**(3): p. 205-209.
18. Esquenazi, A., *Amputation rehabilitation and prosthetic restoration. From surgery to community reintegration.* Disabil Rehabil, 2004. **26**(14-15): p. 831-836.
19. Cooper, P.F.P.a.R.A., *Care of the combat amputee*. 2009, Falls Church, VA: Office of the Surgeon General, United States Army.
20. Yigiter, K., Sener, G., and Bayar, K., *Comparison of the effects of patellar tendon bearing and total surface bearing sockets on prosthetic fitting and rehabilitation.* Prosthet Orthot Int, 2002. **26**(3): p. 206-212.
21. Hachisuka, K., Dozono, K., Ogata, H., Ohmine, S., Shitama, H., and Shinkoda, K., *Total surface bearing below-knee prosthesis: Advantages, disadvantages, and clinical implications.* Archives of Physical Medicine and Rehabilitation, 1998. **79**(7): p. 783-789.
22. Selles, R.W., Janssens, P.J., Jongenengel, C.D., and Bussmann, J.B., *A randomized controlled trial comparing functional outcome and cost efficiency of a total surface-bearing socket versus a conventional patellar tendon-bearing socket in transtibial amputees.* Arch Phys Med Rehabil, 2005. **86**(1): p. 154-61; quiz 180.

23. *Prosthetic & Orthotic Update.* Nobbe Orthopedics, Inc., 2003. **36**.
24. Greenwald, R.M., *Volume Management: Smart Variable Geometry Socket (SVGS) Technology for Lower-Limb Prostheses.* American Academy of Orthotists and Prosthetists, 2003. **15**(3).
25. Fatone, S. and Sanders, J.E., *Residual limb volume change: systematic review of measurement and management.* Journal of Rehabilitation Research & Development, 2011. **48**: p. 949-986.
26. Polliack, A.A., Craig, D.D., Sieh, R.C., Landsberger, S., and McNeal, D.R., *Laboratory and clinical tests of a prototype pressure sensor for clincial assessment of prosthetic socket fit.* Prosthet Orthot Int, 2002. **26**(1): p. 23-34.
27. Baars, E.C. and Geertzen, J.H., *Literature review of the possible advantages of silicon liner socket use in trans-tibial prostheses.* Prosthet Orthot Int, 2005. **29**(1): p. 27-37.
28. Meulenbelt, H.E., Dijkstra, P.U., Jonkman, M.F., and Geertzen, J.H., *Skin problems in lower limb amputees: a systematic review.* Disabil Rehabil, 2006. **28**(10): p. 603-608.
29. Ogawa, A., Obinata, G., Hase, K., Dutta, A., and Nakagawa, M., *Design of lower limb prosthesis with contact pressure adjustment by MR fluid.* Conf Proc IEEE Eng Med Biol Soc, 2008. **2008**: p. 330-333.
30. Silver-Thorn, M.B., Steege, J.W., and Dudley, S.C., *A review of prosthetic interface stress investigations.* Journal of Rehabilitation Research and Development, 1996. **33**: p. 13.
31. Papaioannou, G., Mitrogiannis, C., Nianios, G., and Fiedler, G., *Assessment of amputee socket-stump-residual bone kinematics during strenuous activities using Dynamic Roentgen Stereogrammetric Analysis.* J Biomech, 2010. **43**(5): p. 871-878.
32. Frossard, L., Beck, J., Dillon, M., and Evans, J., *Development and Preliminary Testing of a Device for the Direct Measurement of Forces and Moments in the Prosthetic Limb of Transfemoral Amputees During Activities of Daily Living.* Journal of Proceedings, 2003. **15**(4): p. 135-142.
33. Ong, J.B., Zhanping, Y., Mills-Beale, J., Ee Lim, T., Pereles, B.D., and Ong, K.G., *A Wireless, Passive Embedded Sensor for Real-Time Monitoring of Water Content in Civil Engineering Materials.* Sensors Journal, IEEE, 2008. **8**(12): p. 2053-2058.
34. DeRouin, A., Pereles, B., Sansom, T., Zang, P., and Ong, K.G., *A Wireless Inductive-Capacitive Resonant Circuit Sensor Array for Force Monitoring.* Journal of Sensor Technology, 2013. **3**(3): p. 63-69.
35. Silva, M.T.P. and Vasconcelos, F.H., *Temperature Sensing System With Short-Range Wireless Sensor Based on Inductive Coupling.* Sensors Journal, IEEE, 2011. **11**(10): p. 2469-2478.
36. Ong, K.G., Wang, J., Singh, R.S., Bachas, L.G., and Grimes, C.A., *Monitoring of bacteria growth using a wireless, remote query resonant-circuit sensor: application to environmental sensing.* Biosensors and Bioelectronics, 2001. **16**(4–5): p. 305-312.
37. Peng, C., Chaimanonart, N., Ko, W.H., and Young, D.J., *A Wireless and Batteryless 10-Bit Implantable Blood Pressure Sensing Microsystem With Adaptive RF Powering for Real-Time Laboratory Mice Monitoring.* Solid-State Circuits, IEEE Journal of, 2009. **44**(12): p. 3631-3644.

38. Calkins, F.T., Flatau, A.B., and Dapino, M.J., *Overview of Magnetostrictive Sensor Technology.* Journal of Intelligent Material Systems and Structures, 2007. **18**(10): p. 1057-1066.
39. Ong, K.G. and Grimes, C.A., *Tracking the harmonic response of magnetically-soft sensors for wireless temperature, stress, and corrosive monitoring.* Sens Actuators A Phys, 2002. **101**(1-2): p. 49-61.
40. Ong, K.G. and Grimes, C.A., *Magnetically soft higher order harmonic stress and temperature sensors.* Magnetics, IEEE Transactions on, 2003. **39**(5): p. 3414-3416.
41. Pereles, B.D., DeRouin, A.J., and Ong, K.G., *A Wireless, Passive Magnetoelastic Force–Mapping System for Biomedical Applications.* Journal of Biomechanical Engineering, 2013. **136**(1): p. 011010-011010.
42. Ong, K.G., Paulose, M., and Grimes, C.A., *A Wireless, Passive, Magnetically-soft Harmonic Sensor for Monitoring Sodium Hypochlorite Concentrations in Water.* Sensors, 2003. **3**(1): p. 11-18.
43. Pereles, B.D., Shao, R., Tan, E.L., and Ong, K.G., *A Remote Query Pressure Sensor Based on Magnetic Higher Order Harmonic Fields.* Sensors Journal, IEEE, 2008. **8**(11): p. 1824-1829.
44. Ong, K.G., Tan, E.L., Pereles, B., and Horton, B. *Wireless, magnetic-based sensors for biomedical applications*. in *Engineering in Medicine and Biology Society, 2009. EMBC 2009. Annual International Conference of the IEEE*. 2009.
45. Tan, E.L., Pereles, B.D., Shao, R., and Ong, K.G., *A Wireless and Passive Implantable Pressure Sensor, Sensor Letters.* Sensor Letters, 2009. **7**(1): p. 57-63.
46. Tan, E.L., DeRouin, A.J., Pereles, B.D., and Ong, K.G., *Design, Fabrication, and Implementation of a Wireless, Passive Implantable Pressure Sensor Based on Magnetic Higher-Order Harmonic Fields.* Biosensors, 2011. **1**(4): p. 134-152.
47. Thorp, C.E., Pereles, B.D., DeRouin, A.J., and Ong, K.G., *A Wireless, Passive Chemo-Mechanical Glucose Sensor.* IEEE Sensors Journal, 2011. **11**(9): p. 2027-2031.
48. Pereles, B.D., Shao, R., Tan, E.L., and Ong, K.G., *A wireless flow sensor based on magnetic higher-order harmonic fields, Smart Materials and Structures.* Smart Materials and Structures, 2009. **18**(9).
49. Grimes, C.A., Roy, S.C., Rani, S., and Cai, Q., *Theory, instrumentation and applications of magnetoelastic resonance sensors: a review.* Sensors (Basel), 2011. **11**(3): p. 2809-2844.
50. Jain, M.K., Cai, Q., and Grimes, C.A., *A wireless micro-sensor for simultaneous measurement of pH, temperature, and pressure.* Smart Materials and Structures, 2001. **10**(2).
51. Cai, Q.Y., Jain, M.K., and Grimes, C.A., *A wireless, remote query ammonia sensor.* Sensors and Actuators B: Chemical, 2001. **77**(3): p. 614-619.
52. Cai, Q.Y. and Grimes, C.A., *A salt-independent pH sensor.* Sensors and Actuators B: Chemical, 2001. **79**(2–3): p. 144-149.
53. Gao, X., Yang, W., Pang, P., Liao, S., Cai, Q., Zeng, K., and Grimes, C.A., *A wireless magnetoelastic biosensor for rapid detection of glucose concentrations in urine samples.* Sensors and Actuators B: Chemical, 2007. **128**(1): p. 161-167.

54. Ruan, C., Zeng, K., Varghese, O.K., and Grimes, C.A., *A magnetoelastic bioaffinity-based sensor for avidin.* Biosensors and Bioelectronics, 2004. **19**(12): p. 6.
55. Wan, J., Johnson, M.L., Guntupalli, R., Petrenko, V.A., and Chin, B.A., *Detection of Bacillus anthracis spores in liquid using phage-based magnetoelastic micro-resonators.* Sensors and Actuators B: Chemical, 2007. **127**(2): p. 559-566.
56. Lakshmanan, R.S., Guntupalli, R., Hu, J., Petrenko, V.A., Barbaree, J.M., and Chin, B.A., *Detection of Salmonella typhimurium in fat free milk using a phage immobilized magnetoelastic sensor.* Sensors and Actuators B: Chemical, 2007. **126**(2): p. 544-550.
57. Ruan, C., Zeng, K., Varghese, O.K., and Grimes, C.A., *Magnetoelastic immunosensors: amplified mass immunosorbent assay for detection of Escherichia coli O157:H7.* Anal Chem, 2003. **75**(23): p. 6494-6498.
58. Stoyanov, P.G. and Grimes, C.A., *A remote query magnetostrictive viscosity sensor.* Sensors and Actuators A: Physical, 2000. **80**(1): p. 8-14.
59. Puckett, L.G., Barrett, G., Kouzoudis, D., Grimes, C., and Bachas, L.G., *Monitoring blood coagulation with magnetoelastic sensors.* Biosensors and Bioelectronics, 2003. **18**(5–6): p. 675-681.
60. Green, S.R. and Gianchandani, Y.B., *Wireless Magnetoelastic Monitoring of Biliary Stents.* Microelectromechanical Systems, Journal of, 2009. **18**(1): p. 64-78.
61. Markova, L.V., Myshkin, N.K., Kong, H., and Han, H.G., *On-line acoustic viscometry in oil condition monitoring.* Tribology International, 2011. **44**(9): p. 963-970.
62. Kouzoudis, D. and Grimes, C.A., *The frequency response of magnetoelastic sensors to stress and atmospheric pressure.* Smart Materials and Structures, 2000. **9**(6).
63. Grimes, C.A., Stoyanov, P.G., Kouzoudis, D., and Ong, K.G., *Remote query pressure measurement using magnetoelastic sensors.* Review of Scientific Instruments, 1999. **70**(12): p. 4711-4714.
64. Grimes, C.A., Ong, K.G., Loiselle, K., Stoyanov, P.G., Kouzoudis, D., Liu, Y., Tong, C., and Tefiku, F., *Magnetoelastic sensors for remote query environmental monitoring.* Smart Materials and Structures, 1999. **8**(5): p. 639.
65. Ong, K.G., Mungle, C.S., and Grimes, C.A. *Control of temperature response for a magnetoelastic sensor with magnetic field tuning*. in *Magnetics Conference, 2003. INTERMAG 2003. IEEE International*. 2003.
66. Schmidt, S. and Grimes, C.A., *Characterization of nano-dimensional thin-film elastic moduli using magnetoelastic sensors.* Sensors and Actuators A: Physical, 2001. **94**(3): p. 7.
67. Li, S. and Cheng, Z.Y., *Nonuniform mass detection using magnetostrictive biosensors operating under multiple harmonic resonance modes.* Journal of Applied Physics, 2010. **107**(11): p. 114514-114514-6.

Chapter 2 Theory

Chapter Overview

The goal of this chapter is to present principles of magnetism and properties of magnetic materials related to the project. Additionally, this chapter includes the theory behind the developed magnetoharmonic and magnetoelastic (resonance) sensors. Of particular interest in these explanations is the presentation of a theoretical mechanism describing the operational principles of the magnetoelastic resonance sensor under a partial and large loading.

2.1 Metglas 2826MB

The described magnetoelastic sensor is based on a soft amorphous magnetoelastic material known as Metglas 2826MB. Metglas 2826MB ($Fe_{40}Ni_{38}Mo_4B_{18}$), purchased from Metglas Inc. 440 Allied Drive Conway, SC 29526, is commonly known as a metallic glass due to its disordered atomic-scale structure leading to a lack of a long order crystalline structure (just like other metallic oxide based glasses). The Metglas is fabricated by rapid heat quenching through melt spin extrusion technique [1], resulting in a metallic strip of tens of microns thick [2] with excellent soft magnetic properties such as high permeability, low coercivity and hysteresis [3]. The specific properties of Metglas 2826MB (see **Table 2.1** below) will be utilized later in this chapter for relevant calculations.

Properties of Metglas 2826MB	Values and unit [2]
Density (ρ)	7900 kg/m^3
Tensile strength	1-2 GPa
Young's modulus	100-110 GPa
Magnetostriction	12 ppm [2]
Poisson's ratio	0.33 [3]

Table 2.1 The properties of Metglas 2826MB.

2.1.1 Magnetic Properties: Soft vs. Hard

Metglas 2826MB exhibits excellent soft magnetic and magneto-mechanical properties. This refers to the fact that in the absence of an applied magnetic field the material reverts to a state of zero or near zero magnetization, demonstrated in the *BH* loops seen in **Figure 2.1 a-b**. The *BH* loop is a plot of the applied magnetic field (*H*) against the measured magnetic field flux density which is the magnetization response of the material (*M*) plus the applied *H* field. **Figure 2.1a** illustrates the *BH* loop of a hard magnetic such as a neodymium-iron-boron material [4]. As can be seen, the initial application of an applied field induces a magnetic response eventually reaching saturation at the saturation magnetization (H_s). When the applied field is reversed, major hysteresis occurs in the material response such that at zero applied field the material is still magnetized, referred to as the remanence (H_r). As the applied magnetic field becomes negative, the produced magnetization eventually reduces to zero, known as the coercive field (H_c). The *B* response continues to decrease to a negative H_s. Reversing the applied *H* field results in an increase back toward a positive H_s [5].

In addition to revealing the H_r and H_s of a material, the *BH* loop can also be used to identify a material's permeability from the slope of the *BH* loop [4]. As can be seen, a hard magnet exhibits a high H_r and H_s with a low permeability. Materials like this are referred to as hard magnets due to the fact that they can only be demagnetized through heat annealing, application of force or the reapplication of applied *H* fields at successively lower strengths, eventually causing the magnetization (*M*) to go to or near zero. **Figure 2.1b** illustrates the *BH* loop of a material such as Metglas 2826MB. As can be seen, H_r and H_c are nearly zero and, based on the slope of the *BH* loops, the expected permeability would also be quite high. The fact that these materials only magnetize in the presence of an applied *H* field and that they do not retain their magnetization unless a constant field is applied, i.e. H_r and H_s close to zero, make them excellent sensor transducers since any change in the observed material response at a given applied field can be directly correlated to the presence of a target of interest.

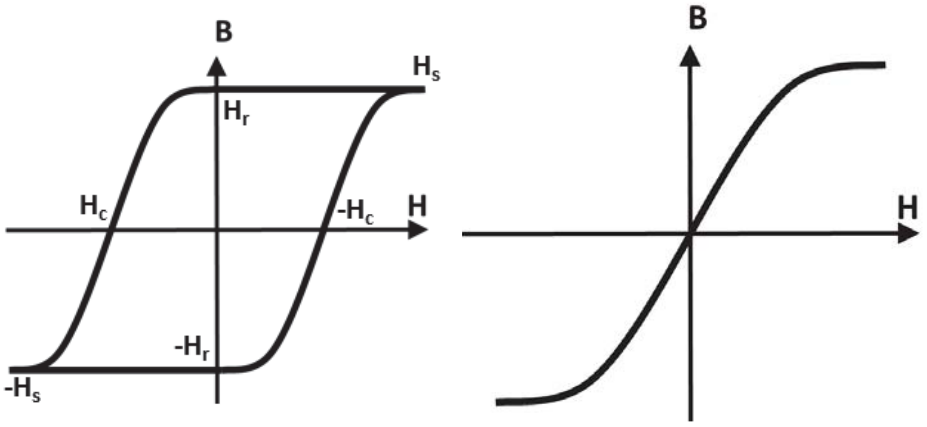

Figure 2.1 The BH loop of a (a) hard and (b) soft magnetic material.

2.1.2 Magnetic Properties: Magnetoelasticity

In addition to being a soft magnetic material, Metglas 2826MB also exhibits magnetoelastic properties. Magnetoelasticity is a term used to describe the coupling between elastic and magnetic energy in a given material. Specifically, a magnetoelastic material's elastic and magnetic properties are sensitive to an applied magnetic or mechanical stimulus, respectively. For instance, if a magnetic field H is applied to a material that is both magnetoelastic and magnetostrictive, a magnetostrictive strain is induced in the material according to [4]:

$$\varepsilon = \frac{\sigma}{E_M} + \frac{3\lambda_s}{2}\left(\frac{H^2}{H_k^2} - \frac{1}{3}\right) \qquad H<H_k \qquad (1)$$

where ε is the magnetostrictive strain, σ is an applied longitudinal stress, E_M is the Young's modulus at a constant field, λ_s is the magnetostriction ($\Delta L/L$ at magnetic saturation), H is the applied magnetic field and H_k is the anisotropy field.

This is of particular interest in the description of the theory behind the developed magnetoelastic resonance sensors. According to Eq. (1), the application of a magnetic field H can cause a strain in a magnetic material. This strain is observed as a change in the material's dimensions, referred to as magnetostriction, and in the material's Young's modulus, referred to as the ΔE effect. Specifically, the application of an applied magnetic field causes a forced rotation of domain regions, which are comprised of magnetic

dipoles, responsible for the overall magnetic response of the material. These forced rotations cause neighboring atomic elements to displace one another, resulting in a change in material dimensions, which also represents an induced internal strain that alters the material's Young's modulus [6].

While Eq. (1) represents a magnetic stimulus causing a change in mechanical properties, the opposite occurs as well. Of particular interest to this work is the impact of an external stress on the anisotropy (H_k) and susceptibility (χ) of Metglas according to [5]:

$$H_k = \frac{2K_u - 3\lambda_s\sigma}{M_s} \tag{2}$$

$$\chi = \frac{M_s^2}{2K_U - 3\lambda_s\sigma} \tag{3}$$

Eq. (3) describes what is known as the Villari Effect, which occurs when the permeability (μ) (related to susceptibility (χ) according to $\mu=\mu_0(1+\chi)$) of a magnetic material changes as a result of an applied mechanical stress. Specifically, from Eq. (3) it is apparent that an applied tensile stress will result in an increase in material permeability for positive magnetostriction materials while negative magnetostriction materials will experience a decrease in permeability. This results from a decrease in the anisotropy of the material, which alters the effect of a given magnetic field on the magnetization of the material, as can be seen in Eq. (3) [5]. This phenomenon has been used to develop force sensors, more thoroughly described below.

2.2 Higher Order Harmonics and Applied Stress

As previously described, the slope of the *BH* loop represents the permeability of the sensing material and an applied stress will alter that permeability according to the sign of the material's magnetostriction. In order to visualize this change, the non-linearity of the *BH* loop is taken advantage of. Specifically, if a constant AC field is applied to the material, the observed secondary magnetic flux will be in the form of a distorted sine wave. By utilizing a discrete fourier transform the frequency components of this response can be visualized according to [7]:

$$B(h) = C_0 + \sum_{n=1}^{\infty} 2|b_n| \cos\left(\frac{nh}{h_{ac}} + \phi_n\right) \quad (4)$$

where B is the magnetic flux, C_0 is a DC offset, b_n is the coefficient of the n^{th} order, h is the applied AC field and ϕ is the phase angle. What are referred to as the higher order harmonics can then be visualized by examining the peak amplitude of a particular frequency component, in this work the 400 Hz component captured from a 200Hz applied AC field, can be recorded. More precisely, the application of an additional DC biasing field will result in a change in the amplitude of the captured frequency component as the sensor response is moved along the BH loop according to [6]:

$$A_n = \frac{kLB_s\omega}{\pi}\left|e^{jn\pi H_{dc}/h_{ac}}\cos(\pi n) - \frac{h_{ac}}{\pi n H_k}\sin\left(\frac{\pi n H_k}{h_{ac}}\right)\right| \quad (5)$$

By plotting the peak amplitude against the applied DC biasing field, the higher order harmonics can be then be visualized (see **Figure 2.2**).

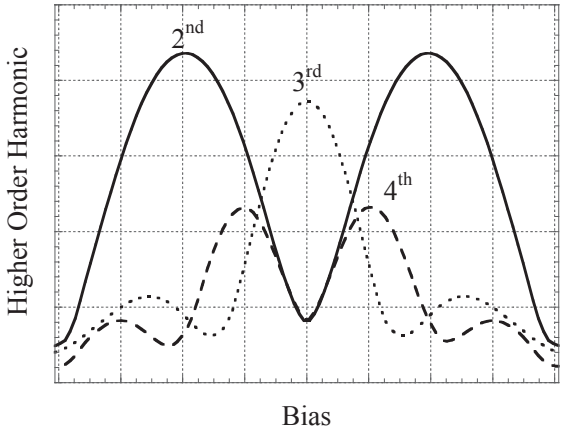

Figure 2.2 Higher-order field components of a magnetically soft material.

2.2.1 Operational Principle of Magneto-harmonic Sensors

With the higher order harmonics visualized, the pressure sensitivity of the material can be explored. Specifically, a change in the amplitude of the higher order

harmonics occurs with applied loading. This can be explained by the magnetic permeability (χ), which is the ratio of the saturation magnetization (M_s) to the anisotropy field (H_k) expressed as [7]:

$$\mu \approx B_s / H_k \tag{6}$$

The anisotropy field of a magnetic material can be related to the tensile stress along the magnetization direction as [9]:

$$H_k = H_{k0} - 3\lambda_s \sigma_x / M_s \tag{7}$$

where H_{k0} is the anisotropy field at zero stress, λ_s is the saturation magnetostriction of the material and σ_x is the tensile stress along the magnetization direction, which is also along the length of the sensor.

Equation (8) describes the change in anisotropy field due to the tensile stress along the sensor's length. However, for applications where applied loading is primarily normal to the surface of the sensing strip, the transverse stress on the sensor surface can be related to the tensile stress along the sensor length (y-direction) using the Poisson's ratio υ as:

$$\sigma_x = 2\,\sigma_y / \upsilon \tag{8}$$

Force and area are related to the applied stress σ_y according to:

$$\sigma_y = F_y / lw \tag{9}$$

where F_y is the applied force along the y-axis, l is the length and w is the width. If Eqs. (8) and (9) are substituted into Eq. (7):

$$H_k = H_{k0} - \frac{6\lambda_s F_y}{M_s \upsilon \cdot l \cdot w} \tag{10}$$

Eq. (6) illustrates that the change in permeability is inversely related to the anisotropy field and from Eq. (7) it can be determined that the anisotropy field changes directly as a function of applied stress. Eqs. (8) and (9) show that not only is the stress of interest in the y-direction, but also that the stress, and thus the change in anisotropy field,

is directly related to the change in applied force. Applying this to Eq. (6) it is then apparent that the application of force will result in an increase in the magnetic permeability as a result of a decrease in H_k.

This will result in an increase in overall magnetic flux density and thus an increase in the observed higher order harmonic according to Eq.(13) and Eq.(14) [7]:

$$A_n = \frac{LB_S\omega}{\pi^2}\left|e^{jn\pi H_{dc}}cos(\pi n) - \kappa sin\left(\frac{1}{\kappa}\right)\right| \tag{13}$$

$$\kappa = \frac{h_{ac}B_s}{n\pi\left(B_sH_k\text{-}3\lambda_s\sigma\right)} \tag{14}$$

where A_n the n^{th} order harmonic amplitude, H_{dc} is the applied DC magnetic field, L is the coupling between the sensor and the coil, B is the magnetic flux density, ω is the radian frequency, H_k is the anisotropy field, λ_s is the magnetostriction and σ is the applied stress [10].

2.3 Magnetostriction and Load Monitoring

Many magnetic materials are *magnetostrictive*, which means they experience a change in dimensions when exposed to an applied magnetic field. As illustrated in **Figure 2.3**, magnetostriction arises as a result of the physical displacement of neighboring dipoles as the applied magnetic field causes the various domain regions, which are comprised of dipoles, in a material to orient towards the applied field,.

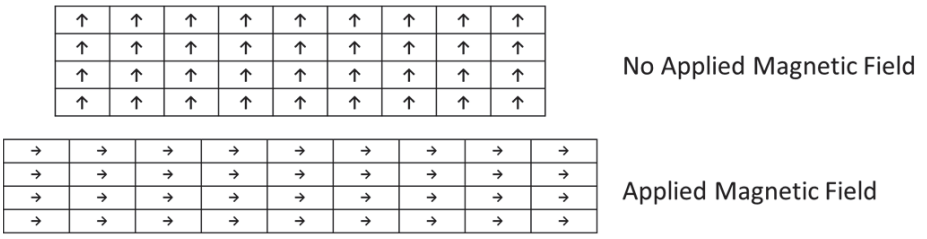

Figure 2.3 In the presence of an applied magnetic field the domain regions of a magnetic material orient in the field direction, resulting in an elongation in the material.

This property can be used, along with an AC excitation field, to induce longitudinal vibrations in a magnetostrictive material as a result of discrete displacements in the material which behave according to [11]:

$$u(x,t)=u_0 cos\left(\frac{n\pi}{L}x\right)e^{j2\pi f_n t} \quad (15)$$

where u is the displacement of a material at position x and time t, u_0 is the maximum displacement, n is the harmonic number and f_n is the resonance frequency of the nth harmonic. If the AC excitation field is swept over a range of values, the magnitude of the material displacement will eventually reach a maximum referred to as the mechanical resonance. The frequency at which this resonance occurs is described according to [10]:

$$f_n=\frac{1}{2L}\sqrt{\frac{E_H}{\rho_s(1-\sigma)}} \quad (16)$$

where f_n is the nth resonant frequency, n is the harmonic, L is the strip length, E_H is the sensor Young's modulus at a constant field H, ρ_s is the sensor density and σ is the Poisson's ratio [10]. Additionally, the acoustic velocity of the elastic wave at resonance behaves according to [10]:

$$v=\frac{2f_n L}{n} \quad (17)$$

where v is the acoustic velocity, f_n is the resonance frequency of the n^{th} harmonic mode, L is the sensor length and n is the harmonic mode. These vibrations, as a result of the rotation of magnetic dipoles, correspond to an induced secondary magnetic flux. Since the mechanical resonance occurs as a result of a peak in the number of commonly oriented domains, a peak in the secondary magnetic flux also occurs at resonance, as illustrated in **Figure 2.4** which shows the first, second and third magnetic resonant peaks of a 71 mm × 4 mm strip. As can be seen, a sharp increase occurs at the resonant peaks followed by a sharp decrease in the amplitude of the captured magnetic response. In the following section the manner in which this resonance frequency is utilized to monitor applied loading is detailed.

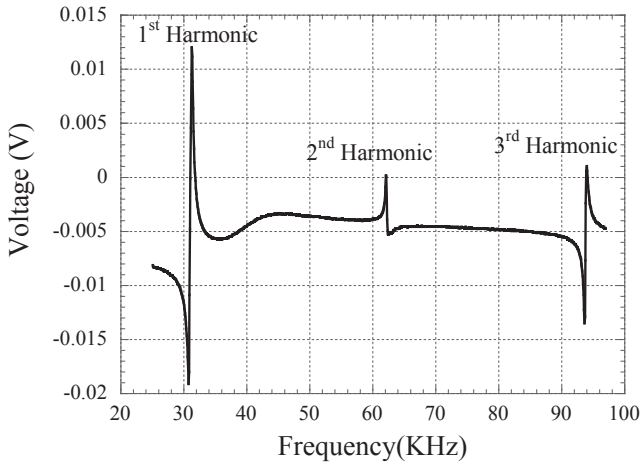

Figure 2.4 The first three harmonic resonant peaks of a 71 mm × 4 mm sensing strip were visualized by applying an AC frequency sweep from 0 kHz to 100 kHZ.

2.3.1 Assumption and Justification

The presented theory assumes that 1) each discrete location on a strip is effectively a longitudinal actuator, 2) the magnitude of the friction force from loading is larger than the elastic forces resulting from magnetostrictive deformation at any given discrete location and 3) since the friction force is larger than the produced deformation forces, any discrete point of contact between the applicator and sensing element pins the region. In order to validate the second and third assumptions, it is necessary to compare the theoretical elastic forces from magnetostriction and the frictional forces from applied loading. The forces produced by magnetostriction can be determined using [5]:

$$F_{elasitc}=A\sigma \tag{18}$$

where $F_{elastic}$ is the elastic force, A is the cross sectional area and σ is the total applied stress. In order to calculate $F_{elastic}$ it is necessary to determine the strain in the region of interest such that σ can be calculated using [5]:

$$\sigma=E\varepsilon \tag{19}$$

where E is the elastic modulus and ε is the strain in the region of interest. It is well known that strain is simply the ratio of the change a dimension and the original dimension. In order to determine the elastic force at any given point on the strip then, ε must be

determined. To accomplish this, the change in length at a point along the strip can be calculated according to [11]:

$$u(x,t)=u_0 cos\left(\frac{n\pi}{L}x\right)e^{j2\pi f_n t} \tag{20}$$

where u_0 is the maximum change in length, x is the position along the length of the sensing element, n is the harmonic resonance mode, L is the length of the sensing element and f_n is the resonance frequency of the n^{th} harmonic resonance mode and t is time. While n, L, x and t can either be chosen or are known, the constant u_0 is calculated according to [4]:

$$\varepsilon_\lambda=\frac{u_0}{L} \tag{21}$$

where ε_λ is the magnetostrictive strain, which is 12 ppm for Metglas 2826MB [2], and f_n is calculated using [10]:

$$f_n=\frac{2222}{L*1000} \tag{22}$$

By then plugging Eq. (21) and Eq. (22) into Eq. (20) the equation for displacement becomes:

$$u(x,t)=(\varepsilon_\lambda L)cos\left(\frac{n\pi}{L}x\right)e^{j2\pi\left(\frac{2222}{L*1000}\right)t} \tag{23}$$

The strain is the determined according to:

$$\varepsilon=\frac{u(x,t)}{L} \tag{24}$$

Using the known elastic modulus of 100 GPa and the strain calculated from Eq. (23), the total stress in a given area can be determined according to Eq. (19), which allows for the calculation of the total force in a given area by plugging the stress into Eq. (18). This process was utilized with a theoretical 30.5 mm × 4 mm Metglas 2826MB strip in contact with a 1.0 mm × 5.0 mm applicator. The calculated displacement at t = 0 for the 1st harmonic (n = 1) of this sensor in the region in contact with the applicator, occurring at the boundaries, is then found to be 0.0701 N.

Having determined the theoretical magnetostrictive force, the frictional force must be determined. Generally speaking the coefficient of friction between metals and plastics ranges between 0.2 and 0.4 [12]. Using this range, even at forces as low as 0.5 N the load in the region of the applicator is 0.1 N and at the high end is 0.2 N. This would result in a

force that can overcome the maximum theoretical elastic forces produced by magnetostriction, resulting in the pinning of the contact regions.

2.3.2 High Load Magnetoelastic Resonance Sensor Theory

The validation of the proposed assumptions provides the foundation for the presented theory used to explain how the developed sensor monitors an applied loading as an increase in the observed resonance frequency. This phenomenon is explained by examining the contact mechanics between the load applicator and the vibrating strip. Specifically, on a macro scale, two surfaces in contact under an applied loading can appear to be in complete contact with one another, almost as if they are adhered together. However, typically materials have some level of surface roughness which results in contact occurring primarily at the peaks of these rough surfaces, referred to as asperity regions (see illustration in **Figure 2.5**) [13]. As an applied pinching force increases, the materials deform in relation to their respective elasticities, resulting in further contact as the gaps between the surfaces decreases. Eventually the size and number of contact points can no longer increase unless plastic deformation occurs in one or both materials [13]. In the case of a vibrating magnetoelastic sensor, these contact regions represent areas of pinning wherein the magnetoelastic sensor can no longer vibrate. In effect, this results in a decrease in the overall length of the sensor, which causes an increase in resonance frequency that can be related to the applied loading [10].

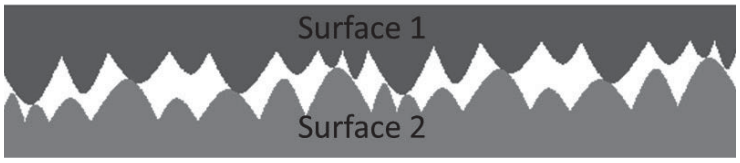

Figure 2.5 The actual contact between two surfaces depends upon the roughness of each surface and the resulting contact points referred to as asperity regions.

References

1. *All Frequently Asked Questions*. 2003-2014; Available from: http://www.metglas.com/faq/.
2. *Metglas® 2826MB Magnetic Alloy*. 2003-2014; Available from:

http://www.metglas.com/products/magnetic_materials/2826mb.asp.
3. Ramasamy, M. and Prorok, B.C., *Resonance Behavior of Magnetostrictive Sensor in Biological Agent Detection*, in *Experimental and Applied Mechanics, Volume 6*, T. Proulx, Editor. 2011, Springer New York. p. 875-876.
4. Keat, G.O. and Craig, A.G., *Magnetostrictive Nanomaterials for Sensors.* ChemInform, 2004. **35**(37).
5. Elkins, K.E., *Fabrication of Iron-platinum Ferromagnetic Nanoparticles*. 2008: ProQues. 153.
6. Cullity, B.D. and Graham, C.D., *Introduction to Magnetic Materials*. 2009: Wiley.
7. Ong, K.G. and Grimes, C.A., *Tracking the harmonic response of magnetically-soft sensors for wireless temperature, stress, and corrosive monitoring.* Sens Actuators A Phys, 2002. **101**(1-2): p. 49-61.
8. Livingston, J.D., *Magnetomechanical properties of amorphous metals.* physica status solidi (a), 1982. **70**(2): p. 591-596.
9. Kouzoudis, D. and Grimes, C.A., *The frequency response of magnetoelastic sensors to stress and atmospheric pressure.* Smart Materials and Structures, 2000. **9**(6): p. 885.
10. Grimes, C.A., Roy, S.C., Rani, S., and Cai, Q., *Theory, instrumentation and applications of magnetoelastic resonance sensors: a review.* Sensors (Basel). 2011. **11**(3): p. 2809-44.
11. Suiqiong, L. and Cheng, Z.Y., *Nonuniform mass detection using magnetostrictive biosensors operating under multiple harmonic resonance modes.* Journal of Applied Physics, 2010. **107**(11): p. 114514-114514-6.
12. Zaretsky, H.H., Steven R. Herbert, and Alex Moroz., *Medical Aspects of Disability: A Handbook for the Rehabilitation Professional*. 4 ed. 2010, New York, NY: Springer Publishing Company. 784.
13. Persson, B.N.J., *Contact mechanics for randomly rough surfaces.* Surface Science Reports, 2006. **61**(4): p. 201-227.

Chapter 3 A Wireless, Passive Load Cell based on Magnetoelastic Resonance

Brandon D. Pereles, Thomas Dienhart, Thadeus Sansom, Kyle Johnston, and Keat Ghee Ong*

Department of Biomedical Engineering, Michigan Technological University, Houghton, MI 49931, USA

Abstract

A wireless, battery-less load cell was fabricated based on the resonant frequency shift of a vibrating magnetoelastic strip when exposed to an AC magnetic field. Since the vibration of the magnetoelastic strip generated a secondary field, the resonance was remotely detected with a coil. When a load was applied to a small area on the surface of the magnetoelastic strip via a circular rod applicator, the resonant frequency and amplitude decreased due to the damping on its vibration. The force sensitivity of the load cell was controlled by changing the size of the force applicator and placing the applicator at different locations on the strip's surface. Experimental results showed the force sensitivity increased with a larger applicator placing near the edge of the strip. The novelty of this load cell is not only its wireless passive nature, but also the controllability of the force sensitivity.

Keywords: Magnetoelastic; resonance; magnetic; load cell; force

3.1 Introduction[1]

Most force transducers today are based on, but not limited to, resistive, capacitive, and/or optical sensing technologies. Resistive based sensing platforms monitor force through devices that change electrical resistance in response to an applied load. For instance, piezoresistive sensors primarily consist of materials whose electrical resistance changes with force. One such device, the Tekscan Flexiforce, utilizes semi-conductive ink sandwiched between conductive polyester sheets as the force sensitive element. An applied load alters the resistance of the ink, thus changing the overall resistance measured

[1]"The material in this chapter was previously published in *Smart Materials and Structures*."

on the active conducting sheets [1]. Capacitive based sensing platforms take advantage of the changes in observed sensor capacitance as a means to monitor force application. One such system was developed for use with endoscopic tools and is comprised of an array of capacitive elements with a total size of less than 1 mm^2 [2]. Similar to resistive and capacitive technologies, optical sensors function as a result of an observed change in the intensity, frequency, and spectrum of light due to an applied force. For instance, the LED Microshift, consisting of a glass cube with a cavity protected by a silicon diaphragm, was deployed for blood pressure monitoring in catheters based on the change in light spectrum [3]. These force monitoring devices, while highly useful and well established, often lack wireless and passive sensing capability, which not only limits long term use but also prevents application as embedded sensors.

Wireless, passive versions of force sensors have been developed based on electromagnetic coupling. For example, sensors based on radio frequency identification devices (RFID), which consist of strain gauges incorporated onto the RFID tags for electromagnetically coupling to a remote detector, were reported for use in structural health monitoring [4]. Magnetic materials were also used for wireless force monitoring. For instance, a sensor was reported for wireless force mapping and consisted of three strips of a soft amorphous magnetoelastic material, Metglas 2826MB, adhered to a polycarbonate block with appropriate load applicators placed on top of the strips [5]. Under excitation of an AC magnetic field, the magnetoelastic material generated magnetic field at higher frequencies (higher order harmonic fields) capable of being remotely monitored with a detection coil. Applied force resulted in an increase in the observed amplitude of the higher order harmonic fields due to an increase in the sensor's magnetic permeability. The force profile could then be determined by processing the higher-order magnetic field responses of all strips [5].

Another sensor design based on the interference between a magnetically soft material and a permanent magnet was also developed for stress and force monitoring. The sensor design consisted of a magnetically soft material placed adjacent to a permanent magnet. Force or pressure altered the separation distance between these two magnetic elements, changing the magnetization response of the magnetically soft material. The

change was reflected in the shift in higher-order harmonic field pattern [6]. This sensor was applied to measure mechanical force loading [7] as well as atmospheric [6] and liquid pressures [8].

Magnetoelastic resonance sensors are another type of wireless sensors that have been demonstrated for force or stress monitoring. When subjected to an AC magnetic excitation field, these sensors experience a mechanical resonance as a result of their magnetoelasticity. The experienced resonance produces a secondary magnetic flux that can be detected with an external pickup coil [9]. The application of a force dampens the vibration, reducing the resonant frequency and amplitude. This mode of sensing has been deployed for monitoring the Young's modulus and mass of a coating, and, with a mass-changing chemically sensitive coating, the concentration of various chemicals and biological agents such as glucose or E. coli [9, 10]. While the reported sensors are simple, they focused on uniform force loadings on the sensor surfaces, and there is no systematic way to control the stress sensitivity.

Presented here is a force sensor, or a load cell, based on the magnetoelastic resonance using non uniform force distribution for controlling stress sensitivity. The load cell consisted of a strip of magnetoelastic material and an associated permanent magnet to produce the biasing field for optimal magnetoelastic response [11]. Both elements were placed inside a rigid structure featuring an applicator that transferred force to the strip's surface. Since the strain of a magnetoelastic strip is zero at the center of the strip and maximum at the ends of its length, the effect of the force loading will be different depending on the loading location. This phenomenon was exploited for creating a wireless, passive load cell with controlled stress sensitivity.

3.2 Experiments

3.2.1 Sensor Fabrication

Two load cells were fabricated and tested. The first load cell consisted of a series of holes through which the force applicator can pass (see **Figure 3.1a**). Load Cell A, consisting of an array of loading positions for the force applicator, was used to characterize response of the magnetoelastic strip under loading at different positions.

Load Cell B, with only one force loading position, was fabricated to demonstrate the application of this technology for wireless force measurement (see **Figure 3.1b**). Load Cell A was milled from a piece of polycarbonate using a CNC Micro Milling Machine and measured 54.5 mm × 32.2 mm × 12.7 mm. The holes in the top piece, measuring 4.75 mm in diameter, were positioned at the center of the width of the strip and were spaced along the length of the strip. Force was applied through applicators consisting of polycarbonate shafts with an attached metal rod for applying weight during testing. Three force applicators were fabricated and used to investigate the effect of loading area on the load cell sensitivity and dynamic range. The applicators consisted of a polycarbonate shaft with a rod affixed to the top for applying weights. The area of force application was controlled by adhering rubber tips to the head of the applicator. Three such applicators were fabricated with circular rubber tips having diameters of 0.7 mm, 1.6 mm, and 2.48 mm respectively.

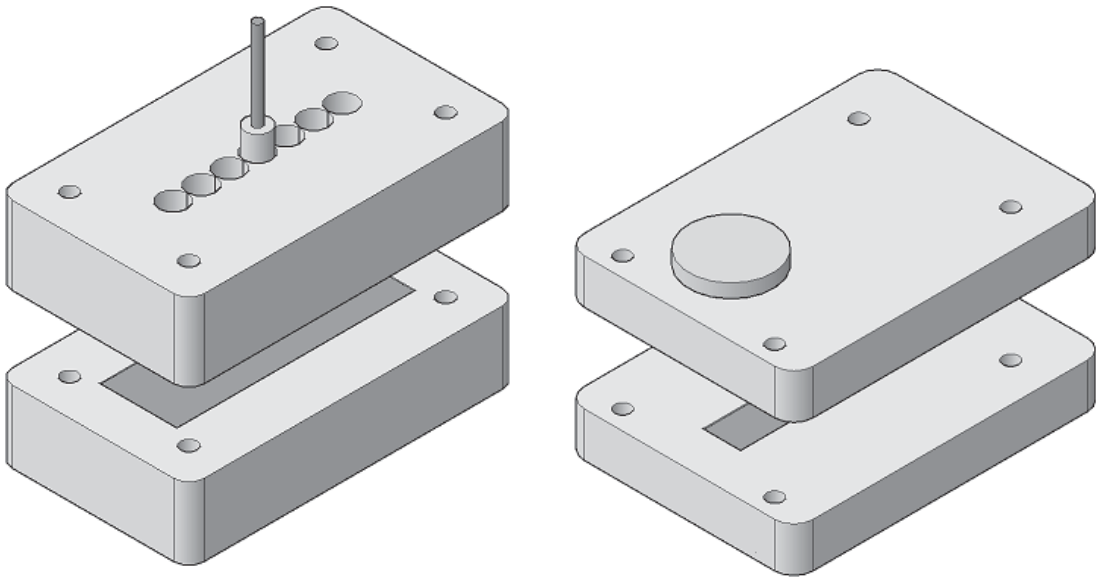

Figure 3.1 (a) Load Cell A was designed to allow for loading at multiple positions. (b) Load Cell B consisted of a single loading position, but was significantly smaller than Load Cell A.

Similarly, Load cell B was milled from a block of polycarbonate using a CNC Micro Milling Machine. The top and bottom pieces measured 35 mm × 25 mm × 5.85 mm and were held together by nuts and bolts at the corners. An applicator head consisting of two pieces of polycarbonate rod and a small metal tip was also fashioned.

The top of the applicator measured 11.15 mm in diameter with a height of 4.2 mm, the shaft measured 4.7 mm in diameter with a height of 5.9 mm, and the metal tip measured 1.5 mm in length extending out of the shaft. A hole was milled for the applicator head and a guide rod was used to prevent the applicator from rotating and minimized tilting during testing.

The bottom pieces of both load cells consisted of two wells, one for placing the magnetoelastic strip and the other for the permanent magnetic strip. The well dimensions for the magnetoelastic strip and the permanent magnetic strip were 38.65 mm × 12.52 mm × 0.5 mm and 14.63 mm × 4.0 mm × 0.5 mm for Load Cell A and 30 mm × 8 mm × 0.5 mm and 15 mm × 6.5 mm × 0.5 mm for Load Cell B, respectively. The magnetoelastic strips were sheared from a ribbon of 26 μm thick Metglas 2826 MB ribbon ($Fe_{40}Ni_{38}Mo_4B_{18}$) purchased from Metglas Inc, Conway, SC, USA and the permanent magnetic strips were cut from 0.05 mm thick ribbon of Arnokrome™ 3 (Arnold Magnetic Technologies). It is worth noting that the permanent magnetic strips can be replaced by an external DC magnetic field.

3.2.2 Experimental Setup and Procedure

Figure 3.2 illustrates the experimental setup. The load cell was attached to the test platform with double sided adhesive tape and was positioned in front of the excitation and detection coils. The detection coil connected to a Stanford Research Systems SR810 Lock in Amplifier which captured the sensor resonance and sent it to a PC for further analysis. A customized Visual Basic program was used to automate the measurement process. The excitation coil consisted of a 50 turn 18-gauge circular coil connected to a Fluke 271 10 MHz AC function generator responsible for producing the necessary frequency sweep. An audio amplifier (Tapco J1400) was used to amplify the excitation signal.

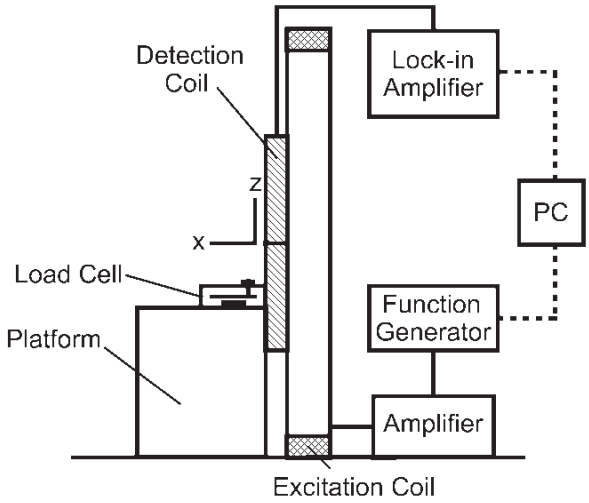

Figure 3.2 The full experimental setup illustrating the AC excitation coil, detection coil, function generator, amplifier, and magnetoelastic load cell.

During all experiments, loads were applied to the applicator heads in 0.049 N intervals from 0 to 0.311 N for the multi-position load cell and 0 to 0.203 N for the smaller load cell (the applicator heads themselves weighed 0.017 N and 0.007 N, respectively, which was not considered in the load calculation). Testing was then repeated from maximum load to zero in order to test sensor repeatability and hysteresis. Before running experiments, the sensors were removed from in front of the detection coil and a background sweep was performed to remove ambient noise and the resonance of the coil from the obtained results. Following sufficient testing with both sensors, Load Cell B was further characterized through hysteresis and movement (along the *x*, *y*, and z axis) testing.

3.3 Results and Discussion

3.3.1 Effect of Loading Position and Applicator Head Size

As shown in **Figure 3.3**, force loading on the magnetoelastic sensor through an applicator at a portion of the sensor surface increased the resonant frequency. As expected, the resonant amplitude decreased with increasing loading due to damping on the vibration.

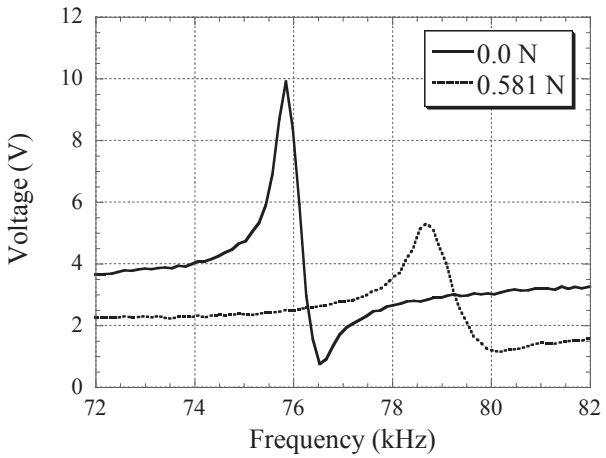

Figure 3.3 Force applied to the magnetoelastic strip resulting in an increase in the peak resonant frequency and a decrease in the resonant amplitude.

Applying loads along the length of the sensor demonstrated an increase in sensitivity as the position of force application moved away from the center of the strip. This can be explained by examining the equation of motion of the sensor, which is described as [12]:

$$\rho \frac{\sigma^2 u}{\sigma t^2} = \frac{E}{1-\sigma^2} \frac{u^2}{\sigma y^2} \tag{1}$$

where t is time, y is the length direction, u is the displacement along the length direction, ρ is the density of the sensor material, E is the Young's modulus of the material, and σ is the Poisson's ratio. For a free standing sensor with no rigid restraints at the ends of its length, the displacement u will be at the largest at the ends of the length and smallest at the center. Assuming the center of the sensor is at $y = 0$, a solution for Eq. (1) that fulfills the boundary conditions of a free standing sensor is:

$$u = 2Be^{-j\omega_n t} \sin\left(\frac{n\pi y}{L}\right) \tag{2}$$

where B is a complex number, n is the resonance mode, ω_n is the longitudinal resonant radian frequencies of the sensor, and L is the sensor's length. Eq. (2) indicates the vibration amplitude of the sensor, at the fundamental resonant frequency, should be zero at the center and largest at the ends. The vibration amplitudes have a large effect on the stress sensitivity of the sensor, as demonstrated by the results in **Figure 3.4**. As expected

from **Figure 3.4**, the largest frequency shift occurred in Position 1 (farthest from the center of the strip); whereas the smallest shift occurred in Position 4 (at the center of the strip).

To quantify the effect of altering the loading position along the sensor's length on sensitivity and range, the curves in **Figure 3.4** were fitted with a decaying exponential in the form of:

$$\Delta f = A\left(1 - e^{-kF}\right) \tag{3}$$

where Δf is the resonant frequency shift, F is the applied load, and A and k are coefficients describing the curve. The coefficients A and k were obtained from curve fitting the collected data. **Figure 3.5** shows that A and k increased with distance from the center, indicating a proportional relationship with the sensor's sensitivity and dynamic range.

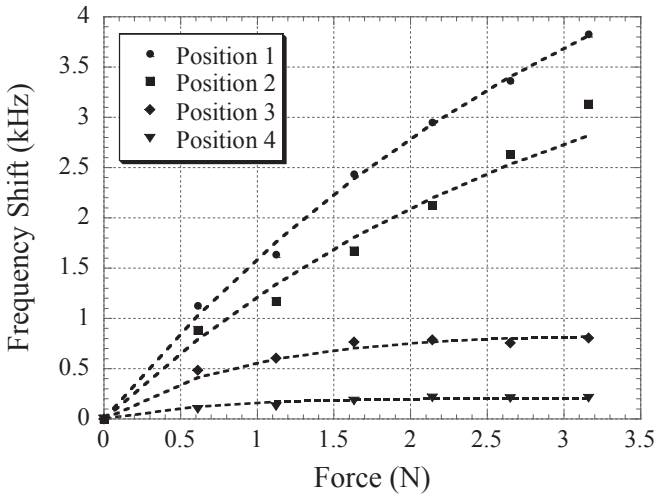

Figure 3.4 The results of multi-position load testing show the sensitivity and dynamic range of the sensor decreased when the load position moved away from the center of the sensor.

The size of the applicator head also had a distinct effect on sensor range and sensitivity (see **Figure 3.6**). During experimental testing it was observed that smaller heads were less sensitive to overall change in force applicator, but also demonstrated the capacity for a larger overall sensing range. **Figure 3.7** plots the coefficients of the

equation for lines in Figure 6 against the applicator head size, demonstrating the capacity to alter sensor sensitivity and range by altering the surface area of the force applicator.

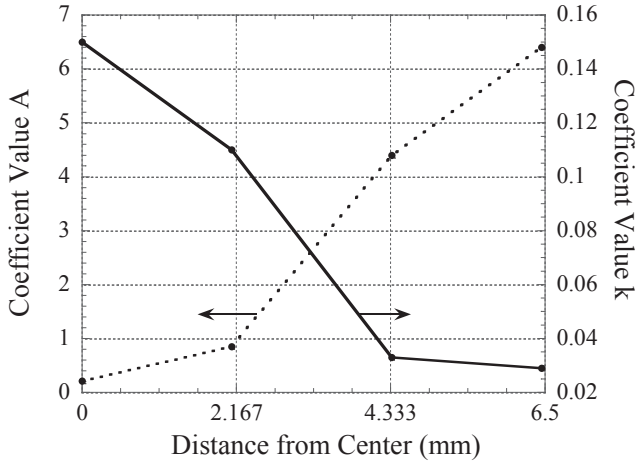

Figure 3.5 The coefficients of the equation describing the sensor behavior demonstrate an inverse relationship (for A) and proportional relation (for k) as the loading moved away from the center of the strip.

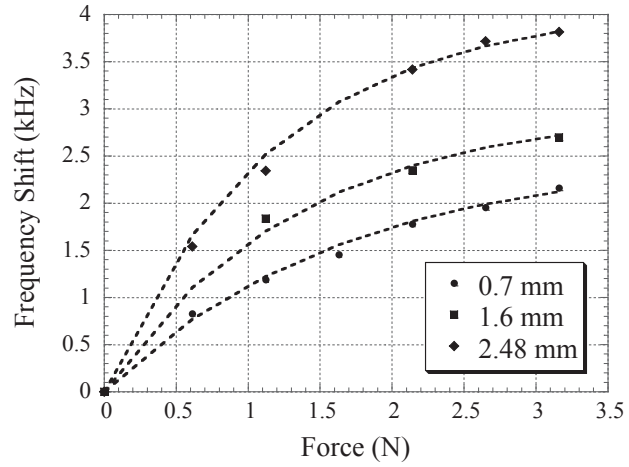

Figure 3.6 The results of loading with different applicator heads demonstrate a direct relationship linking the sensor's sensitivity to the size of the applicator head

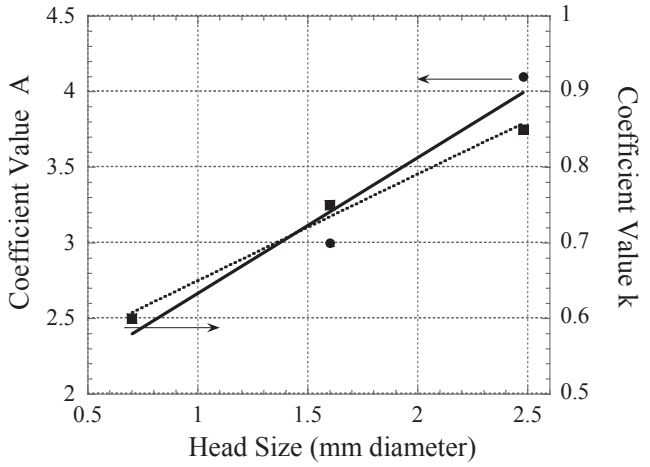

Figure 3.7 The coefficients of the equation describing the sensor behavior demonstrate a direct relationship between the coefficients and the size of the applicator head.

3.3.2 Effect of Load Cell Location from the Excitation/Detection Coils

In addition to force monitoring, the sensor response under zero loading conditions, when incrementally moved on the *x*, *y*, and *z* axis was also observed (see **Figure 3.8**). The *x*-axis testing demonstrated a gradual decrease with increasing distance from the coil, which is to be expected as the field experienced and captured by the detection coil decreased as the magnetoelastic strip was moved away from the coil (see **Figure 3.8a**). Along the *y*-axis, the measured amplitude increased as the sensor moved closer to the center of the detection coil and then decreased as that center passed (see **Figure 3.8b**). This result is explained by the fact that the peak signal amplitude will be experienced when the sensor is at the center of the coil. A similar result was seen along the *z*-axis (see **Figure 3.8c**).

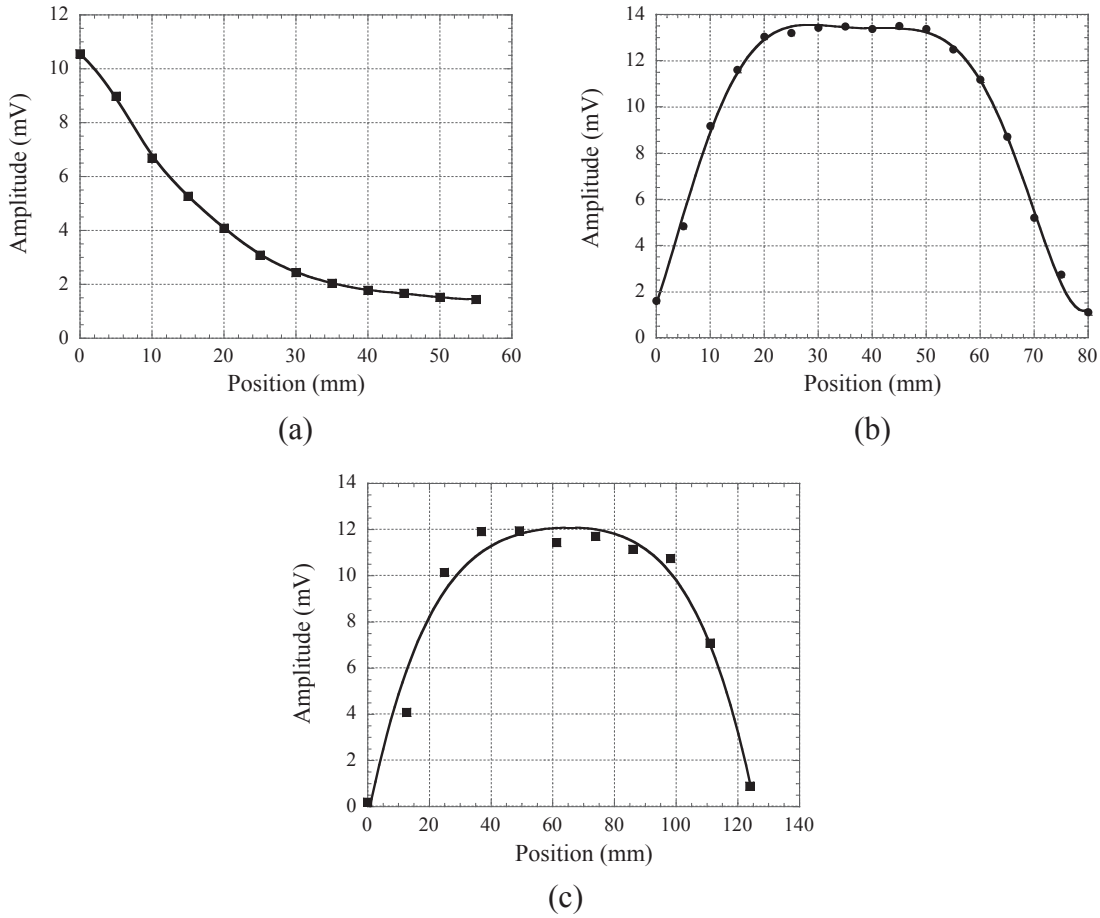

Figure 3.8 The effects on the measured sensor amplitude while the sensor was moved along the (a) x, (b) y, and (c) z axis.

3.3.3 Performance of the Magnetoelastic Load Cell

Following testing with Load Cell A, Load Cell B was fabricated and tested (see **Figure 3.9**). As expected from the previous testing, the sensor was highly sensitive to load application and was capable of detecting loads as low as 0.049 N. Additionally, the sensor saturated at 0.2 N, which was earlier than Load Cell A at 0.311 N. This is to be expected since the applicator head was located closer to the front of the strip. Moreover, the sensor's overall size was decreased, resulting in a decreased overall sensor range and sensitivity regardless of the position of loading and/or the size of the applicator head. The sensor also demonstrated a decaying exponential response, and repeatability testing (see **Figure 3.10**) produced a consistent response over the course of 10 loading cycles.

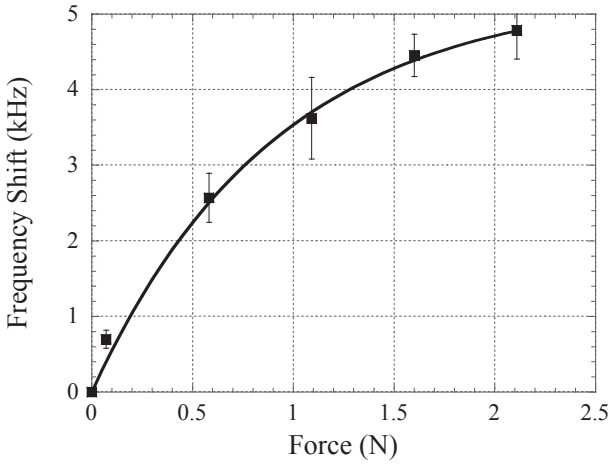

Figure 3.9 The results of testing Load Cell B demonstrate a decaying exponential behavior with high sensitivity but low range.

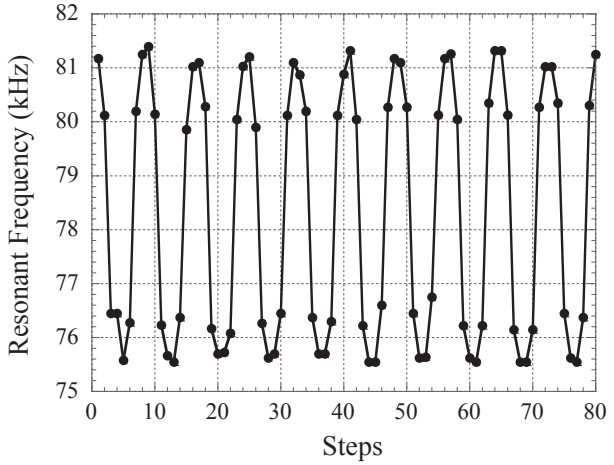

Figure 3.10 Hysteresis testing with Load Cell B demonstrates consistent results over multiple force loading cycles.

3.4 Conclusion

The fabrication and testing of a wireless passive load cell based on the magnetoelastic resonance sensor has been presented. The performance of this load cell was first evaluated by applying loads at multiple locations along the length of the strip and with applicator heads of varying sizes. Testing occurred from 0 to 0.311 N and demonstrated that the largest range and sensitivity was experienced at the edges of the

strip, along its length, while the center of the strip exhibited small change in resonance as a result of force application. Additionally, larger force applicator heads resulted in more sensitive sensing response but significantly decreased range. A smaller load cell with a pin point applicator head situated near the front of the strip was also fabricated. The load cell was tested from 0 to 0.2 N at 0.049 N intervals with acceptable repeatability between tests.

The presented sensor represents, given further development, a new method for wireless passive long term force monitoring with the capacity to be modified for varying ranges and sensitivities based on the location of load application, the size of the applicator head, and the overall size of the magnetoelastic strips. Future works include further miniaturization of the sensor and optimization of the excitation and detection system to provide for a more portable and size appropriate detection system.

Acknowledgments

This work was supported in part by the National Institute of Biomedical Imaging and Bioengineering under Grant R15EB008883-01A1. The content is solely the responsibility of the authors and does not necessarily represent the official views of the National Institute of Biomedical Imaging and Bioengineering or the National Institutes of Health. The authors would also like to acknowledge the Nation Defense Science and Engineering Grant for support of a graduate student fellow to contribute to this project. The authors would like to thank Andrew DeRouin and Ee Lim Tan for their technical support in this project.

References

1. Lebosse C, Renaud P, Bayle B, de Mathelin M. *Modeling and Evaluation of Low-Cost Force Sensors*. IEEE Transactions on Robotics. 2011; **27**(4): p. 815–822.
2. Puangmali P, Althoefer K, Seneviratne LD, Murphy D, Dasgupta P. *State-of-the-art in force andtactile sensing for minimally invasive surgery*. IEEE Sensors Journal. 2008; **8**(3–4): p. 371–381.
3. Polygerinos P, Zbyszewski D, Schaeffter T, Razavi R, Seneviratne LD, Althoefer K. *MRI Compatible Fiber-Optic Force Sensors for Catheterization Procedures*. IEEE Sensors Journal. 2010; **10**(10): p. 1598–1608.

4. Ikemoto, Y.; Suzuki, S.; Okamoto, H.; Murakami, H.; Xin, Lin; Itoh, H.; Asama, H. *Force sensorsystem for structural health monitoring using passive RFID tags for structural health monitoring*. 2008 IEEE Interdisciplinary Conference on Portable Info Devices (PORTABLE) – Polytronic 2008; IEEE Conference on Polymers and Adhesives in Microelectronics and Photonics; 2008. p. 1-6.
5. Pereles, B.D., DeRouin, A.J., Dienhart, T.A., Tan, E.L and Ong, K.G., *A Wireless, Magnetoelastic-based Sensor Array for Force Monitoring on a Hard Surface*, Sensor Letters. 2012, **10**(3-4): p. 806-813.
6. Pereles BD, S R, Tan EL, Ong KG. A Remote Query Pressure Sensor Based on Magnetic Higher Order Harmonic Fields. IEEE Sensors Journal. 2008; 8(11):1824–1829.
7. Ee Lim T, Pereles BD, Ranyuan Shao, Ong J, Keat Ghee Ong. *A wireless, passive strain sensor based on the harmonic response of magnetically soft materials*. Smart Materials and Structures. 2008; **17**(2): p. 025015.
8. Ee Lim T, Pereles BD, Ong KG. *A Wireless Embedded Sensor Based on Magnetic Higher Order Harmonic Fields*: Application to Liquid Pressure Monitoring. IEEE Sensors Journal. 2010; **10**(6): p. 1085–1090. [PubMed: 20514363]
9. Grimes CA, Roy SC, Rani SJ, Cai QY. *Theory, Instrumentation and Applications of Magnetoelastic Resonance Sensors: A Review*. Sensors. 2011; **11**(3): p. 2809–2844. [PubMed: 22163768]
10. Ong KG, Zeng K, Yang X, Shankar K, Ruan C, Grimes CA. *Quantification of multiple bioagents with wireless, remote-query magnetoelastic microsensors*. IEEE Sensors Journal. 2006; **6**(3): p. 514– 523.
11. Ong KG, Mungle CS, Grimes CA. *Control of a magnetoelastic sensor temperature response by magnetic field tuning*. IEEE Trans. Magnetics. 2003; **39**(5): p. 3319–3321.
12. Grimes, C. A., Ong, K. G., Loiselle, K., Stoyanov, P. G., Kouzoudis, D., Liu, Y., Tong, C. and Tefiku, F. *Magnetoelastic sensors for remote query environmental monitoring*. Smart Materials & Structures. 1999, **8**(5): p. 639-646.

Chapter 4 Partially Loaded Magnetoelastic Sensors with Customizable Sensitivities for Large Force Measurements

Brandon Pereles, Andrew DeRouin, Jingfeng Jiang* and Keat Ghee Ong*
Department of Biomedical Engineering, Michigan Technological University
1400 Townsend Drive, Houghton, MI 49931, USA.

Abstract

Magnetoelastic sensors are typically made of strips of magnetostrictive materials that efficiently convert magnetic energy into mechanical energy, and *vice versa*. When exposed to an AC magnetic field, the sensor vibrates, producing a secondary magnetic flux that can be remotely detected. If the frequency of the AC magnetic field matches the sensor's resonant frequency, the magnetic-mechanical energy conversion is optimal, resulting in a large secondary magnetic flux. The magnetoelastic sensor has been used to monitor physical parameters relevant to force, such as mass, since its resonant frequency is dependent on the magnitude of an applied force. Typically, the applied force must be significantly less than the weight of the sensor or it completely dampens the sensor's resonance. Presented here is the design and operation of a magnetoelastic sensor capable of monitoring large forces by applying partial loading to strategic points on a sensor. The characterization and analysis of this new magnetoelastic sensor is presented along with numerical modeling to illustrate the proposed sensing mechanism. Additionally, an array of magnetoelastic sensors were deployed to demonstrate monitoring of force loading on the lock-in portion of a lock-in style lower limb prosthetic sleeve.

Keywords: Magnetoelastic sensor, partial loading, force sensing.

4.1 Introduction

Magnetoelastic sensors take advantage of the magnetostrictive properties of certain magnetic materials. Typically made from amorphous metallic glasses [1], the

dimensions of these materials can be changed by an externally applied time -varying magnetic field, thus longitudinal vibrate [1]. These vibrations produce a secondary magnetic flux, which reaches a peak when the applied excitation field's frequency matches the material's mechanical resonance according to [1]:

$$f_0 = \frac{1}{2L}\sqrt{\frac{E}{\rho(1-\sigma^2)}} \quad (1)$$

where f_0 is the resonant frequency, L is the strip length, E is the sensor's Young's modulus, ρ is the sensor's density and σ is the Poisson's ratio. The changes in the longitudinal vibrations, and thus the secondary magnetic flux, allow this type of sensor to be monitored acoustically with a microphone, magnetically with a sensing coil, or optically with a laser emitter and a photo sensor [1]. Additionally, because the observed resonant frequency is dependent upon the length of the sensor, an array of magnetoelastic sensors can be monitored using a single detection source as long as each sensor has a different length. Many magnetoelastic sensors operate by tracking changes in resonant frequencies as a result of an applied mass to the sensor's surface. The applied mass dampens the vibrations, resulting in a decrease in the resonant frequency. In the case of monitoring chemical concentrations or pH, a mass-changing coating is typically applied to the sensor surface. When exposed to the target of interest, these coatings swell resulting in an increase in the applied mass on the sensor. Several examples include Metglas 2826MB strips coated with poly(acrylic acid-co-isocytlacrylate) for monitoring ammonia [2], pSPMA-IOA and pAA-IOA for salt independent pH monitoring [3] and co-immobilized glucose oxidase and catalyze along with a pH-sensitive polymer for monitoring glucose concentrations [4]. Unlike the monitoring of chemical concentrations and pH, magnetoelastic sensors aimed at monitoring biological targets must have their sensor surfaces functionalized towards a biological target of interest. Some biological targets monitored using functionalized magnetoelastic sensors include avidin [5], *Bacillus anthracis* (responsible for anthrax) [6], *Salmonella typhimurium* [7] and *Escherichia coli* O157:H7 [8].

However, to prevent over-damping of the longitudinal vibrations, the applied masses to these sensors are generally significantly smaller than the mass of the

magnetoelastic sensor [3]. In addition, in most sensing applications, it is also assumed that any coating or applied mass occurs uniformly across the sensor's surface. As a result, magnetoelastic sensors have yet to be widely applied for monitoring large loads and/or for non-uniform loading. Previous work demonstrated that by applying loads at one point, as opposed to uniformly across the entire surface, a magnetoelastic sensor can measure loading of up to 0.98 N [9]. In this work, the magnetoelastic sensor was designed to monitor loads of up to 266 N before losing sensitivity and was deployed in an array onto a 3D printed analog of the lock-in portion of a lock-in style lower limb prosthetic sleeve. Additionally, in the previous work the applied loading was small enough that it was advantageous to apply loads as close to the position of peak vibration as possible to achieve the greatest sensitivity [10]. In contrast, the new design applies loads at the region/regions of least vibration on the sensor. Moreover, the new sensor design also allows for easy customization of sensing range and sensitivity.

4.2. Theory

4.2.1 Mechanics of Partially Loaded Magnetoelastic Sensor

The magnetoelastic sensor monitors the applied loading as a change in its resonant frequency. This phenomenon can be explained by examining the mechanical interactions between the load applicator and the vibrating sensor. As a first approximation, it is reasonable to assume that two surfaces can appear to be in complete contact with one another when they are under an applied loading. However, typically materials have a certain level of surface roughness that can result in contact occurring primarily at the protrusions of the rough surfaces, referred to as asperity regions [11]. As the applied load increases, the materials deform in relation to their respective elasticities, resulting in further contact as the gaps between the surfaces decrease. Eventually the size and number of contact points can no longer increase unless plastic deformation occurs in one or both materials [11]. In the case of a vibrating magnetoelastic sensor, these contact regions represent areas of pinning wherein the magnetoelastic sensor can no longer vibrate. In effect, this results in a decrease in the average length of the sensor, thus increasing its resonant frequency [1].

4.2.2 Numerical Model

A numerical model was developed using ANSYS Mechanical APDL software (Version 13.0, ANSY Inc., PA, USA) to simulate the operation of a partially loaded magnetoelastic sensor. Since the thickness of the sensor was significantly smaller than its width and length (e.g. 26μm vs. 30.5 mm), the model did not consider the material thickness. In constructing the model, Solid 183 was selected as the element for the model with an input elasticity of 100 GPa [12] and a Poisson's ratio of 0.33 [13]. A transient analysis was performed with a time step of 0.198 ms, spanning from 0.198 ms to 300 ms. Following each simulation, the *x*-component of displacement, observed from a single node at the end of the sensor, was extracted from the results. The peak frequency of the collected data was then determined using a Fast Fourier Transform algorithm in Matlab (see **Figure 4.1**). The analysis was then repeated by applying more and more constrained regions at the center of the mesh to simulate increasing contact regions resulting from applied loading.

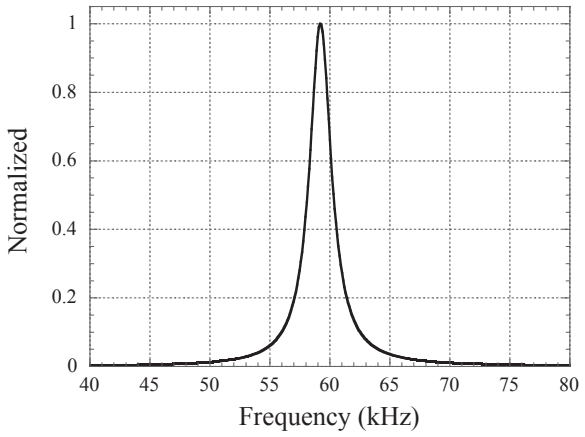

Figure 4.1 The results from the transient analysis were put through a FFT in order to identify the resonance of the simulated sensor.

4.3. Experiments

4.3.1 Sensor and Detector Fabrication

As illustrated in **Figure 2**, the sensors consisted of (a) a frame, (b) a magnetoelastic sensor strip and (c) a load applicator. The frame and load applicator were fashioned from polycarbonate material using a CNC Micro Milling Machine. The design of the applicator in particular was chosen such that the response of the sensor could be controlled by sharing the loads between the four pillars and the portion of the applicator in contact with the sensor, referred to as the applicator head. Lastly, strips of sensing material were sheared from a reel of Metglas 2826MB material purchased from Metglas Inc., Conway USA.

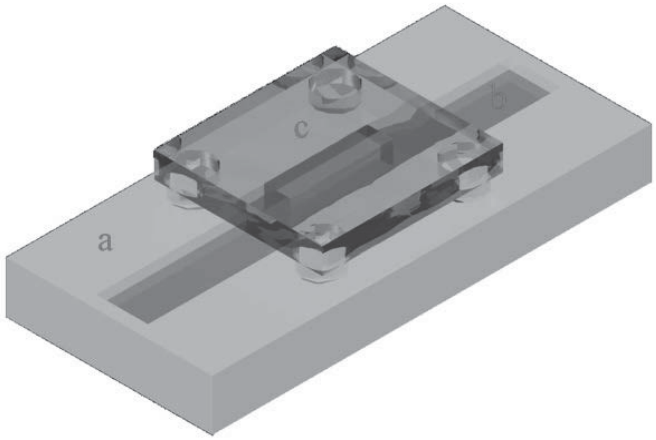

Figure 4.2 The sensor used for characterization consisted of a (a) frame, (b) sensing strip, and (c) applicator.

The fabricated sensor was monitored through an external detector, consisting of two oppositely wound coils connected in a figure-eight configuration. Each detection coil was fabricated using a VFlash FTI 230 Desktop Modeler and measured 13.75 cm × 3.6 mm, and was made of 100 turns of 28 gauge magnet wire. The external AC/DC excitation fields were generated with two circular excitation coils with diameters of 27.6 cm and wound with 50 turns of 26 gauge magnet wire. The excitation coils were separated by 12.5 cm.

4.3.2 Experimental Setup and Procedure

Experiments were conducted to analyze the effects of altering the dimensions of the load applicator on 30.5 mm and 33.5 mm long sensors. In addition to this, the effect

of altering the distance between the load applicator and the sensor, and the impact of changing the roughness and/or elasticity of the materials at the load interface was examined. During testing, sensors were loaded from 0 N to 266 N. Finally, a multi-sensor array was developed and deployed onto a 3D printed lower-limb prosthetic analog to be tested under applied loading.

To measure the resonant frequency of the sensor, AC excitation equipment consisting of a Fluke 271 10 MHz function generation, a Tapco Juice 1400 amplifier, a Stanford Research Systems 810 DSP Lock-in-Amplifier, and a Kepco Bipolar Power Supply were used. A custom Microsoft Visual Basic 6.0 program controlled the process of exciting and monitoring the sensors and the application of desired load regimes using a custom fully automated four piston pneumatic mechanical loader. The collected data and the recorded actual loading were analyzed with a custom Matlab script.

An averaging filter was first applied to the data to reduce noise in the collected results, followed by determination of the resonance frequency for each test. The resonant frequency for each load point was plotted against the applied load and fitted with a decaying exponential curve:

$$y=a\left(1-e^{-bx}\right)+c \tag{1}$$

In this case, the *a* coefficient represents sensor sensitivity and the *b* coefficient represents the signal saturation and dynamic range. The *c* coefficient represents the resonant frequency for an unloaded sensor.

4.4 Results and Discussion

4.4.1 Numerical Model and Effect of Changing Applicator Dimensions

The results of the ANSYS simulations are plotted in **Figure 4.3** which shows the resonant frequency change of applicators of varying widths as a function of their lengths. The applicator's length was used to simulate the change in the contact area between the applicator and the strip due to the applied force – the larger the contact area, the longer the length. The results display a decaying exponential trend similar to the actual sensor response towards altering the length and/or width of applicators measured with a 30.5 mm and 33.5 mm long sensor (see **Figures 4.4** and **4.5**).

In actual testing, a 30.5 mm × 4.0 mm Metglas 2826MB strip was loaded from 0 N to 266 N at 22.2 N intervals with applicator heads whose width was held constant at 1 mm while the length of the applicator was changed from 2 mm to 6 mm at 1 mm intervals between load tests. The collected coefficients from applied decaying exponential curve fitting can be seen in **Figure 4.6**. Similar testing was performed on the effects of loading a 33.5 mm × 4.0 mm Metglas 2826MB from 0 N to 266 N at 22.2 N intervals with applicator heads whose length was held constant at 4 mm and 5 mm while the width of the applicator was changed from 1 mm to 3 mm at 1 mm intervals between tests. **Figure 4.5** shows the results when the length was held constant at 5 mm and **Figure 4.7** plots the collected coefficients from curve fitting the results from the 4 mm and 5 mm long applicators. The results from both sets of testing indicate that increasing the applicator head size increases sensitivity, as indicated by the ANSYS model.

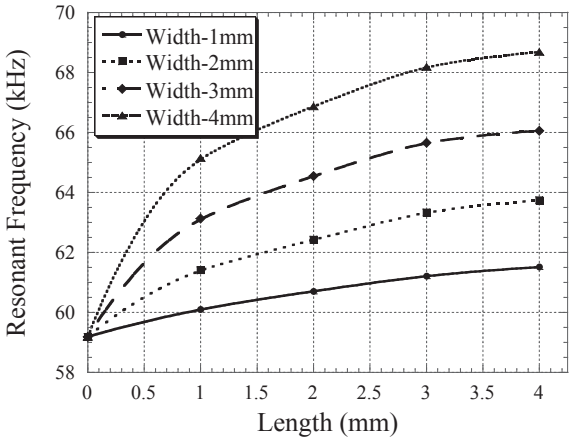

Figure 4.3 ANSY simulations were performed by increasing the area of a constrained region at the center of the strip in order to emulate the average change in contact area with applied load.

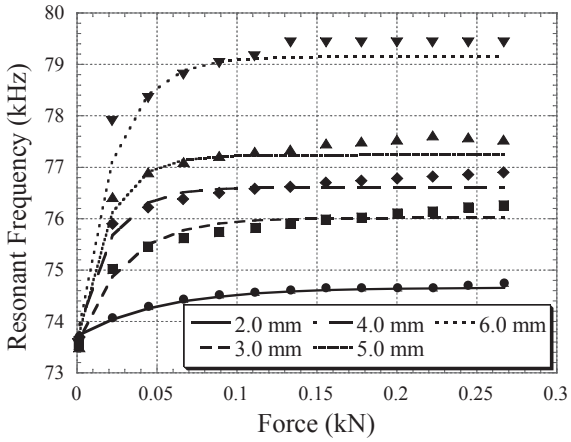

Figure 4.4 The effects of loading a 30.5 mm × 4.0 mm Metglas 2826MB from 0 N to 266 N at 22.2 N intervals with applicator heads whose width was held constant at 1 mm while the length of the applicator was changed from 2 mm to 6 mm at 1 mm intervals between load tests.

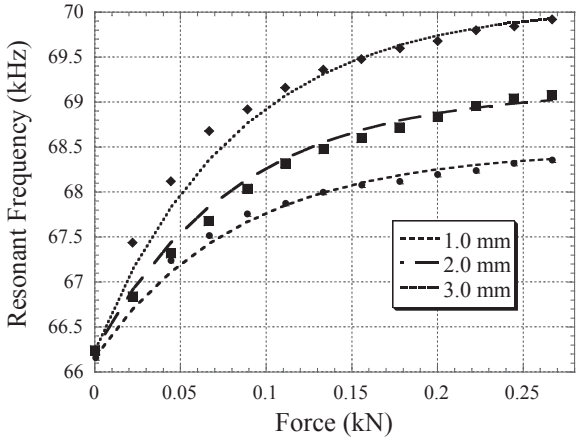

Figure 4.5 The effects of loading a 33.5 mm × 4.0 mm Metglas 2826MB from 0 N to 266 N at 22.2 N intervals with applicator heads whose length was held constant at 5 mm while the width of the applicator was changed from 1 mm to 3 mm at 1 mm intervals.

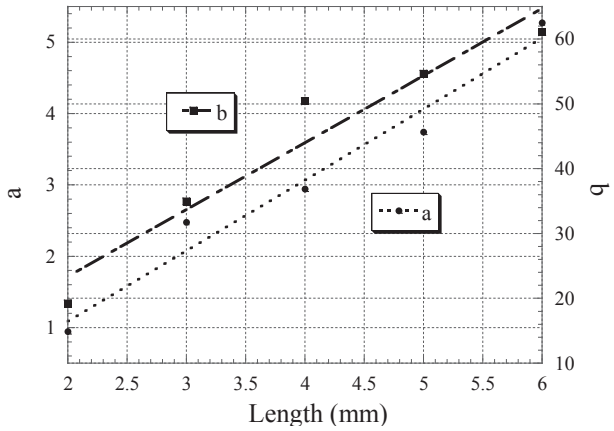

Figure 4.6 The coefficients from decaying exponential curve fits applied to loading results with a 30.5 mm × 4.0 mm sensor strip using applicators having varying lengths from 2 mm to 6 mm at 1 mm intervals.

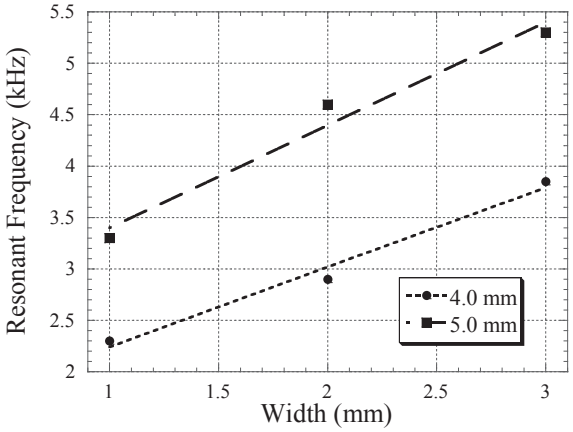

Figure 4.7 The coefficients from decaying exponential curve fits applied to loading results with a 33.5 mm × 4.0 mm sensor strip using applicators having varying widths from 1 mm to 3 mm having lengths of 4 mm and 5 mm.

4.4.2 Effect of Changing Surface Roughness

In order to test the effects of changing surface roughness, a 3 mm × 5 mm applicator was used to load a 30.5 mm × 4.0 mm magnetoelastic sensor from 0 N to 226 N at 22.4 N intervals. The applicator head was then roughened with sandpapers of different grit to alter the surface roughness, and the experiment was repeated. The results of roughening the applicator with sandpaper with particle sizes of 268 mμ, 140 mμ and 92 mμ (in that order), are plotted in **Figure 4.8a** along with a plot of the determined

coefficients in **Figure 4.8b**. Using sandpaper with smaller particle sizes increases the number of available contact regions by creating a surface with less roughness due to the smaller size of abrasive elements on the sandpaper, thus resulting in a greater overall distribution of the applied loading. As a result, a smoother surface decreases the sensor sensitivity due to smaller contact regions, but increases the dynamic range as a result of having more asperity regions capable of contacting the strip.

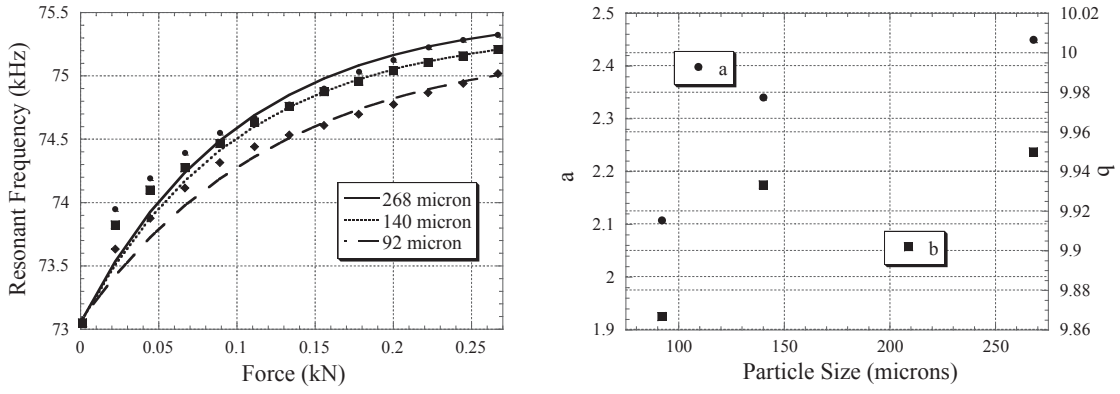

Figure 4.8 The (a) results and (b) coefficients of the applied decaying exponential curve fits from loading a 30.5 mm × 4.0 mm from 0 N to 266 N at 22.2 N with an applicator whose roughness was altered between tests using sandpaper whose particle sizes were 268 mμ, 140 mμ, and 92 mμ.

4.4.3 Effect of Changing Young's modulus

The *ΔE* effect describes the change in Young's modulus of a magnetostrictive material due to an applied magnetic field. As a result, this effect was utilized to examine the outcomes of changing the Young's modulus of the contacting materials on a sensor's response. A 30.5 mm × 4.0 mm sensor experienced loads from 0 N to 133 N at 44.5 N intervals with different applied DC biasing fields from nearly 2.71 A/m to 814.89 A/m at 135.58 A/m intervals, thus altering the Young's modulus of the sensor. The results, in terms of resonant frequency and applied bias field, are plotted in **Figure 4.9**. To further explore the effect of changing the contacting material Young's modulus, the resonant frequency was plot against applied loading while under varying biasing fields (see **Figure 4.10a**). The coefficients from curve fitting were then plot against the applied bias field

(see **Figure 4.10b**). The shape of the *c* coefficient curve in **Figure 4.10b** is similar to the standard ΔE curve [14], which was expected since the *c* coefficients represented the resonant frequencies of the unloaded sensors under varying biasing fields. Interestingly, the *c* coefficient curve has an opposite trend to the *a* coefficient curve. This demonstrates an inverse relationship between the Young's modulus of the strip, and hence the Young's modulus at the contact interface, and sensor sensitivity. This means that when the Young's modulus of the sensor decreased, its resistance to deformation also decreased, leading to an increased number of contact areas when compared to the same material with a higher Young's modulus at the same loading.

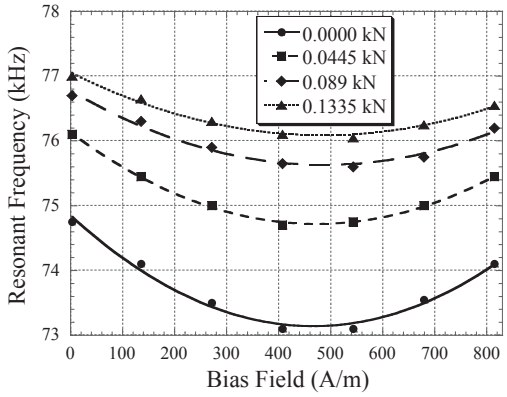

Figure 4.9 In order to evaluate the effects of changing the Young's modulus of components at the contact interface on sensor response, load testing was performed from 0 N to 133 N at 44.5 N intervals on a 30.5 mm × 4.00 mm strip under different applied DC biasing fields ranging from 2.71 A/m to 814.89 A/m at 135.81 A/m intervals.

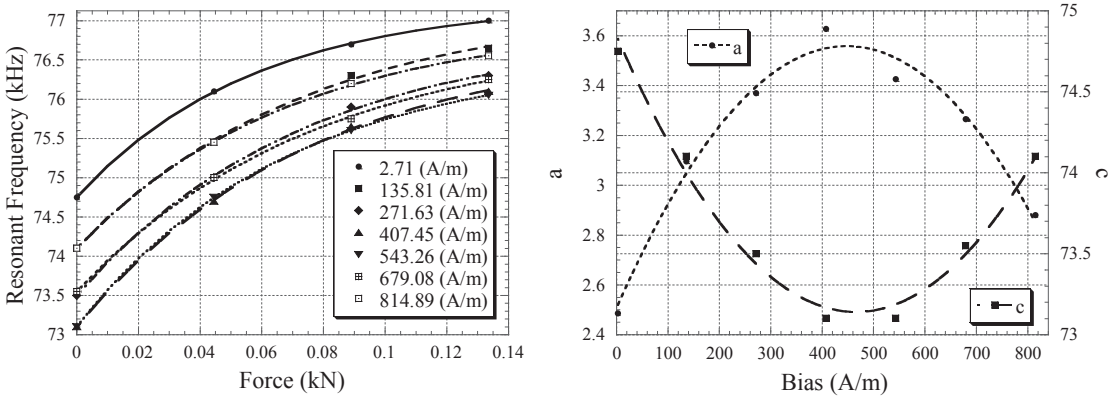

(a) (b)

Figure 4.10 The change in Young's modulus as a result of applied loading under different biasing fields was (a) curve fit with decaying exponential curves and (b) the coefficients were plot against the applied biasing field.

4.4.4 Load Sharing

In addition to testing the effect of changing the load applicator size, the introduction of load sharing to the applicator design was also investigated. Specifically, as can be seen in **Figure 4.2** the load applicator has four supporting posts. As a result, applied loads were distributed between the applicator head and the posts. **Figure 4.11a** shows the results of changing the size of the end of the posts to alter the effective force experienced by a 45 mm × 3 mm sensor tested with load applicators having a 3.0 mm × 1.5 mm applicator head. In each test the load applicator experienced a load from 0 N - 266 N at 44.3 N intervals. The collected data was then curve fitted with decaying exponential curves and the coefficients were plotted against the percent loading experienced by the sensor (see **Figure 4.11b**). This result demonstrates that the range and sensitivity of the sensor can be altered by controlling the size of the posts. Specifically, if a higher portion of the applied load is experienced by the sensor, the sensor sensitivity increases but the overall range decreases.

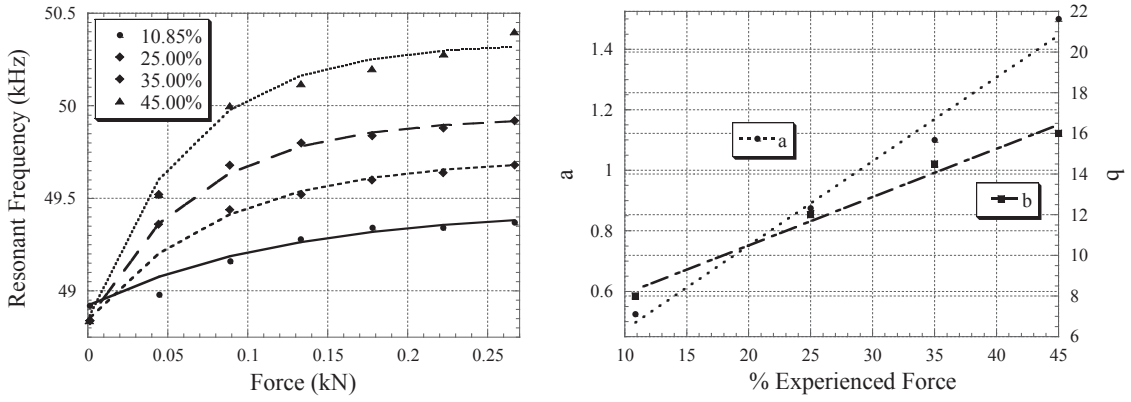

(a) (b)

Figure 4.11 The results of altering the load sharing between the applicator head and support posts were (a) plot against the total applied loading and (b) the coefficients from curve fitting were plot against the percent loading experienced by the applicator head.

4.4.5 Effects of Altering Distance between Load Applicator and Sensor

The effect of altering the distance between the load applicator and the sensor was also analyzed using Metglas 2826MB discs placed underneath the posts of the load applicator prior to testing. During experiments, loads were applied from 0 N – 266 N at 22.2 N intervals. The results from testing and the coefficients from the applied decaying exponential curve fitting are plotted in **Figure 4.12a-b**. The results demonstrate that as the distance between the resonating sensor and applicator head increases, the peak response within the tested range and the sensitivity both decrease. In theory, adding an initial separation between the applicator and sensor decreases the effect of applied loading, as the initial separation gap must first be breached. This increases the overall range of the sensor as fewer contact points are formed for a given load, while also decreasing the overall sensitivity. Additionally, it is worth noting that the curvature of the results when zero discs were present results from the fact that when no discs were present a gap existed between the support posts and the sensing strip. As a result, the sensor did not exhibit the characteristic exponential trend until the applied loading was large enough for the posts to contact the sensor frame.

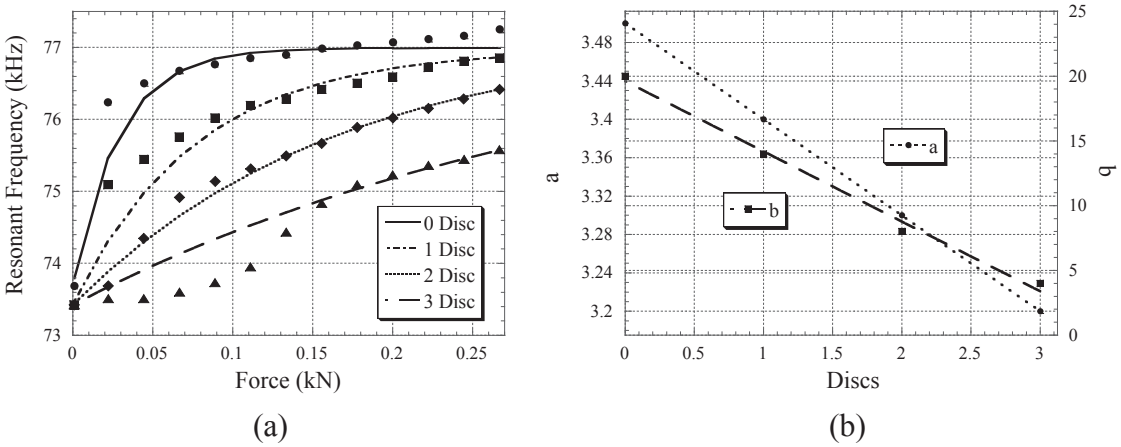

Figure 4.12 The (a) results and (b) coefficients of the applied decaying exponential curve fits from load testing of a 30.5 mm × 4.0 mm sensing strip from 0 N to 266 N at 22.2 N intervals with the distance between the applicator head and sensing strip adjusted from 0.0 μm to 40.0 μm at 20 μm intervals with an initial gap of 20 μm when no insert was placed underneath the support pillars of the applicator.

4.4.6 Hysteresis, Drift and Stability

Hysteresis and drift were quantified by loading a 30.5 mm × 4.0 mm long sensor from 0 N to 266 N and back to 0 N at 22.2 N intervals for 20 cycles (see **Figure 4.13**). The collected data was examined and a maximum of 5.13% average hysteresis and a 0.64% drift in the unloaded response and a 6.96% drift in the peak load response over 20 cycles were found. The error in both drift and stability could be improved in future works by examining the effect of deformation of the load applicator and frame during experiments. Additionally, if the applied loading is not consistently distributed through the applicator's posts, shifting may occur during prolonged or repeated testing, possibly leading to the experienced errors. In future works the design of the applicator will be examined and modified to reduce these errors.

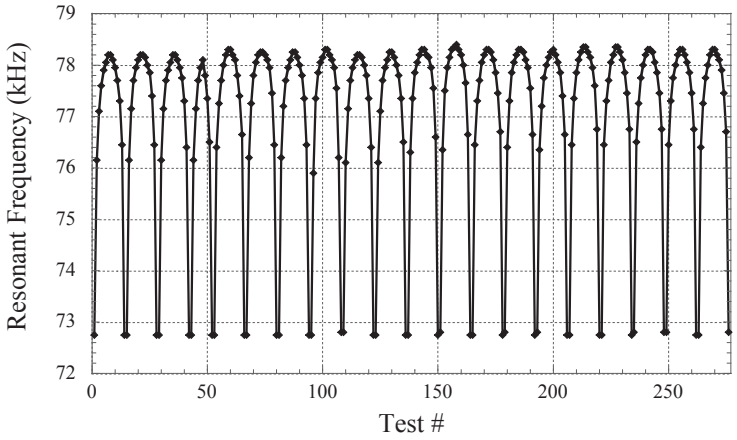

Figure 4.13 The drift and hysteresis of the developed sensor were characterized using a 30.5 mm × 4.0 mm sensor strip loaded from 0 N to 266 N at 44.8 N intervals with a 1 mm × 4 mm applicator head over the course of 20 cycles.

4.5 Implementation to Prosthesis Model

A lower limb prosthetic model was fashioned using a VFlash Desktop 3D Printer (see **Figure 4.14a-b**). Prior to full testing, each sensor in the array was characterized, as per the procedures above, in order to establish an empirical relationship between applied load and resonant frequency shift. The results from this characterization along with the developed curve fits can be seen in **Figure 4.15**. The empirically determined coefficients

were utilized to determine applied loading based on the captured resonant frequency shift.

Following sensor characterization, the prototype was placed into the mechanical loader and equal loads were applied on all four pistons from 0 N to 226 N at 44.4 N intervals. In order to evaluate the effectiveness of the developed characterizations, the total applied force was compared to the total recalculated force (see **Figure 4.16**) with a maximum error of 10%. In the future, this array will not only be expanded to include more elements, but the load applicator design will be modified to improve stability and decrease maximum error.

(a) (b)

Figure 4.14 The lock-in portion of a lock-in style lower limb prosthetic was modified in AutoCad and fabricated using a VFlash Desktop 3D Modeler. (a) Sensor strips and load applicators were inserted into the fabricated test apparatus prior to (b) fully assembling the proof of concept test apparatus.

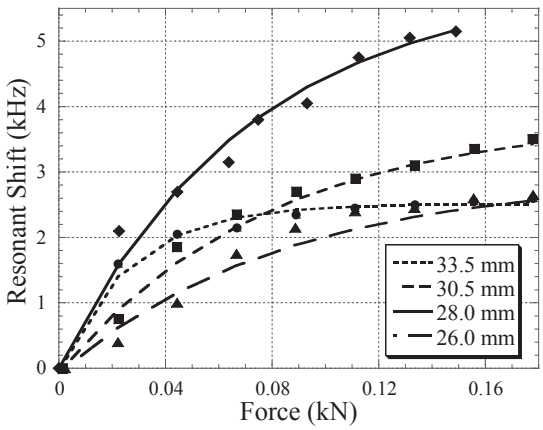

Figure 4.15 Each sensor strip in the test apparatus was characterized to develop a solving method for determining the applied loading from the

resonant frequency by loading each element in the array from 0 N to 178 N at 22.2 N intervals.

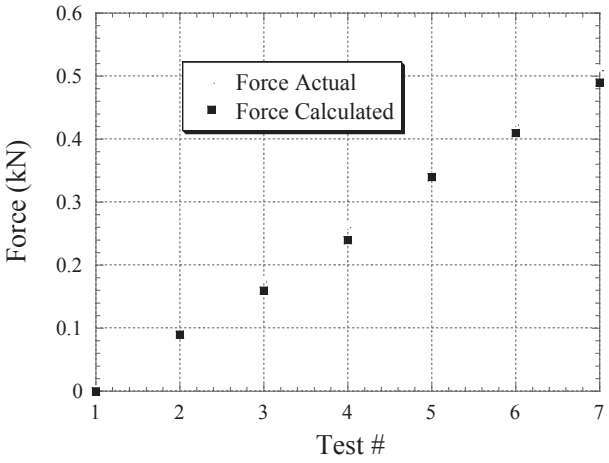

Figure 4.16 Results from loading the assembled and instrumented test apparatus used to calculate expected loading with a maximum 10% error.

4.6 Conclusion

A new magnetoelastic sensor platform for monitoring applied loading was presented. The new design allows for application of partial loading to the center of a vibrating magnetoelastic sensor. The ability to control the sensor range and sensitivity by altering parameters such as the applicator head size, Young's modulus/surface roughness of the interface and the distance between the load applicator and sensor was also illustrated as part of characterization of the sensor platform. The sensor also illustrated a maximum of 5.13% average hysteresis, 0.64% drift in the unloaded state, and a 6.96% drift in the peak load response over 20 cycles. Moreover, a sensor array tested on a lower limb prosthetic had a maximum 10% error when comparing the actual total applied force against the total applied force determined by from curve fits obtained during sensor characterization. Future works include modifying the load applicator design to improve drift and hysteresis as well as decreasing sensor size and increasing the maximum array size.

Acknowledgments

Pereles was supported by the Department of Defense (DoD) through the National Defense Science & Engineering Graduate Fellowship (NDSEG) Program. The authors would like to acknowledge Northern Orthotics & Prosthetics Inc. for contributions to this work.

References

1. Grimes C.A., Roy S.C., Rani S. and Cai, Q., Theory, Instrumentation and *Applications* of Magnetoelastic Resonance Sensors: A Review. *Sensors (Basel)*, [Online], vol. 11, no. 3, pp. 2809-2844, 2011.
2. Cai Q.Y., Jain M.K. and Grimes C.A., "A wireless, remote query ammonia sensor," *Sensor. and Actuat. B-Chemical*, vol. 77, no. 3, p. 614-619, 2001.
3. Cai Q.Y. and Grimes C.A., "A salt-independent pH sensor," *Sensors and Actuators B: Chemical*, vol. 79, no. 2–3, pp. 144-149, October 2001.
4. Gao X., Yang W., Pang P., Liao S., Cai Q., Zeng K., and Grimes C.A., "A wireless magnetoelastic biosensor for rapid detection of glucose concentrations in urine samples," *Sensor. and Actuat. B-Chemical*, vol. 128, no. 1, pp. 161-167, December 2007.
5. C. Ruan, Z. Kefeng, O.K. Varghese and Grimes C.A., "A magnetoelastic bioaffinity-based sensor for avidin," *Biosens. and Bioelectron.*, vol. 19, no. 12, pp. 1695-1701, July 2004.
6. Wan J., Johnson M.L., Guntupalli R., Petrenko V.A. and Chin B.A., "Detection of Bacillus anthracis spores in liquid using phage-based magnetoelastic micro-resonators," *Sensor. and Actuat. B-Chemical*, vol. 127, no. 2, pp. 559-566, November 2007.
7. Lakshmanan R.S., Guntupalli R., Hu J., Petrenko V.A., Barbaree J.M., and Chin B.A., "Detection of Salmonella typhimurium in fat free milk using a phage immobilized magnetoelastic sensor," *Sensor. and Actuat. B-Chemical*, vol. 126, no. 2, pp. 544-550, October 2007
8. Ruan C., Zeng K., Varghese O.K., and Grimes C.A., "Magnetoelastic immunosensors: amplified mass immunosorbent assay for detection of Escherichia coli O157:H7," *Anal. Chem.*, vol. 75, no. 23, pp. 6494-6498, December 2003.
9. Pereles B.D., Dienhart T., Sansom T., Johnston K., and Ong K.G., "A Wireless, Passive Load Cell based on Magnetoelastic Resonance," *Smart Mater. Struct.,* vol. 21, no. 7, July 2012.
10. Ramasamy M. and Prorok B.C., "Resonance Behavior of Magnetostrictive Sensor in Biological Agent Detection," in *Experimental and Applied Mechanics, Volume 6*, pp. 875-876, 2011.
11. Persson B.N.J., "Contact mechanics for randomly rough surfaces," *Surf. Sci. Rep.*, vol. 61, no. 4, pp. 201-227, June 2006.
12. "Magnetic Alloy 2826MB (nickel-based), Technical Bulletin, Metglas®, <http://www.metglas.com/assets/pdf/2826mb.pdf>.
13. Ramasamy, M., "Resonance Behavior of Magnetostrictive Sensor in Longitudinal

Vibration mode for Biological Agent Detection," *M.S. thesis, Dept. Matr. Eng.*, Auburn Univ., Auburn, ALA, 2010.
14. Ong K.G., Mungle C.S. and Grimes C.A., "Control of a magnetoelastic sensor temperature response by magnetic field tuning*," IEEE Trans. Magn.*, vol. 39, no. 5, pp. 3414-3416, September 2003.

Chapter 5 A Wireless, Magnetoelastic-based Sensor Array for Force Monitoring on a Hard Surface

Brandon D. Pereles, Andrew J. DeRouin, Thomas A. Dienhart, Ee Lim Tan, Keat Ghee Ong*

Department of Biomedical Engineering, Michigan Technological University, Houghton, MI 49931, USA.

* Corresponding author: kgong@mtu.edu

Abstract

A force monitoring system consisting of stress-sensitive magnetoelastic strips for remotely measuring the force profile across a hard surface is described. Under the excitation of a magnetic AC field, the magnetoelastic strips generated higher-order harmonic fields (magnetic AC fields at multiple frequencies of the excitation field), allowing remote measurement of their responses without interference from the excitation field. Due to their magnetoelastic properties, these higher-order harmonic fields were also dependent on the applied force and, as a result, variations in force/stress could be tracked via changes in the field amplitudes. These changes were monitored using a detection system featuring a set of magnetic detection coils, which captured the response of the magnetoelastic strips. To demonstrate the functionality of this sensor system, a three-strip magnetoelastic sensor array was fabricated on a flat polycarbonate substrate. The substrate, placed within a customized mechanical loader, was exposed to a variety of force loading conditions. Experimental results demonstrated a proportional relationship between the amplitude of the 2nd order harmonic field and the applied force. An algorithm was developed to[2] identify the magnitude of the applied force. The novelty of this system lies in its wireless and passive nature, which is ideal for applications in which wires and internal power sources are prohibited or discouraged. Moreover, the sensing component of this system is an array of thin magnetoelastic strips, allowing for minimal modifications to existing structures during implementation.

[2]"The material in this chapter was previously published in *Sensor Letters*."

Keywords: Magnetic Higher-Order Harmonic Fields, Magnetoelastic, Wireless, Passive, Force Sensors, Mechanical Loading.

5.1 Introduction

Force and stress are generally measured via strain, which is defined as the change in dimensions of an object due to an applied force. In practice, strain is often measured with strain gauges, most of which can be classified as resistive, capacitive, or vibrational. Resistive strain gauges monitor strain as a function of the change in resistance across a conductive or semiconductive material when elastically deformed [1]. Semiconductive materials exhibit piezoresistive behavior, resulting in a larger change in the electrical response with applied force compared to conductive materials [2]. As a result, semiconductive materials exhibit higher gauge factors, typically between 50 and 200, while conductive materials experience less than 5 [1]. These piezoresistive strain gauges find common use in different fields for a variety of applications, such as measuring stress on a knee prosthesis [3] or stress monitoring during an electronic packaging process [4]. While semiconductor strain gauges offer accurate sensing on small scales, their response can vary with temperature, and they can be difficult to manufacture.

Capacitive strain gauges measure stress/strain as a function of the change in the capacitance of a sensor. The primary advantages of capacitive strain gauges come from their capacity to operate in high temperature environments, minimal hysteresis, and long-term stability [4]. However, they have a lower sensitivity compared to their piezoresistive counterparts. For example, thick cermet and polymer based capacitive strain gauges demonstrated similar linear responses and hysteresis to piezoresistive sensors but with gauge factors of only 6 for the cermet capacitor and 3.5 for the polymer capacitor [5].

Vibrating wire strain gauges function by measuring the vibrating frequency of a wire held in tension between two anchoring points and excited into vibration by a magnetic coil. Due to the effects of applied stress/strain, the anchoring position changes, resulting in a measurable alteration in vibrational frequency [1]. Due to their high sensitivity, vibrating strain gauges are commonly used in low strain structures such as

concrete beams [6]. As a whole, strain gauges in this category have the advantage of stress detection in the range of parts per million and are robust, easily attachable, and accurate; however, changes in temperature can drastically affect their performance [7].

Fiber optic technology has also been used for stress monitoring. The advantages of fiber optics include electrically passive operation, EMI immunity, high sensitivity, and multiplexing capabilities. Two main types of fiber optic strain sensors exist: interferometric and intensiometric. Interferometric methods observe changes in light passing through the fiber optic cable, while intensiometric sensing techniques monitor changes in the radiant power transmitted in a cable. A common example of an interferometric sensor is the Fabry-Perot interferometer sensor, which measures the change in light intensity between two mirrors placed in parallel with the fiber optic cable. An applied stress alters the distance between the mirrors resulting in a phase change in the light. While highly accurate, this method exhibits an inability to handle periodic interruptions by the power supply [8,9]. Additionally, fiber optic sensors are prone to damage, are affected by temperature elevations, and require that any coating used to protect fiber optic wires allow for proper transfer of force to the sensors [10].

Wireless capacitive stress/strain sensors were also developed for monitoring pressure as a function of change in measured capacitance. One such device coupled an RF transceiver to a custom capacitor for pressure monitoring [11]. The device was comprised of a pressure sensitive cavity, fabricated through silicon fusion bonding of two silicon wafers used to seal the cavity, and a flexible and a stationary electrode, forming a capacitor. Pressure applied to the device deflected the flexible electrode toward the fixed electrode, thus altering the capacitance of the sensor. Using a RF transceiver, information was wirelessly collected and sent for analysis [11]. Another wireless capacitive sensor, known as the SmartPill, incorporated pressure, pH, and temperature sensors for monitoring gastrointestinal tract conditions [12]. Unfortunately, these systems are limited in their size by the necessity for onboard electronics and, in the case of an active sensor, may eventually require the device to be removed in order to replace the power supply.

A simpler version of wireless capacitive stress/strain sensors was realized by incorporating an inductive-capacitive (LC) tank circuit into a sensor. In a wireless,

passive stress/strain LC sensor, the capacitive stress/strain element connected to an inductor, which remotely conveyed stress/strain information as a change in the resonant frequency of the tank circuit. Among the applications of this type of sensor are monitoring stent integrity after an endovascular repair procedure [13] and measuring pressure in automobile tires [14].

Another class of passive stress/strain sensors is based on amorphous magnetoelastic materials. When exposed to a time varying AC field, magnetoelastic materials vibrate due to the magnetoelastic effect. The magnetoelastic effect also causes the vibrating magnetoelastic material to generate a magnetic flux that reaches a peak at its mechanical resonant frequency [15,16]. When an internal stress is applied, the resonant frequency of the strip becomes stress dependent, and, as an example, has been used to determine atmospheric pressure [15,16]. This sensor is not only passive and wireless, but also low cost and long lasting. However, the strip itself must be stressed (by bending) to act as a sensor and there is no reliable way to control its sensitivity.

A strain sensor was developed using magnetoelastic materials by Kouzoudis and Mouzakis [17]. A Metglas 2826 MB ribbon was attached on an epoxy resin slab and exposed to vibrations of varying amplitudes and frequencies. Due to its magnetoelastic property, the vibration of the magnetoelastic material caused a change in its magnetization stages, which was remotely picked up by a nearby detection coil. The sensor was demonstrated to have a strain gauge factor of 11,700 at a vibration frequency of 150 Hz.

Due to magnetic softness, amorphous magnetoelastic materials also generate higher order harmonic fields (magnetic fields at multiple frequencies of the excitation field) when under the excitation of a low frequency AC magnetic field [18]. To visualize the higher-order harmonic fields, the magnetoelastic material is generally excited by a steady AC magnetic field along with a sweeping DC biasing field. The biasing field alters the magnitude of the higher order harmonic fields and thus produces a distinct pattern as shown in **Figure 5.1**. In the previous work, it was shown that the amplitude of the higher-order harmonic fields increased when force was applied along the length of a magnetoelastic strip [19].

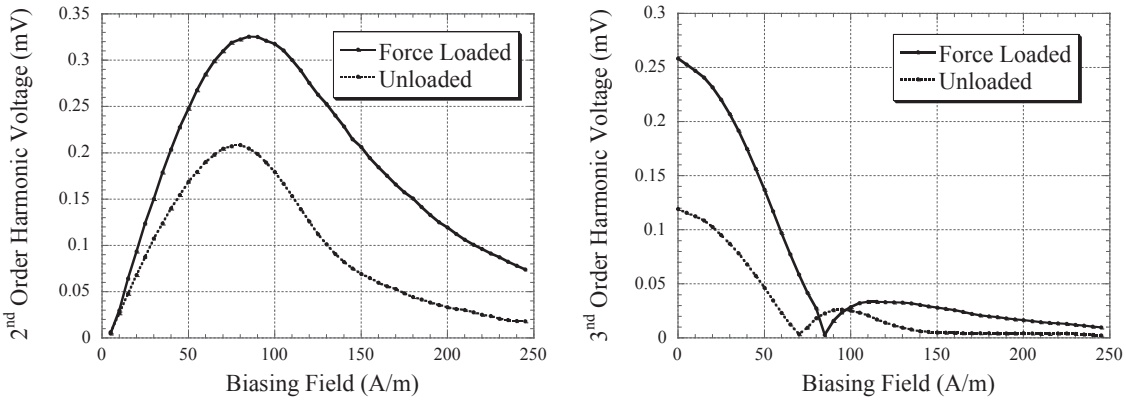

Figure 5.1 The (a) 2nd order harmonic field and (b) 3rd order harmonic field measured as a function of an applied DC field with and without an applied force.

This paper describes a force monitoring system that tracked the changes in the 2nd order harmonic amplitudes of an array of magnetoelastic strips. By using an array of magnetoelastic strips, the new system is able to monitor not only the total contact force on the surface, but can also determine the force distribution on the surface. In contrast to the previous work [18], force was applied directly onto the surface instead of along the length of the magnetoelastic strip. Similar to the previous work, however, the application of force on the magnetoelastic strip surface resulted in an increase in the 2nd order harmonic field (see **Figure 5.1**).

By capturing the response of each strip, the system could identify the position and magnitude of the applied force. This sensing system was not only wireless and passive, but also simple to implement since it was nothing more than an array of magnetoelastic strips directly applied onto the desired surface. The process reduces cost and will allow for the production of long lasting sensors for a variety of applications.

It is worth noting that the presented sensor differs from other devices based on magnetoelastic materials, such as those described by Kouzoudis and Mouzakis [17] in terms of operating principle, ideal application, and strengths and weaknesses. For instance, to obtain good sensitivity, Kouzoudis' sensor system required the substrate to vibrate and the sensor sensitivity was also proportional to the vibrational frequency. The described sensor, on the other hand, does not require the substrate to vibrate, and its

sensitivity is largely related to the magnetoelasticity of the material. Moreover, unlike Kouzoudis' system, the described sensor uses the higher-order harmonic signals from the material to track pressure and stress. The use of higher-order harmonic signals can significantly remove the background excitation signal, thus increasing the signal to noise ratio. Furthermore, the major applications for both technologies are different due to the differences in their operating principle. Thus, the described sensor is better suited for stress and pressure monitoring while Kouzoudis' sensor system is ideal for strain monitoring.

5.2 Experiments

5.2.1 Sensor Fabrication and Experimental Setup

The sensor, illustrated in **Figure 5.2**, was cut from a block of polycarbonate material and measured 47 mm × 56.5 mm × 12.2 mm. Metglas 2826MB ribbon ($Fe_{40}Ni_{38}Mo4B_{18}$), purchased from Metglas Inc, Conway, SC, USA, was used as the magnetoelastic stress sensing material due to its large magnetostriction (>12 ppm), high permeability (>50,000), and low magnetic coercivity. Three sensing strips were sheared from a 26 m thick Metglas ribbon to 50 mm× 5 mm, and were adhered to the upper surface of the block using cellulose adhesive tape (50 m thick). Adhesive tape was found to introduce less internal stress than glue or epoxy, thus preserving sensor-to-sensor reproducibility. For convenience, these sensing strips were labeled Strip 1, 2, and 3 respectively.

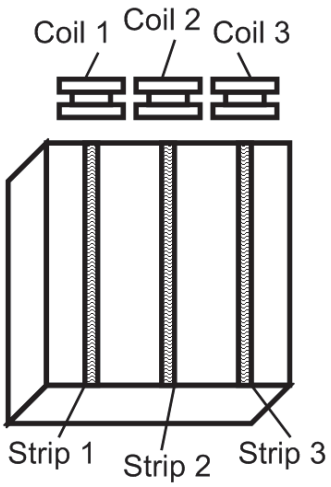

Figure 5.2 The sensor was comprised of three magnetoelastic sensing strips affixed to a polycarbonate substrate.

An automated pneumatic mechanical loader (see **Figure 5.3**) was constructed to apply controllable force to each strip of the sensor. **Figure 5.3** also illustrates the control elements of the automated system. A manual air control valve allowed for adjustments to the overall air flow into the apparatus. Following the main valve, the air was split between an EVP series Proportional Control Valve (Clippard Instrument Laboratory, Inc. 7390 Colerain Ave., Cincinnati, Ohio 45239) and a pneumatic piston. Opening or closing the EVP valve by increasing or decreasing the voltage from a connected Kepco 10 V Programmable Power Supply altered the volume of air flowing to the pneumatic piston. This in turn affected the force applied by the piston. Applied force was monitored using a Measurement Specialties FC23 Compression Load Cell, placed between the load applicator plate and the piston. An Extech 382202 DC Power Supply provided the input voltage to the load cell and applied force data was monitored and transferred to a PC using a Hewlett Packard 3478A Multimeter. A custom Visual Basic program calculated the difference between the actual applied force and the desired force which was then altered using an integral control algorithm to produce an appropriate change in voltage to be sent to the EVP valve. The system provided repeatable loading with a range of 0–355.86 N and was capable of adjusting the force by 4.44 N ± 1.11 N. In addition to automated force loading, the system and Visual Basic program allowed for simultaneous collection of sensor responses from the detection coils. It is worth noting that the range

and weight increment of the system were set for the purposes of this testing by adjusting the air pressure into the system, the air flow at the main regulator, the coefficient used in calculating the change in voltage to the EVP valve, and the time allowed between weight increments for the system to settle.

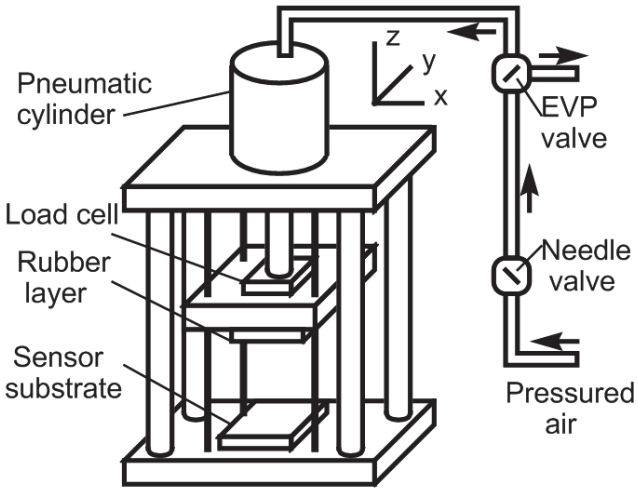

Figure 5.3 The mechanical loader housed the sensor and allowed for incremental loading of the sensing strips. The total applied force was measured with a load cell.

Rectangular detection coils consisted of a functioning coil connected to an oppositely wound compensating coil in series, both made of 100 turns of 36 gage copper wire. The individual coils measured 12.0 mm × 17.6 mm × 4.3 mm. For convenience, the detection coils were labeled Coil 1, 2, and 3 according to the strip being measured (see **Figure 5.2**), and the compensating coils were similarly labeled Compensating Coil 1, 2, and 3. During the experiments, Strip 1, 2, and 3 were aligned to the centers of Coil 1, 2, and 3, respectively.

The sensor was secured within the mechanical loader and the apparatus was positioned directly in front of the detection and excitation coils. As illustrated in **Figure 5.4**, the detection coils were connected to an Agilent spectrum/network analyzer 4396B to capture the signal for the PC (through a custom Visual Basic program and GPIB interface) for further analysis. The excitation coils consisted of two superimposed 50 turn 18-gauge coils (28 cm in diameter) that provided the AC and DC excitation fields. One

coil was connected to an AC function generator (Fluke 271 10 MHz) and an amplifier (Tapco J1400), while the other coil (DC) connected to a Kepco MBT 36–10 MT power supply. In all tests the AC field was 150 A/m, 200 Hz and the DC field was 0–250 A/m.

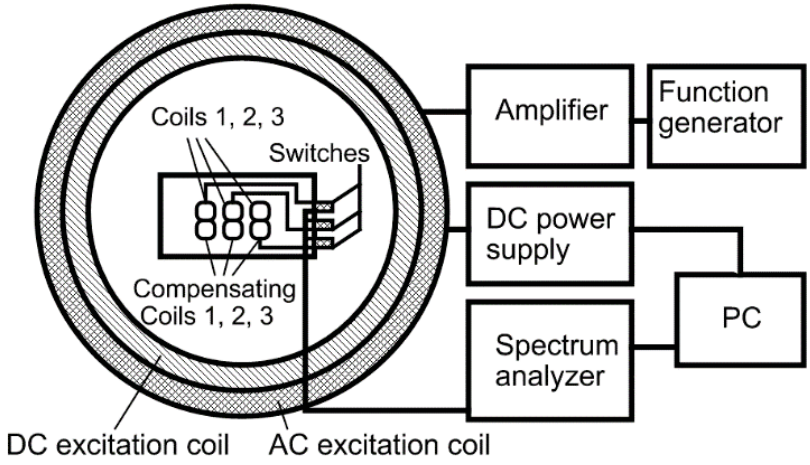

Figure 5.4 The full experimental setup illustrating the excitation coils and the detection coils. During the experiments, the mechanical loader (not shown here) and the test substrates were placed directly in front of the detection coils so Strip 1, 2, and 3 were directly aligned to Coil 1, 2, and 3, respectively.

5.2.2 Experimental Procedure

The response of each magnetoelastic strip was collected while the total applied load increased from 0 to 266.89 N and then decreased to 0 N at weight increments of 22.24 N. During the experiment, data was collected simultaneously from all coils following a short period to allow the piston to reach the desired load and stabilize there. The collected data was then zeroed to a common starting point by subtracting a zero load value obtained from the first data point. This procedure was repeated for a variety of loading conditions created by placing rubber inserts over specified strips, thus producing conditions where in some strips were loaded and others were not.

In addition to changing with the application of force, the response of the sensing strips also varied as a function of relative location from the detection coils. To investigate the effect of changing sensor location, strip responses were measured while moving the mechanical loader incrementally on the x, y, and z axes of a rectangular coordinate

system. The origin of the coordinate system was defined as the exact center between Coil 2 and Compensating Coil 2 (see **Figures 5.3** and **5.4**).

5.2.3 Theory

The pressure sensitivity of the magnetically soft magnetoelastic material can be explained by the magnetic susceptibility (χ), which is the ratio of saturation magnetization (M_s) to anisotropy field (H_k) expressed as [20]:

$$\chi = M_s / H_k \tag{1}$$

The anisotropy field of a magnetic material can be related to the tensile stress along the magnetization direction as [16]:

$$H_k = H_{k0} - 3\lambda_s \sigma_x / M_s \tag{2}$$

where H_{k0} is the anisotropy field at zero stress, λ_s is the saturation magnetostriction of the material, and σ_x is the tensile stress along the magnetization direction, which is also along the length of the sensor.

Equation (2) describes the change in anisotropy field due to the tensile stress along the sensor's length; however, for this particular application, force was loaded on the dominant surface of the ribbon shape sensor (along the *z*-direction shown in **Figure 5.2**). Therefore, the transverse stress on the sensor surface (*z*-direction) was related to the tensile stress along the sensor length (*y*-direction) using the Poisson's ratio υ as:

$$\sigma_x = 2\,\sigma_y / \upsilon \tag{3}$$

Note that a scaling factor of two was added in Eq. (3) to compensate for the fact that only one side of the sensor was being stressed.

As shown in Eq. (2), increasing stress decreases the anisotropy field of a magnetic material, assuming the anisotropy energy and the saturation magnetization stay constant. The change in anisotropic field has a direct impact on the measured signal amplitude of the *n*-th order magnetic harmonic field (A_n), in Volts, which can be described by the equation [17]:

$$A_n = \frac{kLB_s\omega}{\pi} \left| e^{jn\pi H_{dc}/h_{ac}} \cos(\pi n) - \frac{h_{ac}}{\pi n H_k} \sin\left(\frac{\pi n H_k}{h_{ac}}\right) \right| \tag{4}$$

where L is a variable that accounts for sensor-coil coupling, B_s is the saturation induction flux (for ferromagnetic materials, $B_s \approx M_s$), ω is the radian frequency of the fundamental order, h_{ac} is the AC excitation field, and H_{dc} is the DC biasing field. Under an externally applied load, the sensor material deforms and generates an internal stress. Eqs. (1) – (4) indicate that stress causes a change in magnetic anisotropy, which alters magnetization and changes the higher-order magnetic fields allowing for remote detection of pressure.

As indicated in Eqs. (1) and (2), χ is inversely proportional to H_k, which decreases linearly with increasing σ_x. As a result, the susceptibility of the material is expected to show an exponential pattern with increasing stress and eventually converge on an asymptote at infinity as H_k approaches zero. While theoretically this represents an infinite increase in susceptibility, and thus an infinite increase in the 2nd order harmonic amplitude, realistically the change in the susceptibility and the 2nd order harmonic amplitude will more likely resemble an upper bounded decaying exponential curve since the susceptibility will experience a much slower change when the anisotropy has reached a near zero state.

5.2.4 Determination of the Force Loading

An algorithm was developed to determine the force loading on each magnetoelastic strip based on the measured 2nd order harmonic amplitudes. Since the measured 2nd order harmonic amplitudes of the magnetoelastic strips were expected to follow an upper bounded decaying exponential function with increasing stress, upper bounded decaying exponential curves were used to fit the measured data. Due to the close proximity of the magnetoelastic strips to one another, the stress response of each magnetoelastic strip was also dependent on the loading conditions of its neighboring strips. This result is expected, based upon the simple fact that neighboring magnetic fields will interact with one another. Therefore, assuming the strip-to-strip cross interference is cumulative at a given detection coil, the measured 2nd order harmonic amplitude of magnetoelastic Strip i (measured by the i^{th} detection coil) was represented by the summation of the responses of all strips as:

$$S_i = \sum_{j=1}^{3} A_{ij} \left(1 - e^{-a_{ij} f_t}\right) \quad (5)$$

where S_i is the measured 2nd order harmonic amplitude at Coil i, A_{ij} is the peak amplitude measured at Coil i when only strip j is at maximum loading, a_{ij} is the decay coefficient (at Coil i when strip j was loaded), and f_j is the applied force at Strip j.

Equation (5) consists of three upper bounded decaying exponential equations with three unknowns. To solve Eq. (5), a simple iterative method was developed to identify f_j for a set of given S_i. Starting with a set of estimated force loading, the iterative process determines the difference (δ_i) between the calculated S_i from Eq. (5) and the measured signal S_i as:

$$\delta_i = S_i(Calculated) - S_i(Measured) = S_i = \sum_{j=1}^{3} A_{ij} \left(1 - e^{-a_{ij} f_t}\right) - S_i(Measured) \quad (6)$$

A zero δ for all strips indicates the correct input for the force loadings; in contrast, a non-zero δ indicates there is an error in the calculated force loadings. The erroneous force loading g_j is determined from δ_i as:

$$\delta_i = A_{ij} \left(1 - e^{-a_{ij} g_j}\right) \quad (7)$$

The new estimated force loading f_j^{t+1} is determined by subtracting the current force loading to the erroneous force loading g_j:

$$f_j^{i+1} = f_j - g_j = f_j + \frac{\log\left(1 - \delta_i / A_{ij}\right)}{a_{ij}} \quad (8)$$

Equations (6) and (7) are iteratively solved until $f_j^{t+1} - f_j < \varepsilon$, where ε is the acceptable error of the iterative solution.

5.3 Results and Discussion

Figure 5.5 plots the signal recorded by Coil 1, 2, and 3 when rubber inserts were placed on Strip 1 (**Figure 5.5(a)**), 2 (**Figure 5.5(b)**), or 3 (**Figure 5.5(c)**), respectively. These results indicate that when the magnetoelastic strips were under direct force loading, the signal recorded by their corresponding coils increased following an upper bounded decaying exponential function: $a\left(1 - e^{-x}\right)$, confirming the theoretical behavior of

the strips described previously. Also noticeable is that in **Figure 5.5(a)**, the stress response measured at Coil 2 was not zero, but instead was about 25% of the stress response measured at Coil 1, even though Strip 2 was not loaded. This is due to interference from Strip 1. In contrast, Coil 3 measured a zero response because the interference from Strip 1 was shielded by Strip 2 before reaching Strip 3. **Figure 5.5(c)** shows a similar response as **Figure 5.5(a)** since the sensor was symmetrical; however, the response at Coil 3 was slightly lower compared to Coil 1 due to minor differences in physical dimensions between Coil 1 and 3.

Similarly, **Figure 5.5(b)** indicates that Strip 2 interfered with measurements at Coil 1 and 3. Ideally, the measurements at Coil 1 and 3 should be identical but the response at Coil 3 was slightly smaller than Coil 1 due to differences in coil dimensions. Also, compared to **Figure 5.5(a)**, the change in harmonic amplitude was higher when Strip 2 was loaded since Strip 2's response was interfered with by both Strip 1 and 3, while in **Figure 5.5(a)** only Strip 1 interfered significantly with Strip 2.

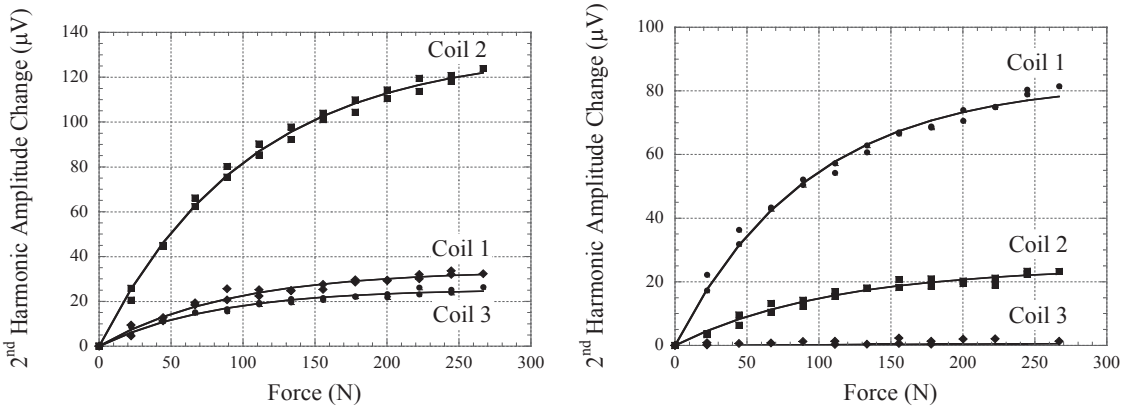

(a) (b)

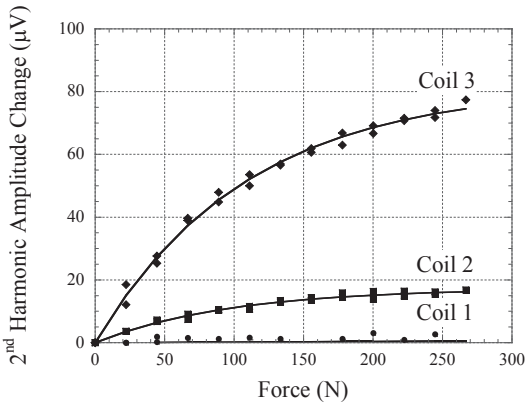

(c)

Figure 5.5 Changes in the 2nd order harmonic amplitude captured by Coil 1, 2, and 3 when only Strip 1 (a), 2 (b), or 3 (c) was loaded, respectively.

After determining the coefficients A_{ij} and a_{ij}, the performance of the iteration process was examined. To prevent measurement errors from affecting the iteration process, all input measurements S_i were calculated using Eq. (5). **Figure 5.6** plots the estimated force loadings for all strips at each iteration step (initial force loadings were set to zero). It was found that the performance of the iteration process degraded with increasing force loading and that in the worst case scenario (156.58 N loading), the error (ε) was 0.35% after 1000 iterations and 0.0075% after 2000 iterations.

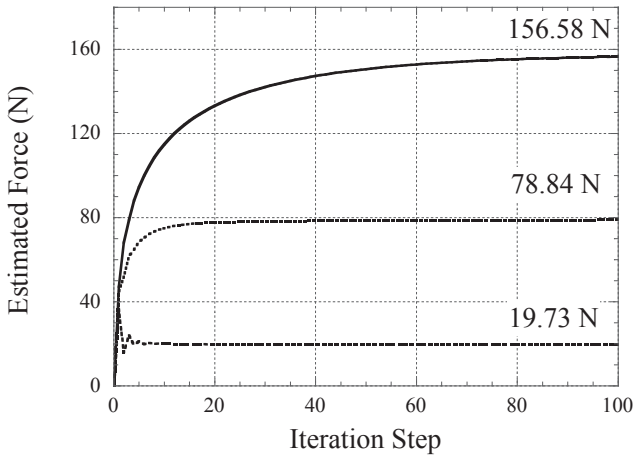

Figure 5.6 Force loading on the magnetoelastic strips estimated by the iterative process as a function of iteration step. The numbers in the figure are the expected

To determine the performance of the whole sensor system, all magnetoelastic strips were loaded and the responses from Coil 1, 2, and 3 were measured simultaneously. The measurements were then fed into Eqs. (6) and (8) to iteratively solve for the force loading on each strip. **Figure 5.7** plots the absolute percentage error between the actual and calculated forces on all strips at different force loading conditions. Although the iteration process has an error of only 0.0075% after 2000 iterations, due to uncertainties in the measured data and other experimental errors, the calculated force has a 10% error when compared to the measured force. One source of error was from the current method of force application. Rubber inserts were used to distribute load on the strips. When the rubber inserts were placed on different strips, the force distribution was assumed to be equally distributed among the strips. In practice, some strips may experience more force than the others due to slight imbalances of the loading plate. As a result, the measured force on each strip might vary slightly from the actual load on the strip. Another source of error was the exponential nature of the data. As shown in **Figure 5.5**, the sensitivity of the sensor decreased with increasing force loading as the upper bounded decaying exponential curve saturated. As a result, the accuracy of the sensor decreased, especially in high load regions, leading to larger errors.

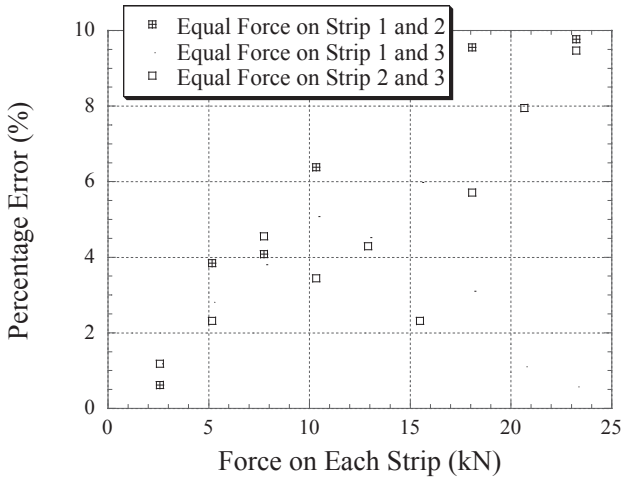

Figure 5.7 The percentage error between the actual and calculated forces on all strips at different force loading conditions.

In addition to characterizing the sensor response under loading and analyzing the developed algorithm, the effects of movement on sensor response were also analyzed. The signal at Coil 2 was recorded and presented in **Figure 5.8** when the sensor was incrementally moved on the *x*, *y*, and *z* axes. While moving along the *x*-axis, the measured amplitude increased when each sensing strip was closer to the center of the coil and then decreased as that center passed. This result was observed three times (corresponding to the 3 strips) followed by a sharp decrease toward zero. A similar result was seen along the *z*-axis; however, in this case the rising and falling of the response occurred as Strip 2 moved within Coil 2 and Compensating Coil 2. As expected, the *y*-axis testing demonstrated a gradual signal decrease with distance.

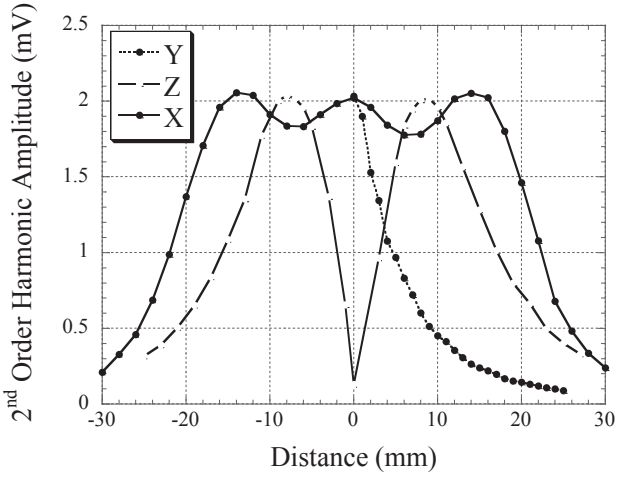

Figure 5.8 Response of sensor when incrementally moved along the *x*, *y*, and *z*-axes.

From **Figure 5.8**, it is evident that the location of the detection coils played a critical role in the accuracy of the system. In the experiment, the location of the sensor was fixed with respect to the detection/excitation coils. However, in practical use, the user may not be able to position the detection coils accurately. To ensure integrity of the measurement, the user will be able to move the coils around the sensor until the system picks up the maximum signal, indicating the correct orientation of the sensor. Alternatively, it is possible to place a calibration sensing strip, which can be parallel to the stress-responsive sensing strips but at a position that is insulated from force loading,

such that all measurement data is calibrated from the calibration sensing strip to eliminate the location effect.

5.4 Conclusion

The fabrication and testing of a wireless passive sensor system for monitoring the applied force on a hard surface has been presented. The sensor was tested from 0 to 226.89 N with experimental data demonstrating an exponential increase in the 2nd order harmonic amplitude of magnetoelastic sensing strips as pressure increased. It was demonstrated that neighboring strips have an interference effect which contributes to the overall sensor reading at a given coil. Additionally, a simple iterative algorithm was developed to determine the applied force on all sensing strips by examining the signals captured by the detection coils.

Future works include the design and fabrication of a more complicated sensor, which will include strips forming a sensing grid, and a more sophisticated algorithm to accommodate the more complex sensor structure. In addition, a new process, such as electroplating or screen printing, will be developed for fabrication of the sensing strips to reduce sensor-to-sensor variability.

Acknowledgements

The authors would like to acknowledge the financial support from the Department of Defense (DOD) of the Office of the Congressionally Directed Medical Research Programs (CDMRP), Grant DR081026 Hypothesis Development.

References

1. A. L. Window, Strain Gauge Technology, Springer, New York (1992).
2. R. L. Hannah and S. E. Reed, Strain Gauge User's Handbook, Springer, New York (1994).
3. M. C. Hsieh, Y. K. Fang, M. Ju, G. Chen, J. Ho, C. H. Yang, P. M. Wu, G. S. Wu, and T. Y. Chen, Journal of Microelectromechanical Systems 10, 121 (2001).
4. K. Tian, Z. Wang, M. Zhang, and L. Liu, IEEE Trans. Components and Packaging Technologies 32, 513 (2008).
5. K. I. Arshak, D. McDonagh, and M. A. Durcan, Sens. Actuators 79, 102 (2000).
6. S. A. Neild, M. S. Williams, and P. D. McFadden, Strain 41, 3 (2005).

7. D. Kuhunek and I. Zoric, IEEE Instrumentation and Measurement Technology Conference Proc. (2007), pp. 1–6.
8. Q. Shi, Z. Wang, L. Jin, Y. Li, H. Zhang, F. Lu, G. Kai, and X. Dong, IEEE Photonics Technology Letters 20, 1329 (2008).
9. Y. Huang, J. Tsai, and F. Lee, ICM2007 4th IEEE Int. Conf. Mechatronics (2007), pp. 1–6.
10. A. D. Kersey, M. A. Davis, H. J. Patrick, M. LeBlanc, K. P. Koo, C. G. Askins, M. A. Putnam, and E. J. Friebele, Journal of Lightwave Technology 15, 1442 (1997).
11. K. Arshak, E. Jafer, T. McGloughlin, T. Corbett, S. Chatzandroulis, and D. Goustouridis, IEEE Sensors 28 (2007).
12. A. Arshak, K. Arshak, D. Waldron, D. Morris, O. Korostynska, E. Jafer, and G. Lyon, Medical Engineering and Physics 27, 347 (2005).
13. J. Zhai, T. V. How, and B. Hon, CIRP Annals-Manufacturing Technology 59, 187 (2010).
14. M. Nabipoor and B. Y. Majlis, J. Phys.: Conference Series 34, 770 (2006).
15. C. A. Grimes, C. S. Mungle, K. Zeng, M. K. Jain, W. R. Dreschel, M. Paulose, and K. G. Ong, Sensors 2, 294 (2002).
16. D. Kouzoudis and C. A. Grimes, Smart Mater. Struct. 9, 1 (2000).
17. D. Kouzoudis and D. E. Mouzakis, Sens. Actuators A 127, 355 (2006).
18. E. L. Tan, B. D. Pereles, and K. G. Ong, IEEE Sens. J. 10, 1085 (2010).
19. K. G. Ong and C. A. Grimes, Sens. Actuators A 101, 49 (2002).
20. J. D. Livingston, Phys. Stat. Sol. 70, 591 (1982).

Chapter 6 A Wireless Passive Magnetoelastic Force Mapping System for Biomedical Applications

Brandon D. Pereles, Andrew J. DeRouin, Keat Ghee Ong*
Department of Biomedical Engineering, Michigan Technological University
1400 Townsend Drive, Houghton, MI 49931, USA.

Abstract

A wireless, passive force–mapping system based on changes in magnetic permeability of soft, amorphous Metglas 2826MB strips is presented for long-term force/stress monitoring on biomedical devices. The presented technology is demonstrated for use in lower limb prosthetics to ensure proper postoperative fitting by providing real-time monitoring of the force distribution at the body-prosthesis interface. The sensor system consisted of a force-sensitive magnetoelastic sensing strip array that monitored applied loading as an observed change in the peak amplitude of the measured magnetic higher-order harmonic signal of each array element. The change in higher-order harmonic signal is caused by[3] the change in the magnetic permeability of the sensing strips that corresponds to an increase in strip magnetization. After loading, the measured higher-order harmonic signals were fed into an algorithm to determine the applied forces, allowing for determination of the real-time loading profile at the body prosthesis interface. [DOI: 10.1115/1.4025880]

Keywords: magnetoelastic materials, magnetic harmonic fields, sensor array, lower limb prosthesis, force sensor

6.1 Introduction

[3]"The material in this chapter was previously published in the *Journal of Biomechanical Engineering*."
Pereles, B.D., DeRouin, A.J., and Ghee Ong, K., *A Wireless, Passive Magnetoelastic Force–Mapping System for Biomedical Applications.* Journal of Biomechanical Engineering, 2013. **136**(1): p. 011010-011010. Published originally by ASME.

A major concern for amputees with prosthetics is pressure induced ulceration at the residuum (stump). A variety of hypotheses exist to explain pressure ulcers, such as long-term compression of tissue resulting in blood-flow occlusion and tissue ischemia or inhibition of the lymphatic system preventing the removal of harmful toxins and waste products [1]. When ulceration occurs, the effects can range from minor skin irritation to tissue death [2]. In all of these instances, patients may be required to stop using their prosthetic until their tissue has healed, significantly interfering with daily activities [3]. As a result, the design of the prosthetic, in terms of load bearing and sleeve/liner selection, plays a critical role in maintaining patient health.

The first preventative measure against pressure ulceration is a properly fit and designed prosthetic. In order to accomplish this, technologies capable of providing quantitative analysis of force distribution during the fitting process have been developed. For instance, the Rincoe Socket Fitting System, Tekscan F-Socket Pressure Measurement System, and the Novel Pliance 16P System are all commercially available pressure-mapping systems aimed at ensuring a properly fit prosthetic by providing quantitative information on the force distribution between the patient stump and prosthetic [4]. The Tekscan F-Socket and the Rincoe Socket Fitalso been developed to maintain force distribution and fit. For instance, a prosthetic capable of changing volume and hardness was developed to account for changes in stump volume and misalignment issues [8]. The system incorporates bags filled with magnetorheological fluid into the prosthetic. Hardness is altered as a result of changes in fluid viscosity in response to an external magnetic field, while volume can be controlled by inserting or removing the magnetorheological fluid. However, while the device was reported to function better than a total surface bearing (TSB) socket in a single patient trial, this system represents a major redesign of current socket systems [8].

With a properly fit prosthetic, the challenge then becomes maintaining proper force distribution and fit. To that end, common practices, such as using prosthetic sleeves and liners, have been reported to improve suspension and comfort [6], but their

effectiveness in terms of prevention of ulceration and other related issues is mixed [7]. In addition, a variety of smart prosthetics have also been developed to maintain force distribution and fit. For instance, a prosthetic capable of changing volume and hardness was developed to account for changes in stump volume and misalignment issues [8]. The system incorporates bags filled with magnetorheological fluid into the prosthetic. Hardness is altered as a result of changes in fluid viscosity in response to an external magnetic field, while volume can be controlled by inserting or removing the magnetorheological fluid. However, while the device was reported to function better than a total surface bearing (TSB) socket in a single patient trial, this system represents a major redesign of current socket systems [8].

These preventative systems and technologies are, unfortunately, still only preventative and typically lack capacity for long-term monitoring and identification of the conditions that will lead to ulceration. Some technologies have been deployed to meet this need. For instance, a sensor system for wireless, long-term continuous monitoring of forces on lower-limb prosthesis utilized a commercial transducer attached to a custom leg prosthesis. The system was reported for wireless use up to 700 m outdoors and was capable of monitoring experienced forces along the relative x, y, and z axis in addition to the moments acting on the prosthesis during a variety of activities [9]. However, in addition to requiring significant modifications to existing prosthetics, the system did not collect data directly at the socket-stump interface and instead monitored from the shaft portion of the prosthetic [9]. Another long-term monitoring system utilized parallel plate capacitors comprised of drive and sense electrodes patterned onto printed circuit boards. The plates were separated by a 2×2 array of pillars [9]. When a compressive or shear force was applied to the sensor, the relative position of the plates changed, altering the measured capacitance. The sensitivity and range of the sensor could be controlled by altering the overall size of the device and the dimensions of the pillars [10]. While this device could be simplistically deployed in a prosthetic sleeve, the fabrication method was complex and the sensor was neither wireless nor passive.

Pereles, B.D., DeRouin, A.J., and Ghee Ong, K., *A Wireless, Passive Magnetoelastic Force–Mapping System for Biomedical Applications.* Journal of Biomechanical Engineering, 2013. **136**(1): p. 011010-011010. Published originally by ASME.

The developed system is presented here for deployment on lower-limb prosthetics as a multipoint force-mapping system. The experienced force on the residuum can be more accurately observed by monitoring force at multiple points, allowing for better identification of those conditions that might lead to tissue damage and confirmation of a proper prosthetic fit. The wireless nature of this sensor technology allows for a convenient and effective means to measure the force distribution at a device interface, and since the sensor is passive, there are no battery lifetime issues. In addition, the sensor itself is a thin layer of magnetic material that can easily be deployed on or in a biomedical device without compromising mechanical integrity or requiring major modifications to existing designs. The application of the magnetoelastic force–monitoring system was demonstrated on an Otto Bock Titan lower-limb prosthesis donated by Northern Orthotics & Prosthetics Inc. (Houghton, MI). The metallic bottom portion of the lower-limb prosthetic, shown in **Figure 6.1**, was identified as a desirable location for deploying the force sensors, since the sensor would still experience forces from the stump socket interface while illustrating the ease with which the system can be deployed to an already existing system. After deploying the sensor, each array element, measuring 37.54 mm × 3.58 mm × 23 μm, was loaded. As illustrated in **Figure 6.2**, each strip was capable of monitoring multiple loads by treating the front and back halves of each sensing strip as separate load regions and assuming that the captured response, when monitoring from either end, was only from the region closest to the detection coil. Using external detection coils, the observed changes in the amplitude of the magnetic higher-order harmonic fields, caused by the applied loading, were remotely monitored and fed into a computer for analysis. A relationship was then empirically found between the captured second-order harmonic amplitude associated with each loading area and the applied force to those regions. Based on this relationship, an algorithm was developed to appropriately identify the load in each region.

Pereles, B.D., DeRouin, A.J., and Ghee Ong, K., *A Wireless, Passive Magnetoelastic Force–Mapping System for Biomedical Applications.* Journal of Biomechanical Engineering, 2013. **136**(1): p. 011010-011010. Published originally by ASME.

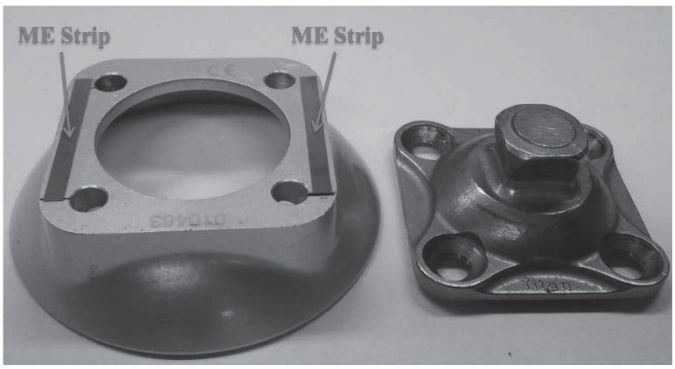

Figure 6.1 The sensor deployed on an Otto Bock lower limb Prosthetic.

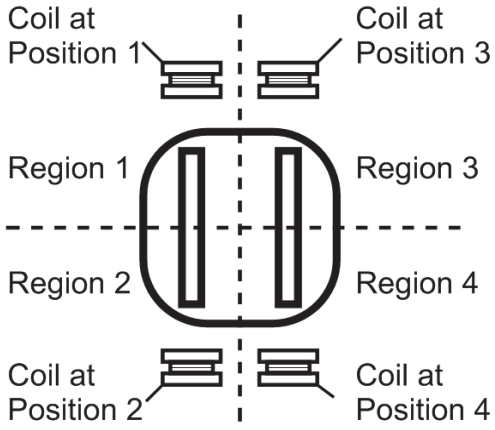

Figure 6.2 Illustration of the sensor strip placement and the location of the regions and monitoring positions where "region" refers to the location of force application

6.2 Experiments

To excite and capture the second-order harmonic amplitude of the sensing strips, an ac/dc excitation system, consisting of a Fluke 271 10-MHz function generator, an ac amplifier (Tapco Juice), a Kepco bipolar power supply, and an Agilent spectrum/ network analyzer 4936B was used (see **Figure 6.3**). Additionally, the detection coil used to capture the sensor response was 3.3 cm in diameter with 200 turns of 28-gauge wire, while the excitation coil used to excite the sensor was 27.6 cm in diameter with 50 turns of 18-gauge wire. During experiments, the sensor was placed within the mechanical

loader such that the sensing strip was centered on one of the detection coils within 60.5 mm. The function generator was then set to produce a 500-A/m, 200-Hz ac excitation signal while the dc power supply excited the sensor with a 280-A/m field. The second-order harmonic was measured by the spectrum analyzer at 400 Hz.

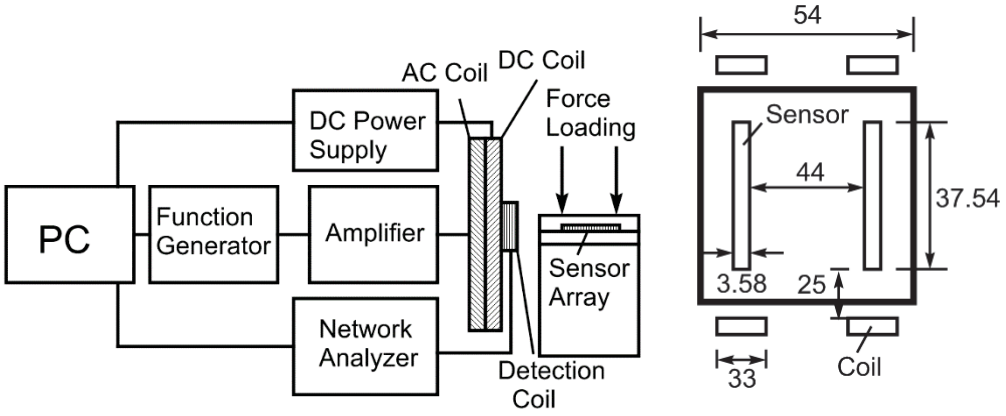

Figure 6.3 (a) The experimental setup consisting of ac/dc excitation coils, function generator, ac amplifier, power supply, spectrum network analyzer, and control box. (b) The dimensions (mm) and locations of the sensors and coils.

As illustrated in **Figure 6.2**, the four sensing regions were named as region 1 (R1), region 2 (R2), region 3 (R3), and region 4 (R4). In the first set of experiments, the detection coils were placed next to R1 and R3. In terms of loading the sensors, R1 and R3 were exposed to a changing load from 0.044kN to 0.133kN at 0.022kN intervals, while constant loads were held on R2 and R4. After completing each loading cycle at R1 and R3, the constant loads at R2 and R4 were increased at an interval of 0.022kN, and the process was repeated until the constant loads reached 0.133kN (see **Figure 6.4**). After performing each load cycle on R1 and R3 with different constant loads held on R2 and R4, the experiment was repeated, this time holding R1 and R3 constant and varying the applied loading on R2 and R4. Once this process was finished, the detection coils were placed next to R2 and R4 and the procedure was repeated.

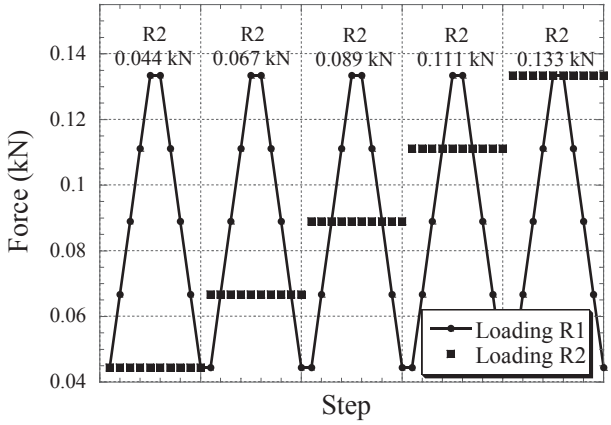

Figure 6.4 Plot illustrating the loading procedure in which a changing load is applied to R1 while a constant load, changed between load cycles, is held on R2.

6.3 Results and Discussion

The effects of loading the sensor in this manner are plotted in **Figures 6.5(a)** and **6.5(b)**. Loading at R1 and R3 resulted in an increase in the observed higher-order harmonic fields, while loading at R2 and R4 caused an observed decrease in the overall sensor response. These effects were further illustrated when repeating the same experiments while monitoring from R2 and R4 (see **Figures 6.6(a)** and **6.6(b)**).

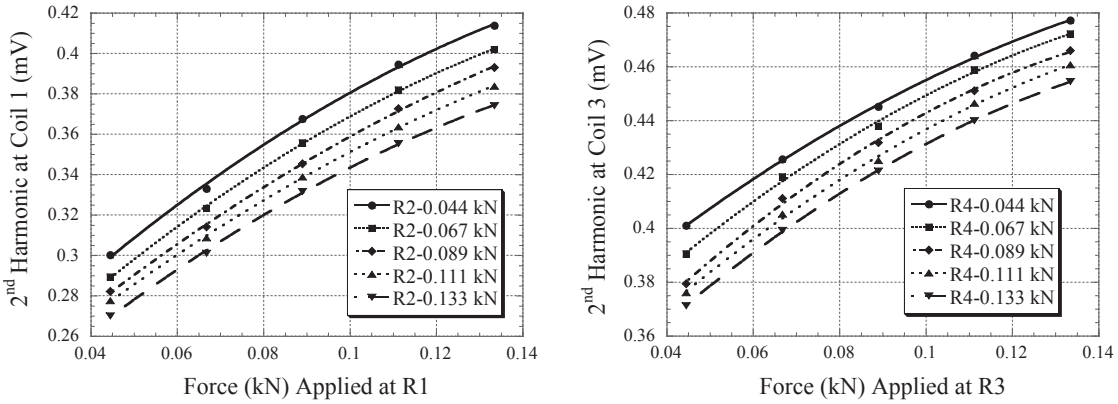

Pereles, B.D., DeRouin, A.J., and Ghee Ong, K., *A Wireless, Passive Magnetoelastic Force–Mapping System for Biomedical Applications.* Journal of Biomechanical Engineering, 2013. **136**(1): p. 011010-011010. Published originally by ASME.

(a) (b)

Figure 6.5 An increasing sensor response was observed while monitoring from (a) coil 1 and (b) coil 3 with a changing load applied to R1 and R3 and constant loading applied to R2 and R4.

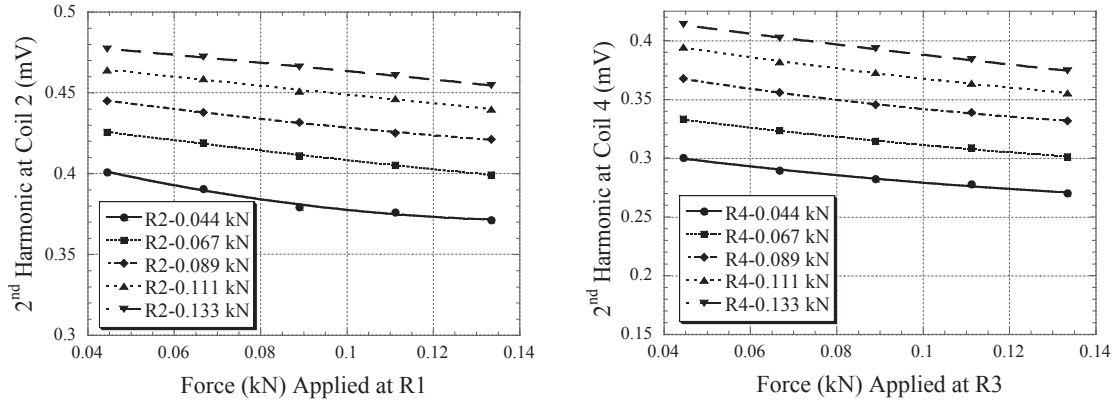

(a) (b)

Figure 6.6 A decreasing sensor response was observed while monitoring from (a) coil 2 and (b) coil 4 with a changing load applied to R1 and R3 and constant loading applied to R2 and R4.

A clear observation from **Figures 6.5** and **6.6** is that the location of force loading produced different sensor responses when monitored from different positions. For example, increasing force loading on R1 caused an increase in harmonic amplitude when monitored from R1 (see **Figure 6.5(a)**), but the same force loading caused a slight decrease in harmonic amplitude when monitored from R2 (see **Figure 6.6(a)**), even though R1 and R2 are on the same strip. This can be explained by the relationship between applied stress and magnetic permeability. As a result of Metglas 2826MB's positive magnetostriction, the effect of applied loading normal to the surface of the sensing strips increases magnetic permeability. When differing loads are applied to separate regions of the strip, the material, in essence, experiences a non-uniform change in magnetic permeability. The magnetic field monitored from either end of each strip will then increase or decrease depending on the loading of both regions. This is illustrated in **Figure 6.5**, where the sensor response is monitored from R1 and R3 and a changing load is applied. Since the loading applied to R2 and R4 only changes between loading cycles,

the effect is an increase in amplitude during load testing as the magnetic permeability at R1 and R3 increases. However, a change in the applied loading at R2 and R4 results in an overall decrease in sensor response as the internal magnetization of the strips shifts toward R2 and R4. A similar effect is observed in **Figure 6.6** when the same experiment is monitored from R2 and R4, where the constant loading was applied. In this testing, the increasing permeability of R1 and R3 leads to a decreasing observed response during load cycles with an increasing overall sensor response with changing constant loads at R2 and R4.

Using the collected data, an algorithm was empirically developed to determine applied loading in all regions. **Figures 6.5** and **6.6** were first curve-fitted with decaying exponential equations,

$$S_i = A_i(1 - e^{-B_i f_i}) + C_i \qquad (1)$$

where S is the sensor response, A is the peak amplitude, B is the slope of the curve, C is the y-intercept of the curve, f is the applied force, and i is the region being loaded. After performing this curve fitting, it was determined that the values of A and B were nearly constant between curve fits, while the value of C was affected from loading on the opposing region of each strip. The dependency of C towards force loading at the opposite region can be described with

$$C_i = a_i\left(1 - e^{-b_i f_{(3-i)}}\right) + c_i \qquad i < 3 \qquad (2a)$$

$$C_i = a_i\left(1 - e^{-b_i f_{(7-i)}}\right) + c_i \qquad i > 2 \qquad (2b)$$

Coefficient values for A, B, a, b, and c were then determined empirically from curves in **Figures 6.5** and **6.6**, completing the algorithm.

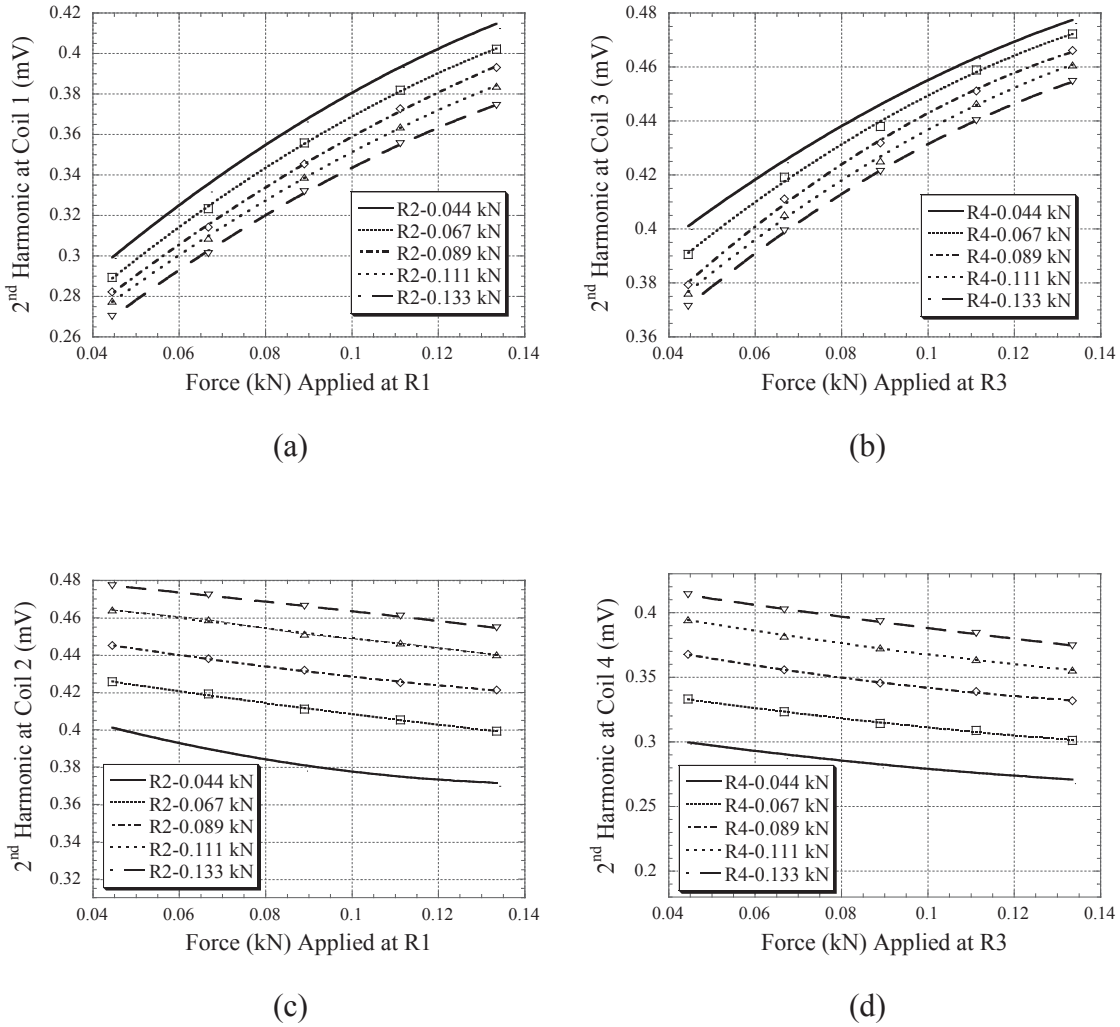

Figure 6.7 The raw sensor data was recalculated using the developed algorithm for testing, where a changing load was applied to R1 and R3 and a constant load was held on R2 and R4 when monitoring from (a) coil 1, (b) coil 3, (c) coil 2, and (d) coil 4.

To determine force loading (f_i) from the measurements (S_i), the algorithm used an iterative process. As an illustration, to determine f_1 and f_2, the algorithm first started with R1 (i=1) and set an initial value for f_2 (e.g., f_2 =0) in Eq. (2a) to solve for C_2. The calculated C_2 was then plugged into Eq. (1) to solve for a predicted f_2. The calculated f_2 was then used in Eq. (2b) to solve for C_1, which was then substituted into Eq. (1) to solve for a new f_1. This process was repeated until the calculated values for the expected forces

and coefficients satisfied Eqs. (1) and (2) within an acceptable error. Using this method, the algorithm was used to recalculate the raw sensor response with a<1% maximum error (see **Figures 6.7(a)–6.7(d)**). Additionally, the maximum error of calculating the expected forces from sensor data was determined as less than 7% (see **Figures 6.8(a)–6.8(d)**). To reduce this error in future works, more rigorous calibrations and higher-resolution solving methods will be developed. Additionally, while the sensor illustrated little drift when loaded cyclically, the effects of changing position in relation to the detection coils on sensor response will need to be accounted for, as previous work has demonstrated that position does have an effect on the magnitude of sensor response [11]. To account for this, it is necessary for the sensors and coils to be properly aligned prior to use by adjusting the coils on unloaded sensors until receiving the expected signals. An alternative technique is to develop a calibration algorithm using another non-loaded sensor strip as a force-independent input parameter.

Figure 6.9 plots the change in measured harmonic amplitude at R1 when R1 was cyclically loaded from 0.044 kN to 0.133 kN. The sensor illustrated little drift when loaded cyclically. To characterize the stability of the sensor when under repetitive and changing loads at both ends of the sensor strip, the response at R1 and R3 was also monitored while force loading was cycled at R1 and R3 from 0.044 kN to 0.133 kN (five measurements were taken at each force loading) while force loading at R2 and R4 was held constant. Force loading at R2 and R4 was then increased at an interval of 0.022 kN after completion of each cycle at R1 and R3. **Figure 6.10** illustrates that the sensor response showed symmetric "stepped pyramids," indicating low hysteresis and drift. There is also a consistent decrease in amplitude for each stepped pyramid, indicating that increased loading at R2 and R4 decreased the sensor signal when measured at R1 and R3. This is consistent with observations in **Figure 6.5**.

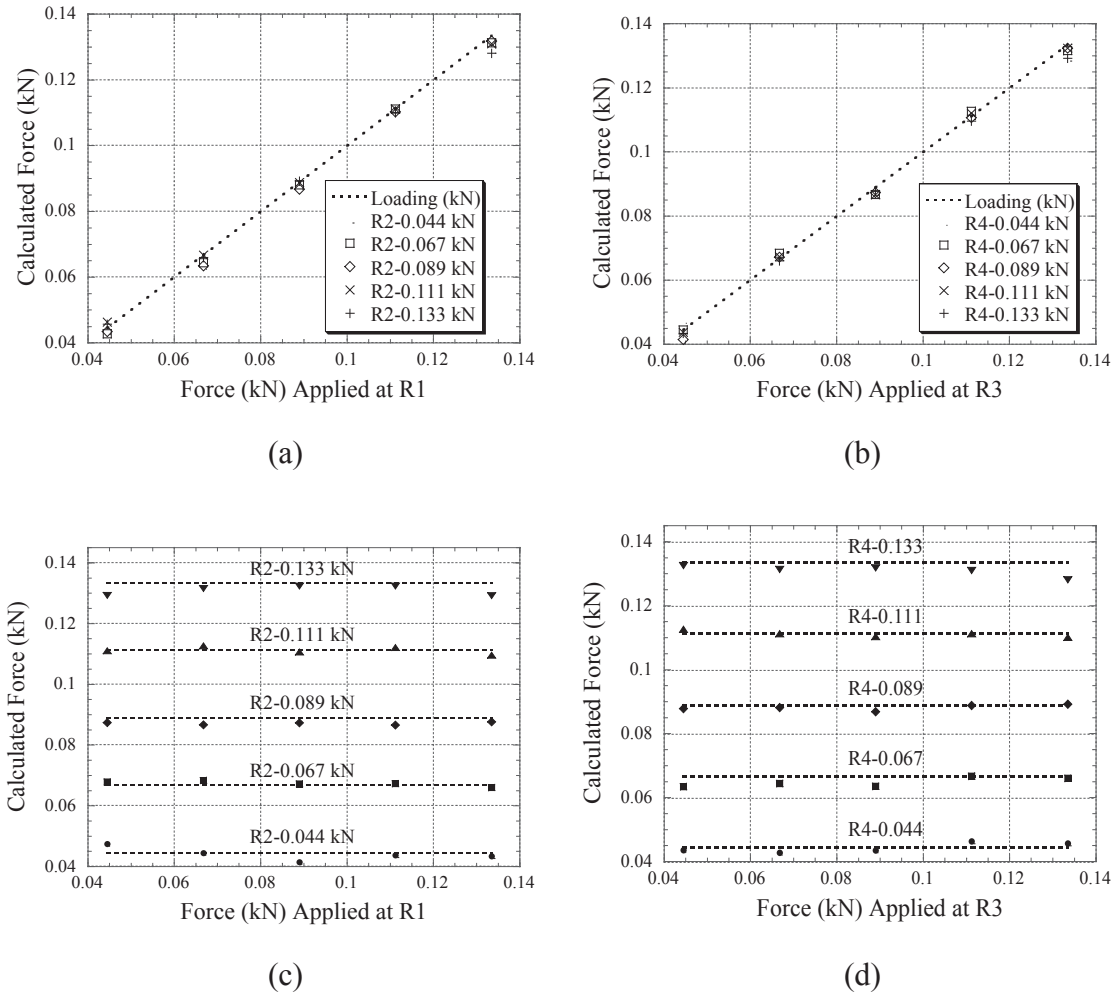

Figure 6.8 The applied loading was recalculated using the developed algorithm for testing, where a changing load was applied to R1 and R3 and a constant load was held on R2 and R4 when monitoring from (a) coil 1, (b) coil 3, (c) coil 2, and (d) coil 4.

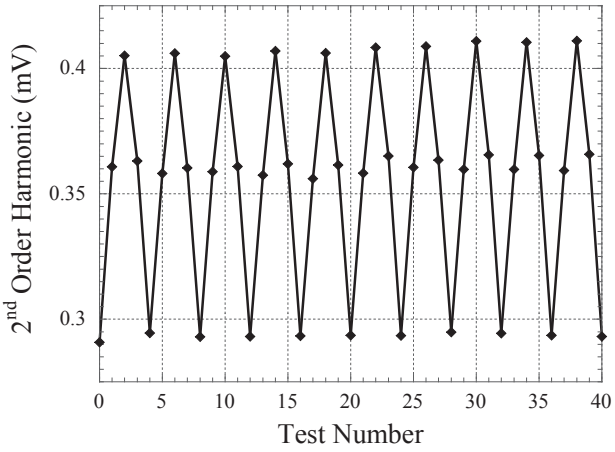

Figure 6.9 Cyclic loading of the sensor was performed from 0.044 kN to 0.133 kN over the course of ten loading cycles with results illustrating low drift in sensor response.

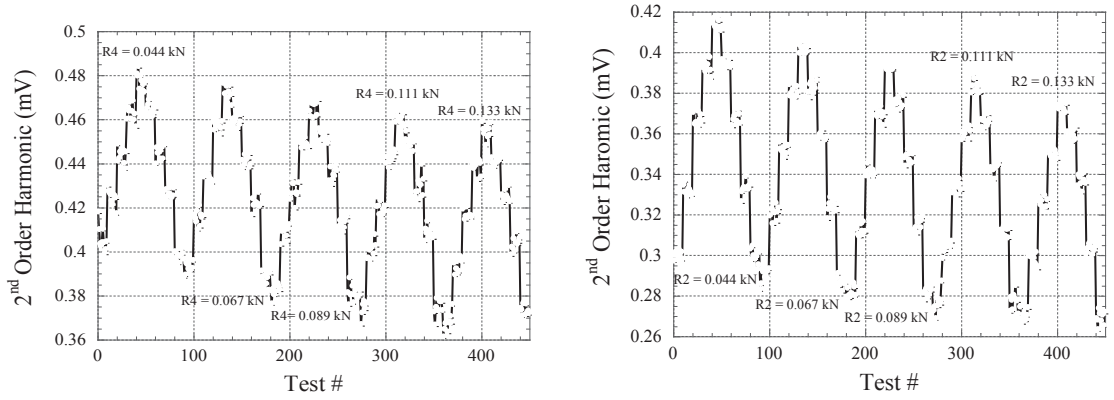

Figure 6.10 Stability testing of the sensor while applying a changing load from 0.044 kN to 0.133 kN at (a) R1 and (b) R3 with constant loads, changed at 0.022kN intervals between load cycles, held on R2 and R4. The sensor responses were monitored from coil 1 and coil 3 and illustrated stepped pyramid responses with low hysteresis and drift.

6.4 Conclusion

A wireless, passive sensor system capable of mapping the force on biomedical devices was developed. The proposed system was constructed with custom rectangular magnetoelastic sensing strips capable of measuring applied forces on two quadrants of a

single strip simultaneously. In order to illustrate the ease with which the sensor system can be deployed, the sensor was adhered to the lower portion of a prosthetic.

These advances are important due to the lack of wireless, long term monitoring systems available to medical staff to diagnose force-related device malfunctions and failures. Overall, this device could drastically improve the quality of care for patients implantable device and assist in the further development of better implants and devices, such as prosthetics, by contributing to the understanding of the dynamic loads that biomedical devices experience.

Future works will focus on developments toward full in vivo testing, as illustrated in **Figure 6.11**. Specifically, a process for fabricating more consistent sensor arrays, as opposed to the current shearing method, along with electronics capable of being attached to existing prosthetics will be pursued. Additionally, while the presented algorithm is fully functional, improvements will be necessary when the array is expanded to include more strips. Moreover, the current detection system connects directly to a personal computer (PC) for data processing and storage, and in the future, portable battery units, memory storage, and wireless data transmission to the PC will be incorporated into the system to develop a truly portable sensing platform.

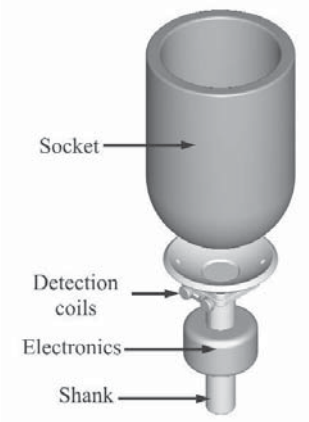

Figure 6.11 Illustration of the implementation of the stress/force monitoring system. To wirelessly monitor responses of the sensors, the system will feature attached electronics, including a power supply, excitation circuitry, and transceiver for wireless data transmission. The excitation/detection coils will be attached to the prosthetic, with the sensing strips sandwiched in between the coupler that connects the shank to the socket.

Pereles, B.D., DeRouin, A.J., and Ghee Ong, K., *A Wireless, Passive Magnetoelastic Force–Mapping System for Biomedical Applications.* Journal of Biomechanical Engineering, 2013. **136**(1): p. 011010-011010. Published originally by ASME.

Acknowledgements

The authors would like to acknowledge Northern Orthotics & Prosthetics Inc. for their contributions to this work. This research was conducted in part with support under and awarded by Department of Defense, Air Force Office of Scientific Research, National Defense Science and Engineering Graduate (NDSEG) Fellowship, 32 CFR 168a, and the Department of Defense of the Office of the Congressionally Directed Medical Research Programs, Grant DR081026 Hypothesis Development.

Nomenclature

A = peak amplitude

B = slope of the curve

C = y-intercept of curve

f = applied force

i = region being loaded

S = sensor response

References

1. Mak, A. F., Zhang, M., and Tam, E. W. C., 2010, "Biomechanics of Pressure Ulcer in Body Tissues Interacting With External Forces During Locomotion," Annu. Rev. Biomed. Eng., 12(1), pp. 29–53.
2. Gailey, R., Allen, K., Castles, J., Kucharik, K., and Roeder, M., 2008, "Review of Secondary Physical Conditions Associated With Lower-Limb Amputation and Long-Term Prosthesis Use," J. Rehabil. Res. Dev., 45(1), pp. 15–29.
3. Salawu, C., Middleton, A., Gilbertson, A., Kodavali, K., and Neumann, V., 2006, "Stump Ulcers and Continued Prosthetic Limb Use," Prosthet. Orthot. Int., 30(3), pp. 279–285.
4. Mak, A. F., Zhang, M., and Boone, D. A., 2001, "State-Of-The-Art Research in Lower-Limb Prosthetic Biomechanics-Socket Interface: A Review," J. Rehabil. Res. Dev., 38(2), pp. 161–174.
5. Polliack, A. A., Craig, D. D., Sieh, R. C., Landsberger, S., and McNeal, D. R., 2002, "Laboratory and Clinical Tests of a Prototype Pressure Sensor for Clinical Assessment of Prosthetic Socket Fit," Prosthet. Orthot. Int., 26(1), pp. 23–34.

Pereles, B.D., DeRouin, A.J., and Ghee Ong, K., *A Wireless, Passive Magnetoelastic Force–Mapping System for Biomedical Applications.* Journal of Biomechanical Engineering, 2013. **136**(1): p. 011010-011010. Published originally by ASME.

6. Baars, E. C. T., and Geertzen, J. H. B., 2005, "Literature Review of the Possible Advantages of Silicon Liner Socket Use in Trans-Tibial Prostheses," Prosthet. Orthot. Int., 29(1), pp. 27–37.
7. Meulenbelt, H. E. J., Dijkstra, P. U., Jonkman, M. F., and Geertzen, J. H. B., 2006, "Skin Problems in Lower Limb Amputees: A Systematic Review," Disabil. Rehabil., 28(10), pp. 603–608.
8. Ogawa, G., Obinata, K., Hase, K., Dutta, A., and Nakagawa, M., 2008, "Design of Lower Limb Prosthesis With Contact Pressure Adjustment by MR Fluid," Conf. Proc. IEEE Eng. Med. Biol. Soc., 2008, pp. 330–333.
9. Frossard, L., Beck, J., Dillon, M., and Evans, J., 2003, "Development and Preliminary Testing of a Device for the Direct Measurement of Forces and Moments in the Prosthetic Limb of Transfemoral Amputees During Activities of Daily Living," J. Prosthet. Orthot., 15(4), pp. 135–142.
10. Sundara-Rajan, K., Bestick, A., Rowe, G. I., Klute, G. K., Ledoux, W. R., Wang, H. C., and Mamishev, A. V., 2012, "An Interfacial Stress Sensor for Biomechanical Applications," Meas. Sci. Technol., 23(8), p. 085701.
11. Pereles, B. D., DeRouin, A. J., Dienhart, T. A., Tan, E. L., and Ong, K. G., 2012, "A Wireless, Magnetoelastic-Based Sensor Array for Force Monitoring on a Hard Surface," Sens. Lett., 10(3-4), pp. 806–813.

Chapter 7 Future Works

Chapter Overview

The focus of this chapter is to present future work on the magnetoelastic resonance technology. Immediate tasks include further validation of the theoretical work, as well as refinement of the sensor design. Additionally, analysis of the effects of applied loading on the sensor's magnetic properties shall be pursued. Moreover, expansion of the ANSYS model as well incorporation of higher-order harmonic resonance modes into the developed sensor technology should be investigated.

7.1 Surface Contact Characterization

To further evaluate the theory presented in Chapter 2, analysis of the actual surface conditions at the contact interface can be investigated. Specifically, atomic force microscopy and/or scanning electron microscopy can be used to determine physical properties of the materials, such as the surface roughness, for more quantitative analysis of the interface contact mechanics. Additionally, the impact of the surface roughness at the interface between the load applicator and the sensor strip, as well as between the sensor frame and the load applicator, could be investigated. The effect of surface roughness was investigated by changing which side of the sensor strip (each sensor strip has a rough side and a smooth side) was in contact with the load applicator and the smooth sensing frame. This testing illustrated a minimal effect on sensor response when the roughness of the load applicator is similar to the sensor frame (see **Figure 7.1a**), while a significant difference was observed when the load applicator is rougher than the sensor frame (see **Figure 7.1b**). This results from the fact that when both the sensor frame and load applicator are smooth, there will always be a smooth to smooth and a smooth to rough interface on either side of the sensing strip, regardless of its orientation. On the other hand, when the load applicator is roughened, there will either be a smooth to smooth and a rough to rough or a smooth to rough and a rough to smooth interface on either side of the strip, depending on its orientation.

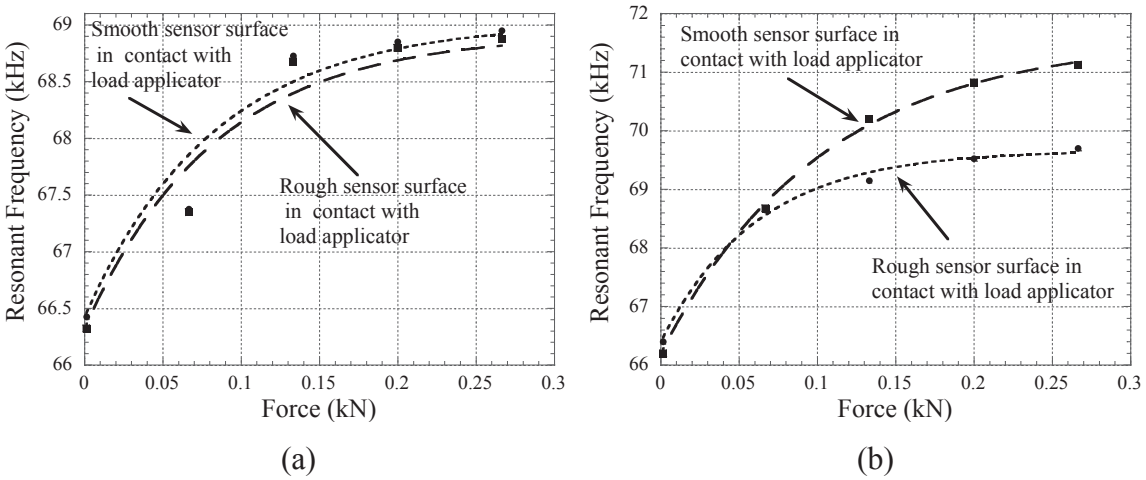

Figure 7.1 The effect of changing which side of the sensor strip was in contact with (a) a smooth applicator head and (b) a roughened applicator. During both tests the sensor frame remained smooth.

7.2 Improving Applicator Design

To further improve the magnetoelastic sensor technology, modifications to the applicator design can be investigated. For instance, to improve the ability of the sensor to handle non-normal and non-centered loading, the applicator can be modified to mimic commercially available load cells which make use of button designs for the load applicator. This design allows the sensing element to primarily experience a normal load even when the applied loading is at an angle and/or not centered. In addition to this, the effectiveness of the current load sharing configuration can be further evaluated to either validate the current design or identify improvements. Furthermore, changes to the material comprising the applicator can be investigated. Specifically, in terms of materials and fabrication methods, the presented work focused on the use of polycarbonate and a table top CNC Micro Milling Machine. By exploring other fabrication procedures such as injection molding, a variety of other materials can be tested.

7.3 Magnetic Evaluation of the Sensor Technology

Further analysis of the resonance sensor's magnetic properties can be investigated as part of future works. For instance, according to the Villari effect, an applied stress to a magnetoelastic material results in a change in the material's permeability. Theoretically, the developed resonance sensor may be responding to an applied load with an increase in

resonant frequency due to a change in material permeability. Preliminary testing has already been performed and can be seen in **Figure 7.2**. In this testing, the 2nd order harmonic amplitude of the sensor under an applied 200 Hz AC magnetic field was observed at different applied loads. The results indicate that a change in permeability is may be occurring with applied loading; however, the extent to which this theoretical change in permeability actually affects the resonant frequency would need to be further investigated.

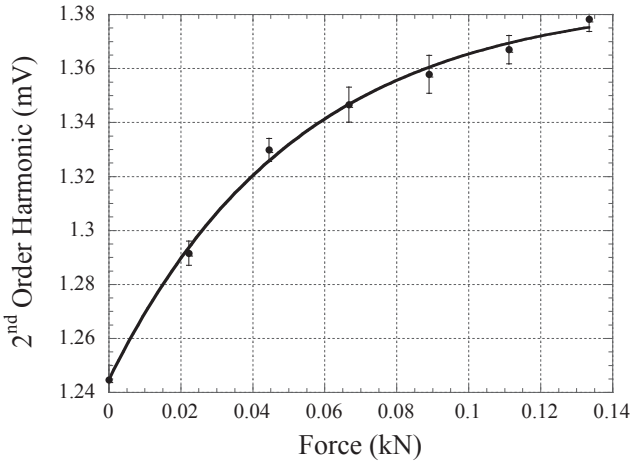

Figure 7.2 The change in amplitude of the 2nd order harmonic of a 30.5 mm long sensing strip was monitored while loaded from 0 N to 133 N at 22 N intervals to analyze the effect of applied loading on sensor permeability.

7.4 Evaluating DC Field and Temperature Dependence

The literature reports several methods for ensuring or calibrating a resonating magnetoelastic sensor's response to account for changes in the applied DC biasing field and/or the experienced temperature. Previous work shows that adjusting the DC field can make the sensor temperature independent. Shifts in the higher order harmonics can only occur in the presence of an additional DC field source, thus allowing for a calibration of the sensing system [1]. However, as **Figure 7.2** demonstrates, large loads shift the higher harmonics, thus preventing this method from being used to calibrate the sensor [1]. Additionally, while other methods for removing the DC field and temperature

dependence of this technology have been reported [2], they function under the traditional assumptions previously discussed and, as a result, may also not be suitable to the developed technology.

7.5 Expanding the ANSYS Model

While simplistic analysis using ANSYS was performed, future works will include the development of a more complex ANSY model. In particular, future models will incorporate an actual load applicator and the sensor frame into the model. However, in order to accomplish this, certain properties, such as the friction between the sensing strips and applicators, will need to be determined empirically.

7.6 Further Study of Higher-Order Harmonic Resonances

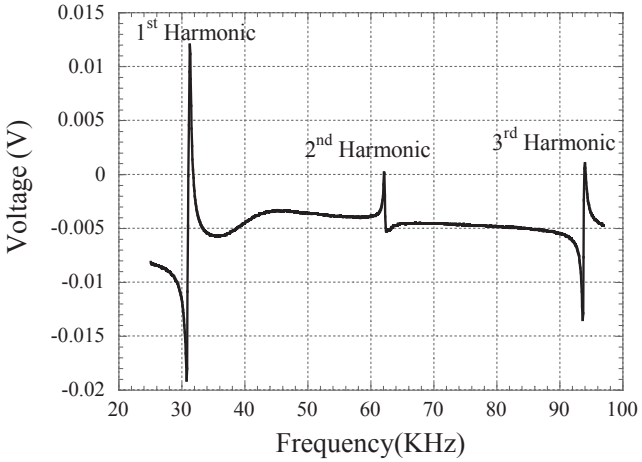

Figure 7.3 A 71.0 mm long sensing strip was observed from 0.0 kHz to 100 kHz in order to capture the 1st, 2nd and 3rd order harmonic.

In addition to the 1st, or fundamental, harmonic resonance exhibited by a resonating magnetoelastic sensor, higher-order harmonic resonances also occur at multiples of the fundamental resonant frequency, as can be seen in **Figure 7.3** which demonstrates the 1st, 2nd and 3rd harmonic of a 71.0 mm long resonating strip. Specifically, a resonating strip will have a number of nodes equal to its resonant mode

(whole number multiple of the fundamental resonant frequency) and these nodes will be positioned according to [3]:

$$x = \frac{L}{2n(2m-1)} \tag{1}$$

where x is the location along the length of the strip, L is the length of the strip, n is the harmonic number and m is a whole number between 1 and n representing each node for a given harmonic resonance n. In theory, a sensor array consisting of multiple strips of the same length, monitored using a single external detection source, could be realized by loading the higher order nodes such that the application of a load results in an increase in the desired harmonic resonance n while damping out the other resonant peaks. This principle is illustrated in **Figure 7.4a** which shows the resonance spectrum of a seven element array. **Figure 7.4a** is designed such that such that the varying line styles correspond to the 1st and 2nd mode of a 65.5 mm, 55.7 mm and 48.0 mm strip respectively. As can be seen in **Figure 7.4b**, the application of a load to the node corresponding to the 2nd mode of these strips dampens the 1st order response.

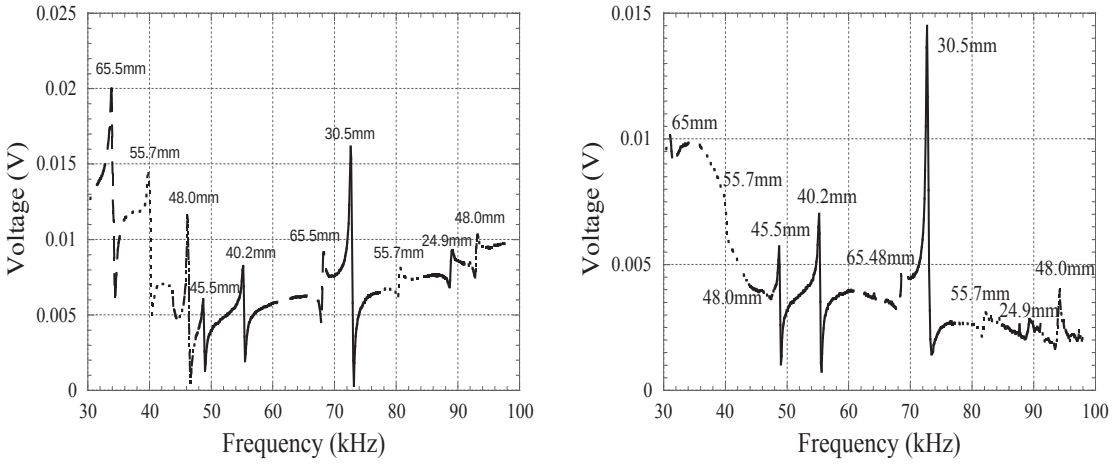

Figure 7.4 The (a) unloaded and (b) loaded response of a of a seven strip sensing array was captured in order to illustrate that loads applied at the higher order nodes will damp out other resonant peaks.

Additionally, to further evaluate and demonstrate the possibility of incorporating sensing elements loaded at the higher order nodes, a 55.0 mm and 71.0 mm long strip

were analyzed by loading at the nodes of the 2nd and 3rd harmonic resonant peaks, see **Figure 7.5a-b**. The results indicate a clear increase in resonant frequency with applied loading, thus demonstrating the feasibility of using loading at higher order nodes in future designs.

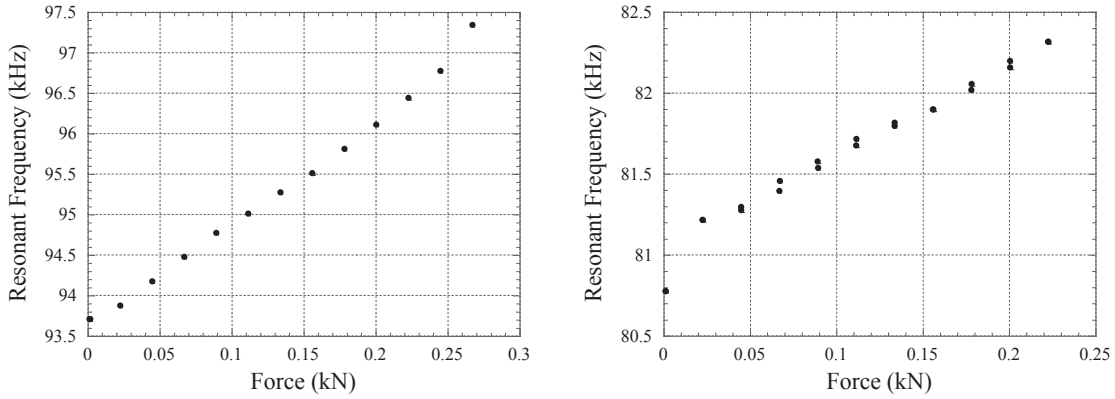

(a) (b)

Figure 7.5 Load testing was performed on a (a) 55.0 mm and (b) 71.0 mm long sensing strip at the 2nd and 3rd order nodes, respectively. Results demonstrate a clear increase in resonant frequency with applied loading.

7.7 Further Non-Uniform Loading Investigation

The theory presented in Chapter 2 explains why an applied loading at the nodes of a resonating strip results in an increase in resonant frequency. However, the presented theory is not sufficient to explain how changing the location of an applied load, at low forces, along the length of the strip would result in an increased sensitivity, as per the work presented in Chapter 4. It is reported in the literature that if a non-uniform mass is applied at a position along the length of a resonating strip, an imbalance between the acoustic wave velocities on either side of the node occurs. As a result, the position of the node shifts toward the side of the sensor with the mass load, resulting in a reported increase in resonant frequency [4]. Further investigations into the effects of non-uniform mass loading on the resonant sensor response may allow for a deeper and more robust understanding of the impact of non-uniform loads on the developed sensor system.

7.8 Determining System Specifications

Sensor specifications such as sensitivity, dynamic range, and hysteresis will need to be comparable or better to currently available systems. For instance, for commercial applications, the Rincoe Socket Fitting System described in Chapter 1 makes use of force sensing elements each with a resolution of 3.45 kPa, a full scale output of 83 kPa, and a maximum sampling rate of 100 Hz [5]. The F-Socket describes in Chapter 1 has a reported 165 Hz sampling rate with a full scale out of 700 kPa [5]. In terms of systems designed for research, a system for monitoring interface mechanics at the stump socket interface was developed by the Musculoskeletal Biomechanics Laboratory at Tel Aviv University, Israel and Sensor Products Co. (NJ, USA). The mapping system was comprised of 0.3 mm thick piezoresistive based force monitoring elements measuring 1.024 cm^2 in size and having an accuracy of 10%, repeatability of 2%, hysteresis of 5%, and non-linearity in the sensor response of 1.5%. The peak load response of each element was 700 kPa [6]. Another reported system consisted of an instrumented lower limb prosthetic with thirteen custom load applicators strategically positioned at the residuum socket interface. The presented system had a full-scale output of 350 kPa and a linearity of 0.5% [7].

The presented technology already surpasses these sensors with a full scale output of 1460 kPa per loading element; however, the resolution of each array element is currently only 122 kPa. As discussed previously in Chapter 4, the resolution could be modified by lowering the dynamic range, which can be achieved by altering the size of the applicator head as well as the load sharing to increase overall sensitivity while attempting to avoid large decreases in full scale output. Additionally, while the sensor has illustrated an accuracy of less than 10% and nearly 5% hysteresis, making it comparable to commercially available systems, this testing has not been performed according to industry standards. As a result, further testing of these properties, in addition to analysis of sensor to sensor repeatability and non-linearity of the system, could be performed.

7.9 Development of Portable Monitoring System

As mentioned in Chapter 1, the amount and duration of loading are significant in maintaining the health of patient tissue. As a result, part of future works could include the development of a portable monitoring system which would allow for collection of loading information not only briefly during a clinical trial, but long term throughout a patient's day.

7.10 Incorporation of Additional Monitoring Systems

As briefly mentioned in Chapter 1, parameters such as temperature and moisture alter the effect of applied loading on patient tissue. As a result, in order to create a more robust sensing platform, the incorporation of sensing strips capable of monitoring temperature and moisture could be investigated. Both forms of monitoring have already been illustrated for use with magnetoelastic resonant based sensors; however, in this case the use of magnetoharmonic sensing may allow for closer contact with the patient's residuum. Such information could allow for a more thorough understanding of the effect of external stimuli on the applied loading measured at the stump socket interface.

References

1. Keat Ghee, O., Ee Lim, T., Grimes, C.A., and Shao, R., *Resmoval of Temperature and Earth's Field Effects of a Magnetoelastic pH Sensor.* Sensors Journal, IEEE, 2008. **8**(4): p. 341-346.
2. Bergmair, B., Huber, T., Bruckner, F., Vogler, C., and Suess, D., *Removal of earth's magnetic field effect on magnetoelastic resonance sensors by an antisymmetric bias field.* Sens Actuators A Phys, 2012. **183**(44-2): p. 11-15.
3. Suiqiong, L. and Cheng, Z.Y., *Nonuniform mass detection using magnetostrictive biosensors operating under multiple harmonic resonance modes.* Journal of Applied Physics, 2010. **107**(11): p. 114514-114514-6.
4. Ramasamy, M. and Prorok, B.C., *Resonance Behavior of Magnetostrictive Sensor in Biological Agent Detection*, in *Experimental and Applied Mechanics, Volume 6*, T. Proulx, Editor. 2011, Springer New York. p. 875-876.
5. Polliack, A., Sieh, R., Craig, D., Landsberger, S., McNeil, D., and Ayyappa, E., *Scientific validation of two commercial pressure sensor systems for prosthetic socket fit.* Prosthetics and orthotics international, 2000. **24**(1): p. 63-73.6.
6. Portnoy, S., Yizhar, Z., Shabshin, N., Itzchak, Y., Kristal, A., Dotan-Marom, Y., Siev-Ner, I., and Gefen, A., *Internal mechanical conditions in the soft tissues of a residual limb of a trans-tibial amputee*. Journal of biomechanics, 2008. **41**(9): p. 1897-1909.

7. Sanders, J., Zachariah, S., Jacobsen, A., and Fergason, J., *Changes in interface pressures and shear stresses over time on trans-tibial amputee subjects ambulating with prosthetic limbs: comparison of diurnal and six-month differences.* Journal of biomechanics, 2005. **38**(8): p. 1566-1573.

Chapter 8 Conclusion

In response to the need for effective long-term load monitoring systems capable of being embedded and observed wirelessly (Chapter 1), two magnetic based sensing platforms were developed and reported. The first of the presented technologies functioned based on observed increases in the resonant frequency of a vibrating magnetoelastic material in response to applied loading. Unlike the majority of previously developed magnetoelastic resonance based sensors, the developed sensor platform not only experiences an increase in resonant frequency, but also operates using non-uniform loading. This is accomplished as a result of an effective decrease in sensor length which occurs with increasing loads (Chapter 2).

In terms of the actual sensor platform, the first development step focused on fabricating a wireless passive load cell (Chapter 3). Results from the developed load cell lead to the pursuit of a sensor design that would allow for monitoring of applied loading at ranges relevant for prosthetic applications (Chapter 4). To accomplish this, loads were applied at the node of a resonating strip with the expectation that this would allow for monitoring within the desired range. In addition to characterizing the effects of altering load applicator design and size, prototype testing was performed on a four element array instrumented onto a 3D printed portion of a lower limb prosthetic sleeve. The sensor performed with a maximum 10% error when comparing the actual applied total loading to the recalculated loads.

The second sensor platform monitors applied loading by observing a change in the amplitude of the higher-order harmonics of a Metglas 2826MB strip. This was first utilized to develop a multi-element array for monitoring applied loading to a hard surface (Chapter 5). This sensor consisted of three strips each monitored from a separate detection element. A variety of loading combinations were applied to the strips in order to evaluate the effect of neighboring strips on the response captured at each detection element in addition to allowing for an evaluation of the ability to distinguish between various loading combinations. The resulting algorithm was capable of identifying applied loads while taking into account the effect of neighboring strips on sensor response.

The developed sensor platform was then improved such that a single strip could be used as a multi-point sensing array (Chapter 6). Specifically, by monitoring the sensor response from either end of a sensing strip, the effect of loads applied on the front and back portions of each strip were capable of being evaluated. Initial proof of concept testing was performed by instrumenting two strips onto a portion of a lower limb prosthetic donated by Northern Orthotics Inc.

Overall, both systems were capable of wirelessly and passively monitoring loads within physiologically relevant ranges. Additionally, the presented magnetoelastic resonance sensor platform represents an entirely new magnetoelastic based sensing configuration and for this reason, future works (Chapter 7) focus primarily on this technology. Specifically, future works aim to improve the physical design of the resonance sensor in addition to performing more in-depth investigations to expand and validate the theory presented Chapter 2. In summary, the presented work has demonstrated the potential for these systems to be useful in clinical settings for long term patient monitoring.

Appendices

Copyright Information

This information pertains to the thesis entitled:

"DESIGN AND APPLICATION OF WIRELESS PASSIVE MAGNETOELASTIC RESONANCE AND MAGNETOHARMONIC FORCE SENSORS"

By Brandon D. Pereles

Chapters 1 and 2

These chapters consist mostly of original work; however, portions of previously published materials, reprinted in their entirety from Chapter 3, 5 and 6, are also included in these chapters. The reprint permissions for these documents are provided on the following page.

Chapters 3, 5 and 6

These chapters are reprinted in their entirety with permissions provided on the following page.

Chapter 4

This chapter is original work currently in submission.

Chapters 7 and 8

These chapters contain original work and unpublished work.